Fall 10-16-2018

# A Narrow-wall Complementary-split-ring Slotted Waveguide Antenna for High-power-microwave Applications

Xuyuan Pan
*University of New Mexico*

Xuyuan Pan

*Candidate*

Electrical and Computer Engineering

*Department*

This dissertation is approved, and it is acceptable in quality and form for publication:

*Approved by the Dissertation Committee:*

Christos Christodoulou, Chairperson

Edl Schamiloglu

Mark Gilmore

Joseph Costantine

Julie Lawrance

# A Narrow-wall Complementary-split-ring Slotted-waveguide-antenna for High-power-microwave Applications

by

**Xuyuan Pan**

B.S., Electrical Engineering, Xidian University, 2011

M.S., Electrical Engineering, University of New Mexico, 2012

DISSERTATION

Submitted in Partial Fulfillment of the

Requirements for the Degree of

Doctor of Philosophy

Engineering

The University of New Mexico

Albuquerque, New Mexico

December, 2018

# Dedication

*To my loving parents, Zhaichun Pan and Naiqin Tong for all the unconditional support, encouragement and belief in me.*

# Acknowledgments

I would like to thank my advisor, Dr. Christos Christodoulou for accepting me as his Ph.D student and giving the opportunity to work on this research project. I am honored and humbled for having been able to work under his supervision. I thank him for encouraging me to work on the project and offering me the facility and equipments to perform experiments. I am also very thankful to Dr. Christodoulou for financially supporting me through my Ph.D program.

I thank Dr. Edl Schamiloglu, Dr. Mark Gilmore and Dr. Joseph Costantine for being on my committe. I am thankful to have a committe full of decorated professors.

I thank my colleague and friend, Dr. Firas Ayoub, Dr. Hamide Faraji, Mr Arjun Gupta, Dr Brian Mackie-Mason, and Mr. George Atmatzakis for all the discussionns we had, all the experiments we performed and all the difficulties we encountered and overcame.

I thank Dr Emil Ardelean for his help with the fabrication of the antenna design model. I thank Dr. Julie Lawrence and her team, Mr. Jeremy Mcconaha and Mr. Matthew Landavazo for their help with the high power microwave tests performed at the Air Force Research Lab.

This work is supported by ONR grant N00014-13-1-0415.

2

[2]To my family and friends, who are the nicest people I ever know

# A Narrow-wall Complementary-split-ring Slotted-waveguide-antenna for High-power-microwave Applications

by

**Xuyuan Pan**

B.S., Electrical Engineering, Xidian University, 2011
M.S., Electrical Engineering, University of New Mexico, 2012

Ph.D., Engineering, University of New Mexico, 2018

## Abstract

A narrow-band, rugged, complementary-split-ring (CSR) slotted waveguide antenna (SWA) with significant size reduction is presented. The antenna is to be vertically front mounted on a land vehicle, with a horizontally polarized fan-beam radiation pattern. The radiation characteristics of a CSR slot in the narrow-wall of a rectangular waveguide are studied for the first time in this work. Both simulation and experimental results show that the complementary-split-ring slot radiates a linearly polarized wave with a total efficiency and gain close to those of conventional longitudinal slots, while the proposed CSR slots have a maximal outer diameter of $0.23\lambda_0$, much smaller compared to conventional half-wavelength longitudinal slots. The CSR slotted waveguide antenna provides, approximately, 55% size reduction, with high directivity, low return loss, and very high power handling capability for

S-band applications. A set of periodic air-filled corrugations is added to the other narrow-wall of the rectangular waveguide to improve the overall gain of the antenna. Experimental data is presented to further validate simulation results.

A new procedure for estimating power handling capability for high-power-microwave antennas, especially slotted waveguide antenna designs, is proposed. The new method takes into account both air-breakdown and multipcation breakdown account. It is suitable for predicting the input power threshold for high-power-microwave antennas operating both under vacuum condition and under air environment. The estimated input power threshold for the S-band narrow-wall longitudinal slotted waveguide antenna acts like a proper guideline for the high-power-microwave experiment performed on the HPM antenna.

3D priting technology is used for developing fast-prototyping methods for microwave passive devices with complicated structures (meta-materials) for high-power-microwave applications. The electro-plated SLA printed CSR-SWA is tested under high-power-microwave pulse and no significant degrading in radiation performances is detected. The electro-plated SLA printed CSR-SWA also provides advantages like cheap, light-weighted.

# Contents

# List of Figures

# List of Tables

# Chapter 1

# Introduction

## 1.1 Overview

The last 50 years have seen an unprecedented and unparalleled growth in the development and use of electronics, both in military and civilian applications. Associated with this has been an increase in concerns over electromagnetic (EM) compatibility[1][2]. The vulnerability of electronics to the generated waveforms has also been proven[3][4]. The developments of HPM source technology have seen major increase in efficiency and reduction in size over the past years[5]. High power microwave antennas are key devices to develop HPM systems[6][7]. HPM antennas are designed to have high-gain, low return loss, withstand high input power and be very compact.

### 1.1.1 overview of development of high-power-microwave antennas

Depending on the feeding HPM source (magnetrons, backward-wave oscillators (BWO), magnetically insulated line oscillators (MILO), Marx generators, etc.)[5], designs of HPM antennas have been proposed in the form of folded horn antenna [8], slotted waveguide antenna[9][10], lens antenna[11], radial transmission helix array[12][13], reflectarray antenna[14] etc. HPM antennas can provide very intense electric field (E-field) levels at hundreds of meters covering narrow band to ultra-wide band spectrums. Such antennas must have a gain as high as possible, side lobes as low as possible, withstand input power as high as possible, and be very compact.

The HPM antennas proposed here are required to be rugged and low-profile to be easily mounted on a variety of platforms. The HPM antenna is required to provide a fan-beam radiation pattern with the electric field polarized along the broad beam-width of the pattern. The antennas under considerations are air-filled narrow-wall slotted waveguide antennas for its ruggedness and high-power handling capability. This type of antenna provides high directivity, low return loss as well as mechanic structural strength. The need to miniaturize the antenna size to fit the platform also leads us to the design of slotted waveguide antennas.

The idea of longitudinal slots in the narrow wall of a rectangular waveguide for high-power has been proposed by Baum [15]. Apertures in the narrow wall of a rectangular waveguide can handle high powers, because the theoretical value of the electric field for the TE10 mode at the narrow wall is zero. This behavior has been used by Taylor and Giri to design a narrow-wall directional coupler for

high power[16]. Traditional slotted waveguide antenna design uses an equivalent transmission line model[17][18]. However, this analytic approach assumes that the apertures are narrow, which decreases power handling capability of the slot array. An array of longitudinal slots in the narrow wall of a rectangular waveguide has been proposed by Pan[19], using slots whose widths are comparable to the lengths. The S-band narrow-wall slotted waveguide antenna consists of four longitudinal slots on the narrow-wall of the waveguide and an H-plane-bend (HPB) radiator as the end structure. The array is designed to radiate as a uniform array[20]. Such slot array produces a fan-beam radiation pattern.

The design combines a microwave network analysis and a full-wave analysis, instead of conventional transmission line model[21][22]. This approach is proven to be suitable for design of slotted waveguide antenna of unconventional apertures.

### 1.1.2 overview of miniaturization of slotted antennas

The key challenging aspect of any compact HPM antenna design is to maintain high-power handling ability while miniaturizing the size of the antenna. More recently, single split-ring resonators have been placed underneath longitudinal slots inside the feeding[23]. The split-ring resonators increase the field intensity under the slots and consequently recover the gain and efficiency of a slot smaller than a conventional half-wavelength slot[24]. However the reduction in size is limited to $0.25\lambda_0$. The complexity of manufacturing increases significantly due to the fact that the split-ring resonator must be precisely located underneath the slot and must be designed to match the desired resonant frequency. To further reduce the size of the slot and to overcome the manufacturing complexities, an alternative technique is

required.

## 1.2 Introduction to complimentary-split-ring slotted waveguide antenna

A split-ring slot cut in the broad-wall of a rectangular waveguide is proposed and investigated by Daliri [25]. Such split ring slot cut is reported to reduce outer diameter to less than $0.25\lambda_0$, while providing similar radiation characteristics as the conventional half-wavelength slot. A 4-element array of complimentary split ring resonators (CSRRs) cut on the broad-wall of a rectangular waveguide was proposed by Daliri [26]. The CSSR array has similar reflection characteristics and radiation pattern to conventional rectangular slot SWA array. The peak realized gain of this array is close to an array of conventional elements and far superior to an array of rectangular slots with similar size.

The idea of combining the advantage of the compact size of split ring slots and the higher power handling capability of narrow-wall apertures leads to the design of the narrow-wall rugged complementary-split-ring (CSR) slotted waveguide antenna (SWA) [27]. The radiation characteristics of complementary-split-ring slots in the narrow-wall of a rectangular waveguide have not been reported in the literature previously. The design of an array of complementary-split-ring slots in the narrow wall of a rectangular waveguide is based on the presented parametric study on the geometrical parameters of the complementary-split-ring slots. A microwave network analysis is then employed, and is verified by full-wave analysis using AYSNS Corporations High Frequency Structure Simulator (HFSS).

The proposed CSR-SWA shows similar radiation characteristics compared to conventional rectangular slot arrays. It provides higher peak gain than the convetional $\lambda/4$ rectangular slot array and a more compact size (55% size reduction) compared to the $\lambda/2$ rectangular slot array.

However, due to the much closer center-to-center spacing, strong coupling is expected among the complementary spit ring slots. Thus, much thicker walls are used, compared to a standard WR284 waveguide for S band applications. To further enhance the coupling between the wave propagating along the waveguide and the much deeper CSR slots, a set of periodic air-filled corrugations is added to the other narrow-wall of the rectangular waveguide. The periodic air-filled corrugations loaded CSR-SWA shows similar reflection characteristics and radiation pattern to the non-corrugations loaded CSR-SWA, with a slightly higher peak gain.

To suppress grating lobes, the double narrow-wall CSR-SWA array is proposed. It consists of two identical narrow-wall complementary-split-ring slotted waveguide antennas, sharing a common broad-wall. The apertures are alternating from one side of the common wall to the other. The length of the double narrow-wall longitudinal slot array is approximately the same as the single array. However, the aperture field distribution of the double narrow-wall longitudinal slot array is more uniform than that of the single array. The double narrow-wall CSR-SWA array provides similar peak gain compared to the conventional $\lambda/2$ rectangular slot array, while its able to reduce the antenna size to 55% along the direction of wave propagation, making it much easier to be mounted on vehicles.

## 1.3 Power handling capability estimation of the high-power-microwave antenna

The power handling capability of a high-power-microwave antenna is generally investigated in the stage of experiment verification, which is time consuming and costly. Some high power microwave antenna designs include maximum allowable input power estimation, through comparing the maximum field intensity within the antenna structure to the breakdown down field intensity threshold [28][29][27]. While this approach is sufficient to determine the input power threshold, it is normally not clearly stated in the estimation of the circumstances that the HPM antennas are operating under. For instance, in [30] the metal breakdown field intensity threshold for vacuum is used while not specifically stating that the antenna is used in vacuum. In [28], the air breakdown field intensity threshold is used while not considering such threshold is critically related to the air pressure level at the testing facility. Also, in the case of [30], the vacuumed HPM antenna can suffer from another breakdown mechanism, i.e. multipaction [31], depending on the pulse duration of the input high power microwave pulses. Thus, the maximum allowable input power estimation methods applied so far are not accurate enough to serve as the guideline for experiment verification.

Power handling capability estimation of the HPM antennas were conducted based on two breakdown mechanisms: air breakdown [32] [33] and multipaction breakdown [31]. The longitudinal slotted waveguide antenna proposed in [19] was under investigation. Both input power threshold for the S-band longitudinal slotted waveguide antenna based on the two mechanisms were obtained. Such results were

able to serve as the guideline for the experiment verification. The entire large signal experiment was conducted under 'safe' conditions. The obtained experiment results showed that the longitudinal slotted waveguide antenna was suitable for high power microwave applications.

## 1.4 3D printing technology for fast prototyping high-power-microwave antennas

The proposed CSR-SWA designs depend on highly accurate electromagnetic simulations that take geometric details into full account. Conventional antenna manufacturing approaches such as direct machining and platelet technology require complex assemblies and lack the ability to precisely translate the electromagnetic simulation model into its physical metallization. To rapidly prototype complex 3D antenna structures in a cost-effective way for high-power-microwave applications, we propose an approach applying stereolithography or 3D printing technology. Recently, it was shown that a horn antenna can be printed using electron beam melting (EBM), using a specialized 3D printer by Garcia [34]. However, the majority of 3D printers print on acrylonitrile butadiene styrene (ABS) plastic. The idea of fabricating complex antennas using plastic and then coating with a conductive material benefits from the high manufacturing precision of 3D printing and its lightweight [35][36]. Also, in [37], 3D printing technology has already been used to prototype components for high-power-microwave magentron designs.

A single CSR-SWA was printed by uPRINT SE 3D printer using ABSplus. It was then spray painted by metallic coatings. It shows similar measured return loss and

radiation patterns compared to the metallic CSR-SWA. However, the metallic coating used is lossy compared to the conductive spray typically used for electromagnetic interference (EMI) reduction, though much cheaper and more cost-effective.

To improve EM performance of the 3D printed CSR-SWA, plating the 3D printed antenna with materials of much higher conductivity is investigated. Laser cutting of 3D printed waveguide has been used for the manufacture of a simple slot array (one waveguide), but the work presented here is the first example of 3D printing entire slot arrays including all CSR slots, and H-plane-bend radiator, in such a way that the entire array can be plated without disassembly. Two samples of the CSR-SWA were printed by uPRINT SE and ProX 800, respectively. The CSR-SWAs were then plated with copper by RePliForm Inc. in Baltimore, MD.

The copper-plated 3D printed CSR-SWAs show similar measured return loss and radiation patterns, with a slightly lower peak gain. The high power microwave measurements indicates that such copper-plated 3D printed CSR-SWAs can handle high-power-microwave pulses.

## 1.5 Division of this dissertation

The work is organized as follows: **the first chapter** gives the brief introduction to this work. **The second chapter** illustrates the analysis of single complementary split ring slot on rectangular waveguide walls. **The third chapter** describes the design of narrow-wall complementary-split-ring slotted waveguide antennas. It includes the microwave network analysis and the full-wave computational analysis of the antenna design. Chapter three also includes the description of the design

of periodic air-filled corrugations loaded CSR-SWAs and the design of the double narrow-wall CSR-SWA array. **The fourth chapter** discusses the maximum allowable input power for the slotted waveguide antenna design without causing breakdown. Two breakdown mechanism are both investigated to determine the maximum input power threshold for the high-power-microwave antenna. **The fifth chapter** describes the validation of the theoretical results through experiments, including the introduction of fast-prototyping the CSR-SWA using 3D printing technology. **The sixth chapter** concludes the work that is included in this dissertation and describes the future work of improving the beam steering mechanism of the narrow-wall longitudinal-slot array antennas.

# Chapter 2

# Complementary-split-ring slots on rectangular waveguide walls

Metamaterials can offer opportunities to realize new physical phenomena that are difficult to achieve with ordinary materials [38][39]. Potential powerful applications of metamaterials have ranged from sub-wavelength focusing and imaging [40][41], negative refraction or double negative (DNG) characteristics [42][43][44], highly directional radiation [45][46], and artificial magnetism [47] to electromagnetic cloaking [48][49]. In most of these applications, a resonance is usually involved, mainly to achieve a negative or other desired magnetic permeability. A typical resonator is the split-ring resonator (SRR), which provides a negative magnetic permeability near resonance for some particular polarization of the incident wave [43][50]. The SRR structures, together with many variants, have served in most cases as metamaterials [51][52][53]. A considerable amount of effort, both theoretical and experimental, has been put toward the study of SRRs [43][44][54][55][56][57].

## 2.1 Slotted Circular cylinders

Slotted circular cylinder resonators (SCCRs) are two dimensional analogs of split ring resonators (SRRs), and, for an incident electromagnetic wave with the magnetic field parallel to the cylinder axis, they can provide negative values of magnetic permeability near the magnetic resonance frequency as well. As a result, SCCR structures may serve as an alternative type of metamaterials [58].

It is known that the artificial magnetism in magnetic resonator structures like SRRs and SCCRs is a local effect due to the internal resonance, instead of arising from the interference between fields radiated by scatterers [59]. As a result, we can focus on the magnetic resonance frequency $\omega_m$ of an individual SCCR, instead of that of the periodic SCCR structures.

The resonance behavior of a SCCR is characterized by the radar cross sections (RCSs) with an incident plane wave, whereas the artificial magnetism is identified by its frequency dependence of the magnetic permeability. It is shown that, near the resonance of a SCCR, the frequency dependence of the magnetic polarizability is similar to that in the SRR, corresponding to a magnetic resonance. As a result, the magnetic resonance manifests itself by a peak of the RCS as a function of the incident frequency. So, we can concentrate on the calculation of the RCSs as a function of the incident frequency.

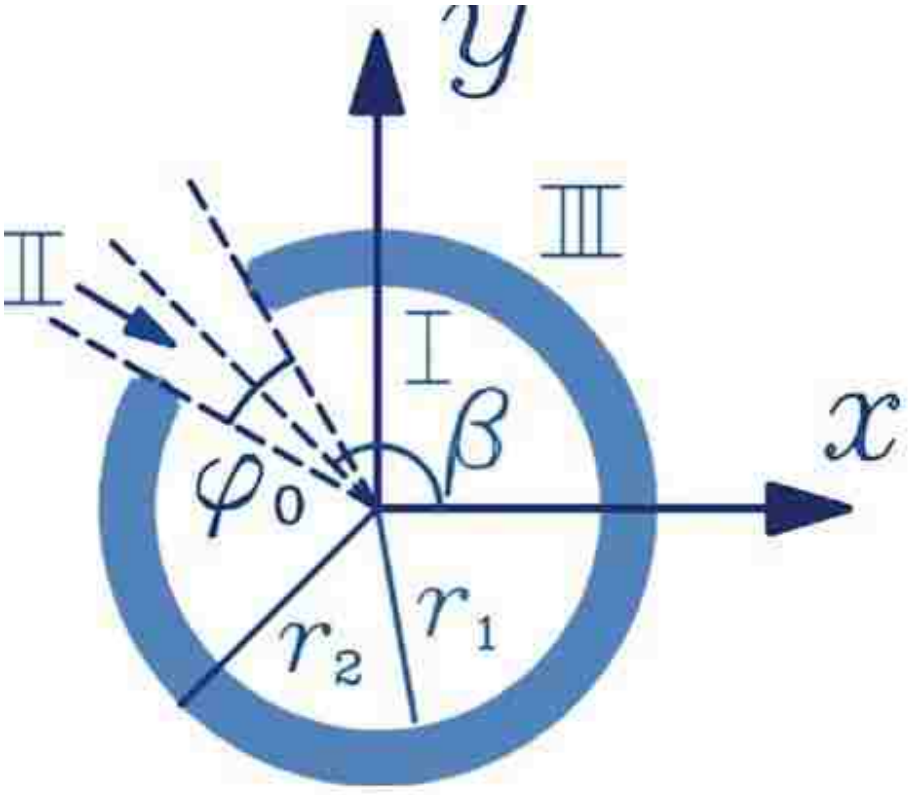


Figure 2.1: Geometry of SCCR structure with nonzero thickness

### 2.1.1 RCS of slotted circular cylinders

The plane-wave scattering by a SCCR has been studied by many authors through various analytical approaches. These efficient analytical approaches provide us the possibility to study the SCCRs resonance behaviors with a rigorous full-wave approach beyond the quasi-static approximation. Ziolkowski and co-workers have studied the scattering from an axially slotted infinitely thin cylinder shell using the generalized dual-series-based Riemann-Hilbert approach [60][61], which is an accurate method ensuring any desired accuracy of the obtained results. The dual-series-based Riemanna Hilbert approach was extended to solve a slotted cylinder

with outer or inner material coating for both transverse electric (TE) polarized and transverse magnetic (TM) polarized waves [62][63]. Serebryannikov and Nosich [64][65] studied the scattering of a plane wave by a circular cylinder shell with a finite thickness and several apertures by an integral representation of the tangential electric field on the slot apertures and the Galerkin method, using weighted Gegenbauer polynomials as basis functions.

The geometry of the SCCR structure is shown in Figure 2.1. The inner radius of the slotted cylinder shell is $r_1$, and the outer radius is $r_2$. The extend of the perfect metal of the slotted cylinder is taken between $\varphi_0 < |\varphi - \beta| \leq \pi$. The angular width of the slot is $\varphi_0$ and the angle between the center of the slit and x axis is $\beta$.

The SCCR structure is illuminated by the TE-polarized plane wave with the magnetic field along the axis of the cylinder. The magnetic field $H_z$ in region I ($r < r_1$), with permittivity $\epsilon_1$ and permeability $\mu_1$, is expanded as follows:

$$H_z^I = \sum_{m=-\infty}^{\infty} b_m J_m(k_1 r) e^{-im\varphi} \tag{2.1}$$

Where $J_m(x)$ is the Bessel function of order $m$, $k_1 = k\sqrt{\epsilon_1 \mu_1}$ with $k = \omega/c$ the incident wave number.

In Region II, we have:

$$H_z^{II} = \sum_{m=0}^{\infty} [D_m J_{\nu_m}(k_2 r) + E_m Y_{\nu_m}(k_2 r)] cos[]\nu_m(\varphi - \widetilde{\varphi}_0)] \tag{2.2}$$

Where $Y_h(x)$is the $h$th-order Neumann function, $\widetilde{\varphi}_0 = \beta - \varphi_0/2$, $\nu_m = m\pi/\varphi_0$, and $k_2 = k\sqrt{\epsilon_2 \mu_2}$ with permittivity $\epsilon_2$ and permeability $\mu_2$ in the slot. Equation

2.2 guarantees that $E_r$ vanishes at the wall of the slot. Finally, in the outer space, region III, with permittivity $\epsilon_0$ and permeability $\mu_0$, $H_z$ is the sum of the incident and scattered fields,

$$H_z^{III} = H_z^{inc} + H_z^{sc} \tag{2.3}$$

$$H_z^{inc} = \sum_{m=-\infty}^{\infty} p_m J_m(kr) e^{-im\varphi} \tag{2.4}$$

$$H_z^{sc} = \sum_{m=-\infty}^{\infty} a_m H_m^{(1)}(kr) e^{-im\varphi} \tag{2.5}$$

Where $H_h^{(1)}(x)$ is the $h$th-order Hankel function of the first kind, $p_m$ and $a_m$ are the expansion coefficients for the incident field and the scattered field, respectively.

Following the method of Serebryannikov and Nosich, from the continuity of $H_z$ and $E_\varphi$ in the aperture and the vanishing of $E_\varphi$ inside the metal, the electrical field is cast in the following form:

$$E_\varphi^I(r_1, \varphi) = E_\varphi^{II}(r_1, \varphi) = \sum_{i=1}^{M} c_i \Theta_i(\varphi) \tag{2.6}$$

$$E_\varphi^{III}(r_2, \varphi) = E_\varphi^{II}(r_2, \varphi) = \sum_{i=1}^{M} d_i \Theta_i(\varphi) \tag{2.7}$$

Where $\Theta_i(\varphi)$ is the weighted Gegenbauer polynominal of the order $-1$, which appropriately considers the edge effect.

The relation between the scattering coefficients $a_m$ and the incident coefficients $p_m$ in terms of scattering matrix $S$ is:

$$a_m = \sum_{m'} S_{mm'} P_{m'} \tag{2.8}$$

With the scattering matrix $S$, we can compute the scattering field at any position. The resonance of SCCR is identified by the peak of the normalized RCS as a function of frequency, with the normalized RCS given:

$$\sigma = \frac{1}{\pi r^2} \lim_{r\to\infty} \frac{2\pi r |H_z^{sc}(r, \varphi_{inc})|^2}{|H_z^{inc}|^2} \tag{2.9}$$

where $\varphi_{inc}$ the incident angle of the plane wave.

Figure 2.2 displays the normalized RCS of an SCCR with a slit width $\varphi_0 = 10°$, normalized outer and inner radius $r_2 = 1$ amd $r_1 = 0.95$. A resonance is identified from the peak of the RCS. Near the resonance the frequency dependence of the magnetic polarizability is similar to that in the SRR, corresponding to a magnetic resonance. As a result, the magnetic resonance manifests itself by a peak of the RCS as a function of the incident frequency.

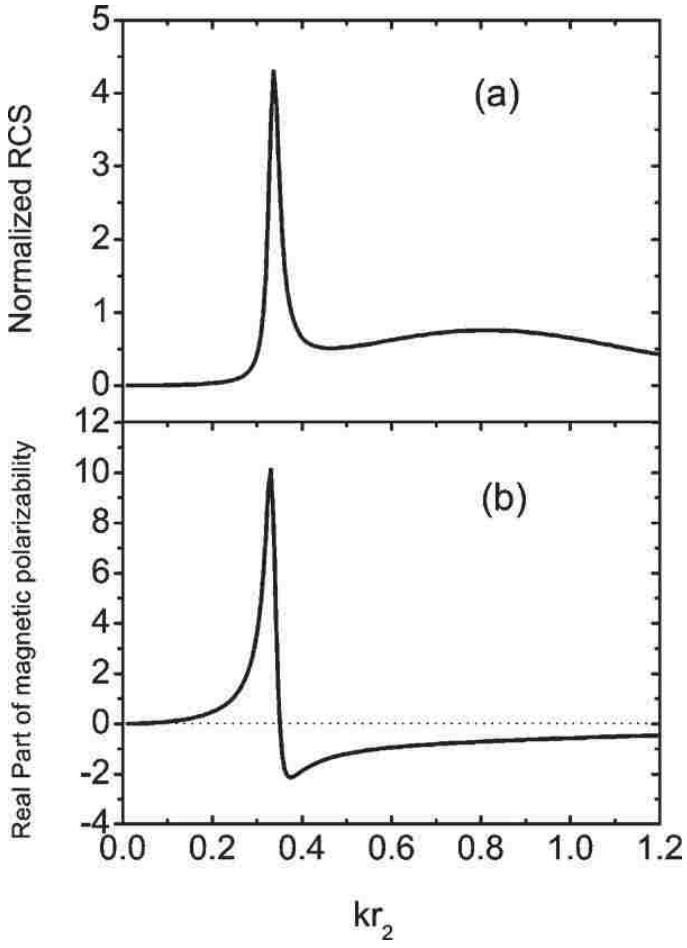


Figure 2.2: (a)Frequency dependence of the normalized RCS and (b) the behavior of the real part of the magnetic polarizability for a single SCCR. [58]

### 2.1.2 Magnetic resonance of slotted circular cylinders

We first identify the magnetic resonance of SCCRs since the interesting characteristics of the SCCRs occur near its magnetic resonance frequency. To identify the magnetic resonance, we calculate the magnetic polarizability of a single SCCR susing

the expression:

$$\mathbf{m} = \chi \mathbf{H} \tag{2.10}$$

$$\boldsymbol{m} = (\boldsymbol{m_i} + \boldsymbol{m_o})/\boldsymbol{\pi r_2^2} \tag{2.11}$$

$$\boldsymbol{m_i} = \frac{1}{2}\int \boldsymbol{r} \times \boldsymbol{j_i} dS \qquad , \qquad \boldsymbol{m_o} = \frac{1}{2}\int \boldsymbol{r} \times \boldsymbol{j_o} dS \tag{2.12}$$

where $\boldsymbol{m}$ is the magnetization density, $\boldsymbol{H}$ is the magnetic field intensity, and $\chi$ is the magnetic polarizability of a SCCR, $\boldsymbol{j_i}$ ($\boldsymbol{j_o}$) is the surface current density on the inner (outer) surface.

Physically, the SRR has been modeled as an L-C circuit system to exhibit its magnetic properties [66][67][68]. Similar to SRR structures, the SCCR structure can be modeled as an L-C circuit system, whose capacitance arises from both the cavity of the cylindrical shell and the slot, whereas the inductance comes from the conducting shell. An approximate expression for the capacitance of the SCCR for small slit width and shell thickness is given by

$$C = \epsilon_2 \frac{r_2 - r_1}{r_1 \phi_0} + 0.275\pi\epsilon^{3/4}(r_2 - r_1)^{2/5}(2\pi - \phi_0) \tag{2.13}$$

the inductance of the SCCR is approximated by that of a circular loop [69], with a small empirical correction taking into account the 2D characteristics and the effect of slit on the cylinder,

$$L = R[ln(\frac{8R}{r_2 - r_1}) - 2 + \frac{1}{4}] \tag{2.14}$$

Thus, the magnetic resonance frequency is evaluated by

$$\omega_m = \frac{1}{\sqrt{LC}} \tag{2.15}$$

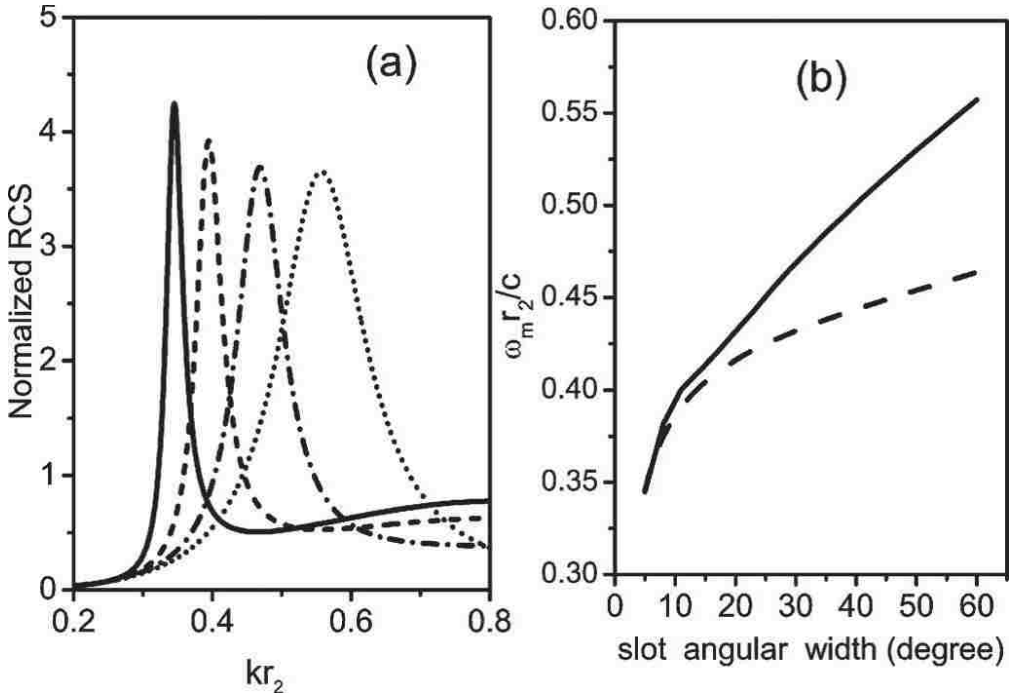


Figure 2.3: (a) Frequency dependence of the normalized RCS of a SCCR on the slot angular width. Solid line: $\varphi = 5°$, dashed line: $\varphi = 10°$, dot-dashed line: $\varphi = 30°$, dotted line: $\varphi = 60°$ (b) Variation of the magnetic resonance frequencies of a SCCR with the slot angular widths in the cavity. Solid line: rigorous approach, dashed line: empirical expression. [58]

The effect of the geometrical parameters of SCCRs on the magnetic resonance have been investigated by [58].Increasing the slit width results in an increase of the magnetic resonance frequency of the SCCR structure. Physically, when the slit width is increased, the capacitance will decrease. In fact, the inductance of the SCCR structure will also decrease when the slit width increases. Decreasing the capacitance and inductance of the system will increase the resonance frequency. However, the change of magnetic resonance with the metal shell thickness is no longer monotonic. Instead, there appears to be an optimal value for the shell thickness that corresponds

to the lowest resonance frequency. Only when the shell thickness is larger than this optimal value does increasing the shell thickness result in an increase of the magnetic resonance frequency of the SCCR structure. The situation is quite different for the case of SRRs.

A complementary split ring slot in a perfectly conducting plate (finite thickness) is the complementary structure of a SCCR. It can also be viewed as the two dimensional analog to the complementary split ring resonator (usually a split ring shaped cut on a conducting sheet). Thus, CSR slots perform both as a resonating structure and as a radiating structure. Similar to most slot antennas. A practical CSR slot antenna uses cavity backed CSR slots, such as CSR slots on either broad-wall or narrow-wall of a rectangular waveguide.

## 2.2 Complementary-split-ring slots on the broad-wall of a rectangular waveguide

Recently, single split-ring resonators have been placed underneath longitudinal slots to reduce slots size. The split-ring resonators increase the field intensity under the slots and consequently recover the gain and efficiency of a slot smaller than the conventional half-wavelength slot [24]. The split-ring resonators must be designed to match the desired resonant frequency, as well as precisely placed underneath the slot, to increase the field intensity under the slots. Thus, the complexity of manufacturing increases significantly. Also, the reduction in size is limited to 0.25 without losing the radiation performance. To further reduce the size of the slot and to overcome the manufacturing complexities, an alternative approach is required.

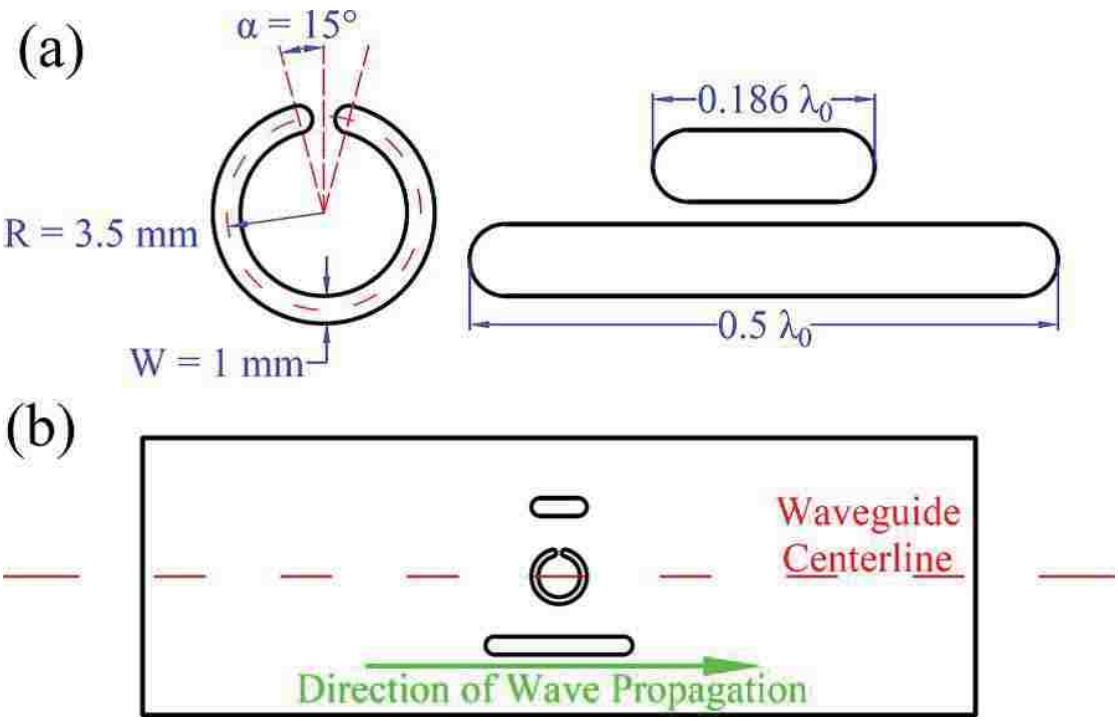


Figure 2.4: (a) Geometry of the split-ring slot in comparison to the rectangular slots. (b) Position of the slots on the broad-wall of a rectangular waveguide. [26]

[26] has proposed a broad-wall slotted waveguide antenna array using complimentary split ring resonator elements. It is shown that the proposed CSR slot, of which the outer diameter is $0.186\lambda$, provides radiation efficiency and gain comparable to those of conventional $0.5\lambda$ rectangular slots. The results indicate that the performance of the CSR-SWA array is far superior to an array of rectangular slots with the same length, and is very close to that of an array of traditional half wavelength rectangular slots.

Figure 2.5, 2.6 and 2.7 show comparison of total efficiency and realized gain of the rectangular slots and split ring slots.

This reduction in slot size while maintaining similar radiation characteristics,

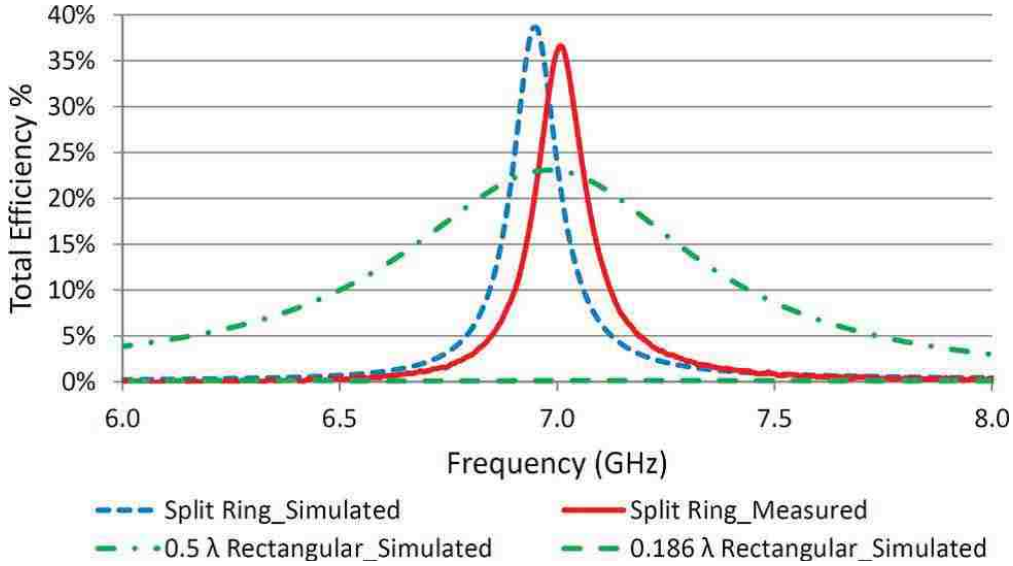


Figure 2.5: Comparison of total efficiency of the rectangular slots and split ring slots. [26]

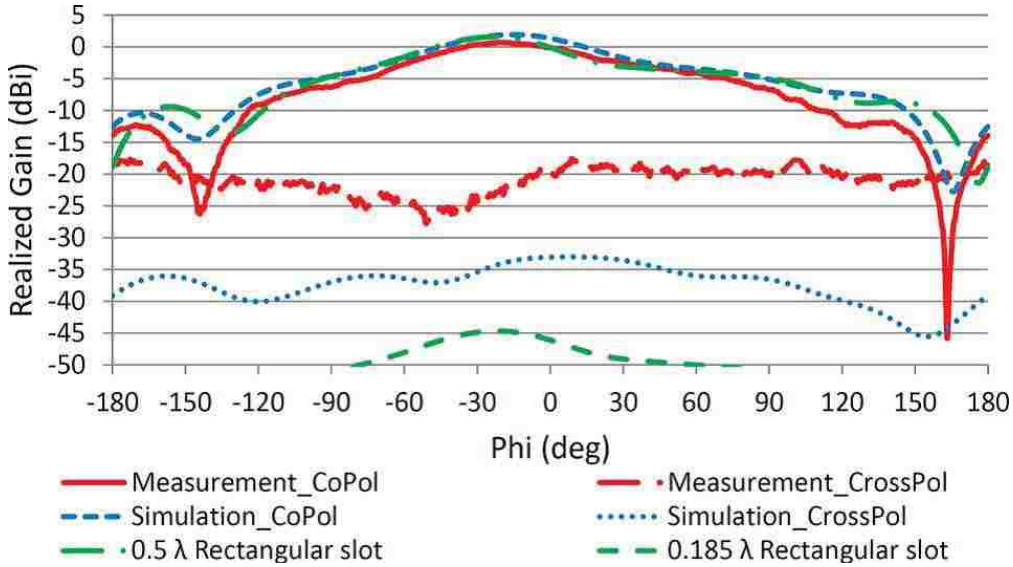


Figure 2.6: Comparison of realized gain of the rectangular slots and split ring slots. [26]

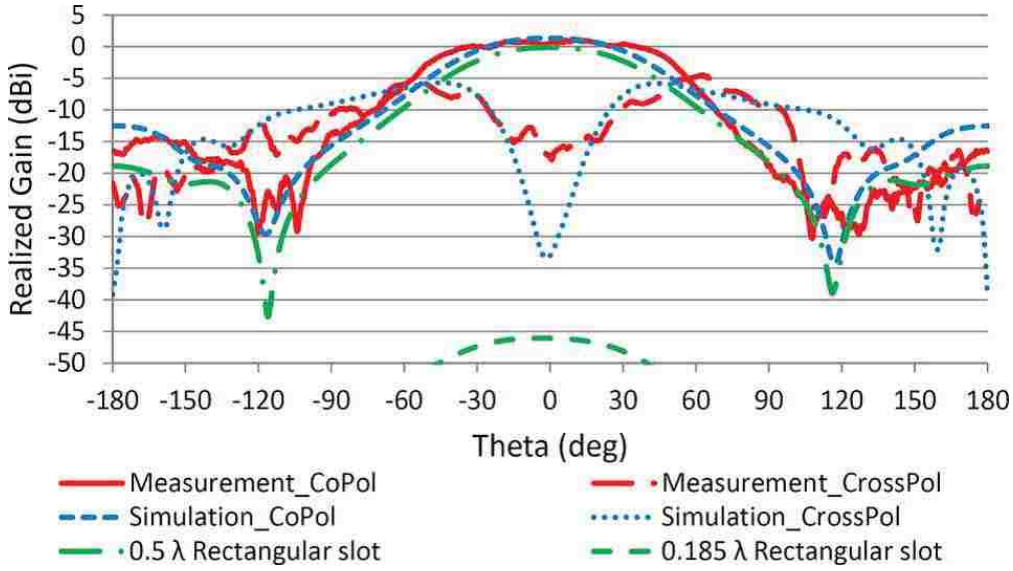


Figure 2.7: Comparison of realized gain of the rectangular slots and split ring slots. [26]

further decreases the overall size of the slot array. In other words, within the same dimension of the conventional half-wavelength slot array, there can be more CSR slots implanted, which means more radiating array elements. As a result, better radiation performance and more array functionality such as beamsteering can be achieved.

## 2.3 Complementary-split-ring slots on the narrow wall of a rectangular waveguide

Apertures on the narrow-wall of a rectangular waveguide are better fit for high-power microwave applications, especially under the dominant $TE_{10}d$ mode. To combine the advantage of high-power handling capability of the narrow-wall slots

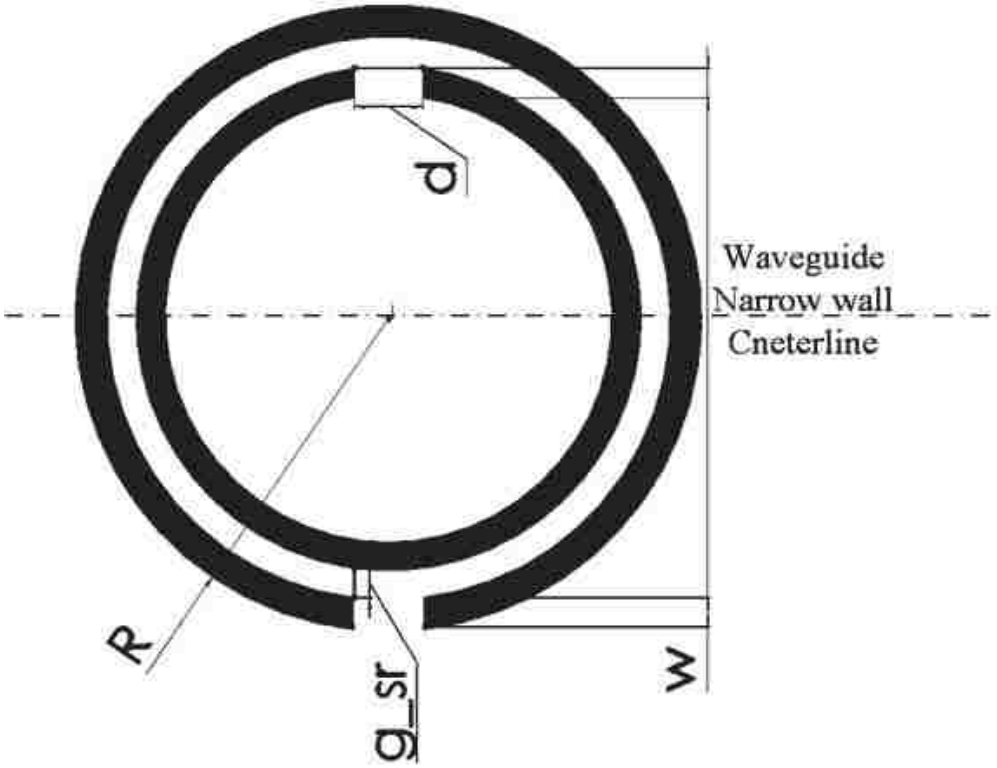


Figure 2.8: Design parameters of the CSR slot

and compact size of complimentary split ring slots, complementary split ring slots on the narrow-wall of a rectangular waveguide are proposed. A parametric study on the CSR slot on the narrow-wall of a rectangular waveguide is performed.

### 2.3.1 Design parameters of CSR Slot on the narrow-wall of a rectangular waveguide

The parameters that define the geometry of the CSR slot are shown in Fig 2.8. The waveguide used in this study is a standard S-band waveguide, WR284. The

outer radius of the outer ring is defined by $R$, the width of both the inner and outer rings is defined by $w$, and the size of the slit on both the inner and outer rings is defined by $d$ or the angular width $\alpha$. The gap between the inner radius of the outer ring and the outer radius of the inner ring is defined by $g_{sr}$. The rotations of the slit on both the inner and outer rings relative to the waveguide centerline are set to be $-90°$ and $+90°$ respectively. These rotation angles are chosen to intercept the surface current on the narrow-wall.

The EM performance of the CSR slots is directly affected by the offset of the slots from the waveguide centerline in the case of CSR slots on the broad-wall of a rectangular waveguide. However, since the CSR slot on the narrow-wall of a rectangular waveguide couples only with the magnetic field under the dominant mode TE10, the impact of the offset of the CSR slot from the waveguide centerline on the EM performance is negligible.

### 2.3.2 Parametric study of the CSR slot

The resonant frequency of the CSR-slot can be independently controlled by parameters $R$, $w$, $\alpha$. HFSS was used to model such slots on the narrow-wall of a rectangular waveguide, as shown in Fig. 2.9. The resonant frequency of the CSR slot mainly depends on its circumference. Thus, as shown in Figure 2.10 for the $S11$, increasing $R$ while keeping $w$, $\alpha$ and $g_{sr}$ constant results in the reduction of the resonant frequency. Similarly, Figure 2.11 shows that increasing the circumference of the split ring by reducing $\alpha$ leads to a reduction of the resonant frequency. The capacitance of the split ring is reduced by increasing w which consequently increases the resonant frequency of the CSRR. However, the inductance of the split ring

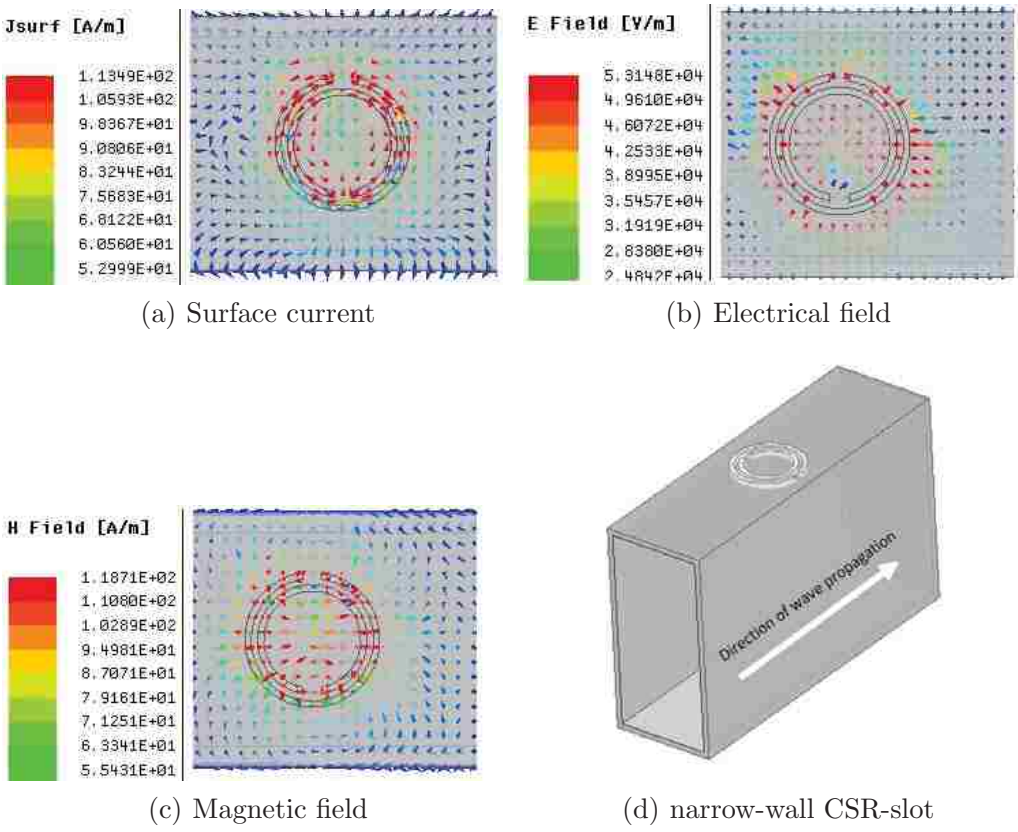


(a) Surface current (b) Electrical field

(c) Magnetic field (d) narrow-wall CSR-slot

Figure 2.9: Narrow-wall CSR-slot in HFSS

increases by increasing w which reduces the resonant frequency.

The effective capacitance of the split ring is a factor of the ratio of the inner and outer radii of the ring and this ratio depends on $w$ as well. However, the effective inductance depends on the square value of the gap width. Therefore for a constant $R$, $\alpha$ and $g_{sr}$, the resonant frequency of the split ring slot can further be reduced by increasing $w$.

In general, the sensitivity of these parameters on the overall properties of a CSR-type antenna increase the difficulty of modeling the CSR-slots compared to the standard longitudinal slots. In the case of longitudinal slots, for a specific width,

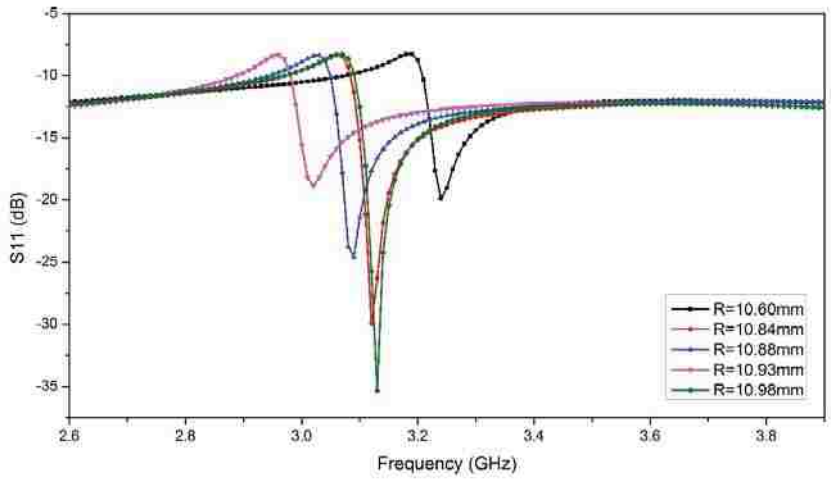


Figure 2.10: Effect of changing the CSR slot radius, R, on the resonant frequency and $|S11|$

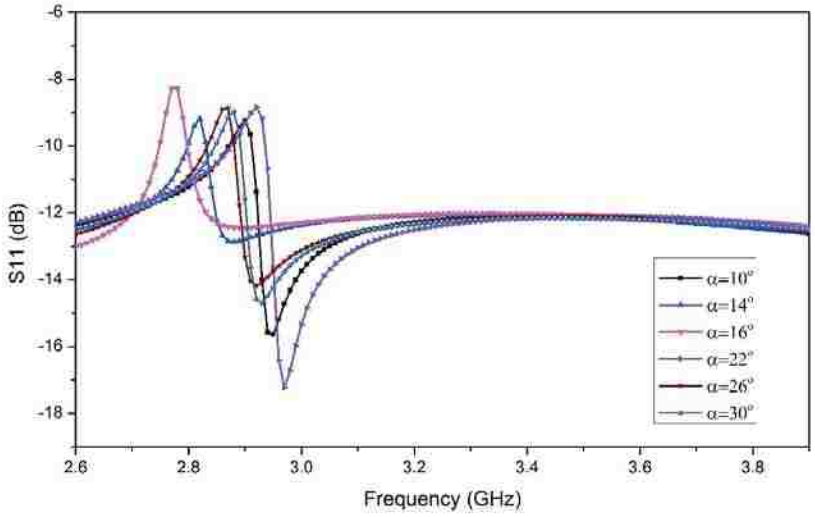


Figure 2.11: Effect of changing the CSR slot width, $\alpha$, on the resonant frequency and $|S11|$

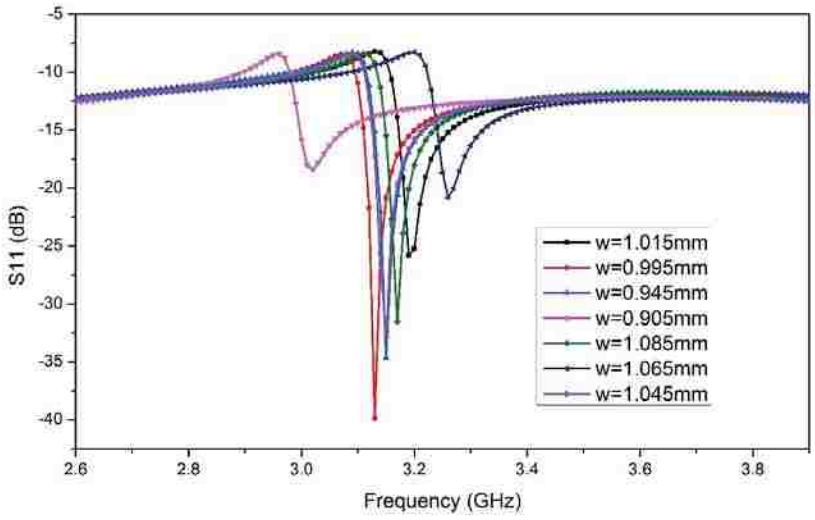


Figure 2.12: Effect of changing the CSR slot gap size, w, on the resonant frequency and $|S11|$

there is a corresponding length that produces resonance or peak power radiated, and sharper resonances are associated with thinner slots, while in the case of CSR-slots, it's the specific set of $R$, $w$, $\alpha$, $g_{sr}$ contributing to resonance or peak power radiated.

Figure 2.13 and 2.14 show a comparison of total efficiency and realized gain of a $\lambda/2$ rectangular slot and a CSR slot of outer diameter $0.229\lambda$ on the narrow-wall of a rectangular waveguide.

The narrow-wall CSR slot couples to the electromagnetic fields in the waveguide and radiates a linearly polarized wave with a radiation pattern similar to conventional rectangular slots. Its shown that the narrow-wall CSR slots are capable of acting as radiating elements for a slot array. The main advantage of the proposed slot is its small size (outer diameter of $0.23\lambda$) compared to the conventional rectangular slot. A rectangular slot with a length of $0.23\lambda$ does not couple to the waveguide

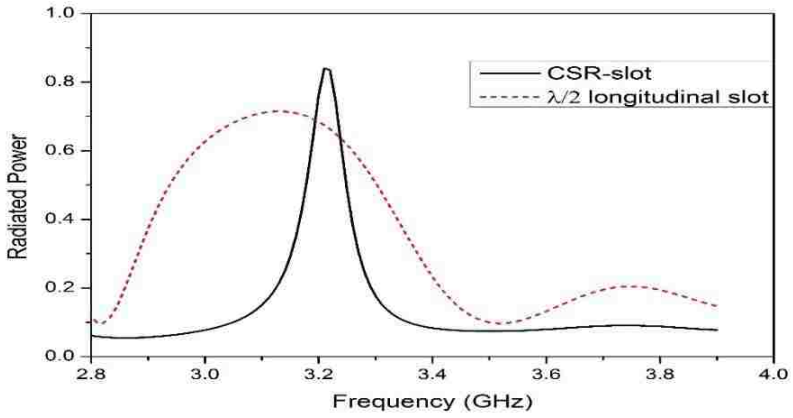


Figure 2.13: comparison of total efficiency of the rectangular slots and split ring slots.

electromagnetic fields well and, hence, essentially does not radiate efficiently.

Based on the presented parametric study on the geometrical parameters of narrow wall CSR slots, a CSR slot array is designed using the obtained S parameter results.

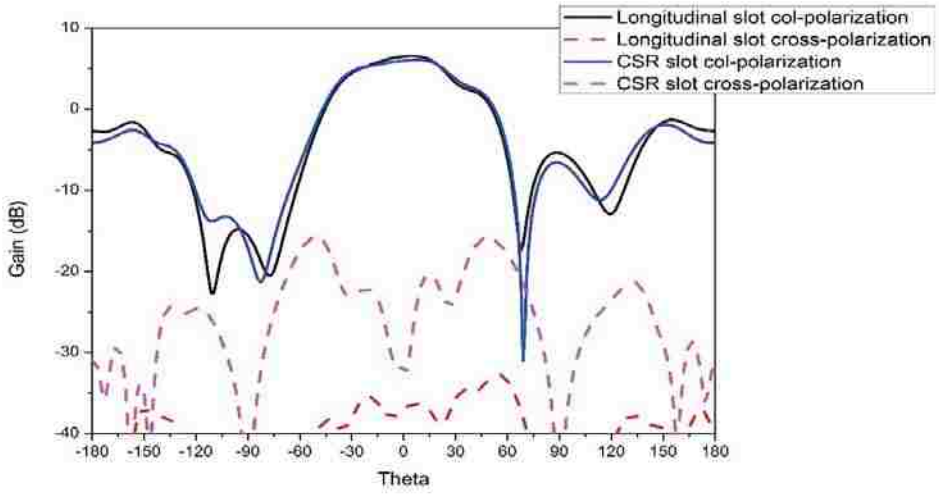


Figure 2.14: comparison of the gain of the rectangular slots and split ring slots.

# Chapter 3

# Complementary-split-ring slotted waveguide antennas

An illustration of the complementary-split-ring slotted waveguide antenna with an HPB-radiator ending is shown in Figure 3.1. This antenna is designed to incorporate CSR-slots on the narrow-wall of a rectangular waveguide into slotted waveguide antenna designs. The criteria for a proper high-power-microwave slotted waveguide antenna, such as minimizing reflected power and maximizing the directivity of its main lobe, still hold for this design.

The antenna consists of five radiating elements: four complementary-split-ring slots and an H-plane-bend radiator. The center-to-center distance between any two adjacent array elements is kept the same. The elliptical curved HPB-radiator provides a similar radiation pattern and half-sine-wave aperture electric-field distribution as the half-wavelength longitudinal slot [13]. It radiates in sync with the other slots, and also serves as a matched load for the waveguide antenna

with minimal reflected power.

To maximize the peak directivity of the array, the elements of the array are designed to radiate equal powers and possess a constant progressive phase shift so that the design forms a uniform array. In order to minimize the power reflected into the feed-waveguide, the power reflected into individual elements need to be destructively interfering. The optimal single-array design is a trade-off between minimizing the reflected power at the input of the array and designing a perfect uniform array.

Ideally, a matched load is preferred at the end of the waveguide instead of a shorting cap, to reduce the power reflected to the feed. An unmatched load might also generate a secondary canted beam from the broadside direction due to the wave reflected from the load. Thus, the HPB-radiator is a perfect fit for slotted waveguide antenna designs since it serves as a matched load and a radiating element at the same time. For an operating frequency of 3.1689GHz, the optimal length of the HPB-radiator is $47.335mm$ ($\lambda/2$), while the width of the HPB-radiator is the same as the width of the standard rectangular waveguide WR284, $34.04mm$. The number of elements in the single array is set to be five, to compare the design to the S-band longitudinal slotted waveguide antenna reported in [Xuyuan].

## 3.1 Microwave network design

Similar to the approach in [29][19], the idea of reducing the array design to a microwave network analysis that was introduced in [23], is applied in this analysis as well. The equivalent microwave network for the single array is shown in Figure

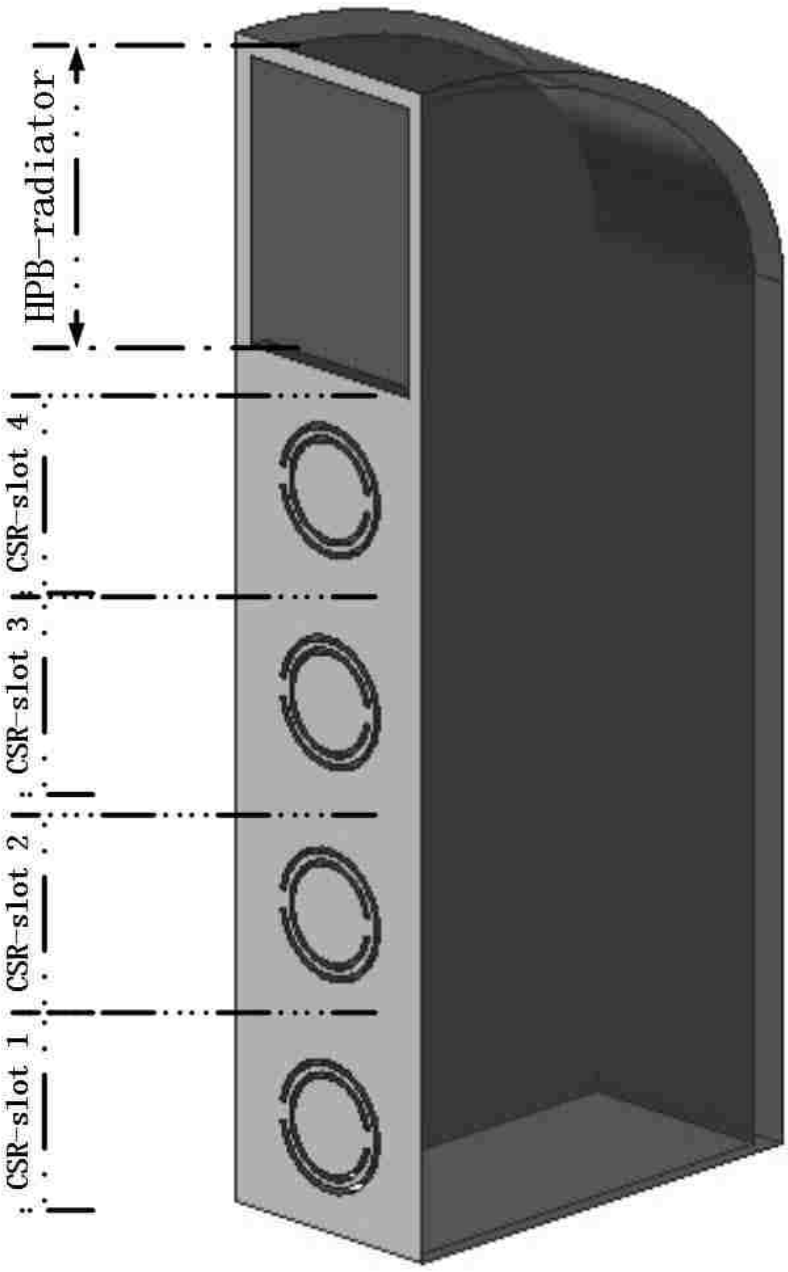


Figure 3.1: Schematic of the complementary-split-ring slotted waveguide antenna

3.2. This approach is based on the assumption that the external coupling between the array elements is negligible, which is acceptable in the case of the longitudinal slot array [19], where the inter-element spacing is $11/16\lambda_g$. However, such an assumption requires further validation in this CSR-slot study. Due to the much more compact slot size, the inter-element spacing can be reduced significantly. However, this means much stronger mutual coupling between the slots, which needs to be considered during the design process. Also, the CSR-slots are resonant structures, with very narrow bandwidth, and any interruption (i.e. mutual coupling from other slots) might result in a shift in resonant frequency, which consequently alters the S parameters of the slots.

Each CSR-slot is represented as a lossy 2-port network (slot 1 to 4) and the HPB-radiator is represented as a lossy 1-port network. The power radited by each slot (including the HPB-radiator) is represented by the loss in the corresponding network. The power radiated by slot $n$ is defined as $P_{rad(n)}$, where $n$ takes the integer number of 1 to 5. The power input to the $n$th lossy network is defined as $P_{in(n)}$. The reflection coefficient of the $n$th lossy network is defined as $\Gamma_n$. The power accepted by the $n$th lossy network is defined as $P_{load(n)}$, and is reprensented in.

$$P_{load(n)} = P_{in(n)}(1 - |\Gamma_n|^2) = \sum_{m=n}^{5} P_{rad(m)} \tag{3.1}$$

As a perfect uniform array, each element radiates equal power ($\frac{1}{5}P_{in}$, in the case of 5 elements array). Ideally, the optimal values of the ratio of the radiated power ($P_{rad(1)}$ through $P_{rad(5)}$) to the input power ($P_{in(1)}$ through $P_{in(5)}$) are given by $0.2P_{in(1)}$, $0.25P_{in(2)}$, $P_{in(3)}/3$, $0.5P_{in(4)}$, $P_{in(5)}$, respectively. Expressions for $P_{rad(1)}$ through $P_{rad(5)}$ and $\Gamma_n$, in Figure 7 are obtained in terms of the S-parameters of the array elements, inter-element spacing, and $P_{in(1)}$ using standard microwave network

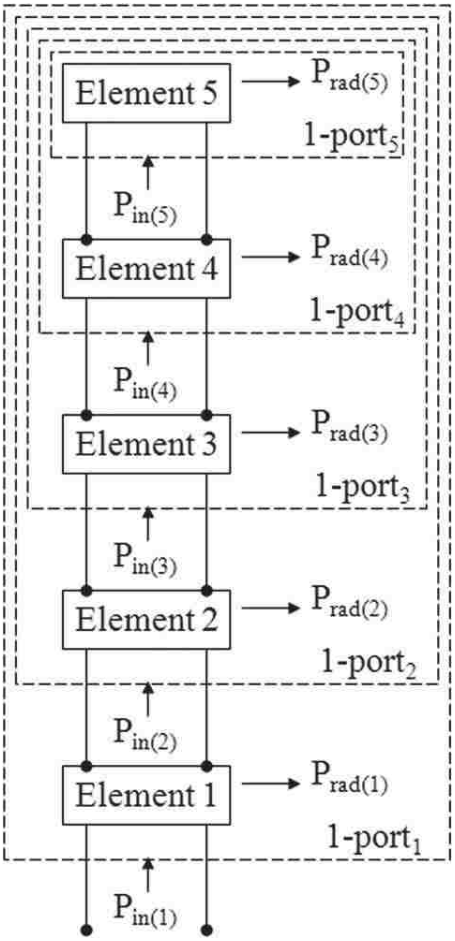


Figure 3.2: Equivalent microwave network of the slot array

analysis [13][18].

$$\Gamma_n = S_{11} + \Gamma_{n+1} S_{12} \left(\frac{S_{21}}{1 - \Gamma_{n+1} S_{22}}\right) \tag{3.2}$$

$$P_{in(n)} = P_{in(n+1)} \left| \frac{1 - \Gamma_{n+1} S_{22}}{S_{21}} \right|^2 \tag{3.3}$$

$$\sum_{m=n}^{5} P_{rad(m)} = P_{in(n)} (1 - |\Gamma_n|^2) \tag{3.4}$$

The longitudinal slot array design in [13][18] used more practical optimization

criteria: 1) the mean offset between $P_{rad(1)}$ through $P_{rad(5)}$ was minimized; 2) the reflected power at the input $< 5\%$ of the input power; 3) the mean error in the progressive aperture phase shift $< 5°$. However, for complementary-spilt-ring slots, its complicated to define the corresponding aperture phase, while the aperture phase of a conventional longitudinal slot can easily be defined as the phase of the aperture electric field at the center of the slot. Thus, only the first two criteria are taken into account in the microwave network analysis of the equivalent CSR antenna.

An important assumption is made that if the array of CSR-slots and the array of longitudinal half-wavelength slots can be characterized as the same microwave network, the radiation properties of both arrays should be similar, if not identical. This assumption is based on the parametric study of the CSR-slots and radiation characteristics of the CSR-slots, which show similar total efficiency, gain, polarization as well as radiation patterns to the conventional longitudinal slots. This assumption also requires further validation based on numerical full-wave analysis.

Figure 3.3: Comparison of the CSR-SWA with the longitudinal slot array (same inter-element spacing)

Based on this assumption, the inter-element spacing is set to be $11/16\lambda_g$, so that the design of the S-band longitudinal narrow wall slot array can be applied, as shown

| Element | $R/mm$ | $w/mm$ | $g_{sr}/mm$ | $\alpha/^\circ$ |
|---|---|---|---|---|
| slot 1 | 10.828 | 1.029 | 1 | 15.0 |
| slot 2 | 10.842 | 0.955 | 1 | 14.9 |
| slot 3 | 10.842 | 1.029 | 1 | 14.9 |
| slot 4 | 10.842 | 1 | 1 | 14.8 |

Table 3.1: Results from microwave network analysis

in Figure 3.3. Using the optimal values of $P_{rad(1)}$ through $P_{rad(5)}$, and corresponding S parameters of each microwave network, the optimal dimensions for CSR slot 1 to 4 are shown in Table 3.1.

## 3.2 Complementary-split-ring slotted waveguide antenna

To verify our assumption, a full-wave analysis was conducted by ANSYS HFSS. The array was simulated by using the optimal dimensions of the slots obtained above and for an inter-element spacing of $11\lambda_g/16$. The total reflected power at the input of the array is $< 1\%$ of the input power. Figures 3.4 and 3.5 compare the radiation patterns of the CSR slot array and the longitudinal slot array (same inter-element spacing: $11\lambda_g/16$).

Clearly, there is a lot more room for reduction of the inter-element spacing of the CSR slot array compared to the half-wavelength longitudinal slot array. However, its a tradeoff between the reflected power, antenna miniaturization and radiation performance of the antenna, like gain, main beamwidth, sidelobe level, etc. Figure 3.6 presents the relation between the peak gain of the antenna and inter-element

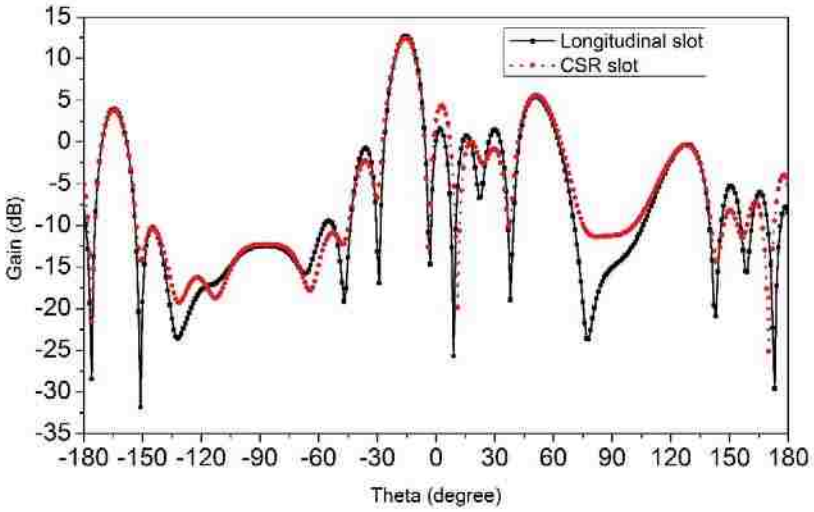


Figure 3.4: H plane radiation pattern of the the CSR slot array and the longitudinal slot array (same inter-element spacing: $11\lambda_g/16$)

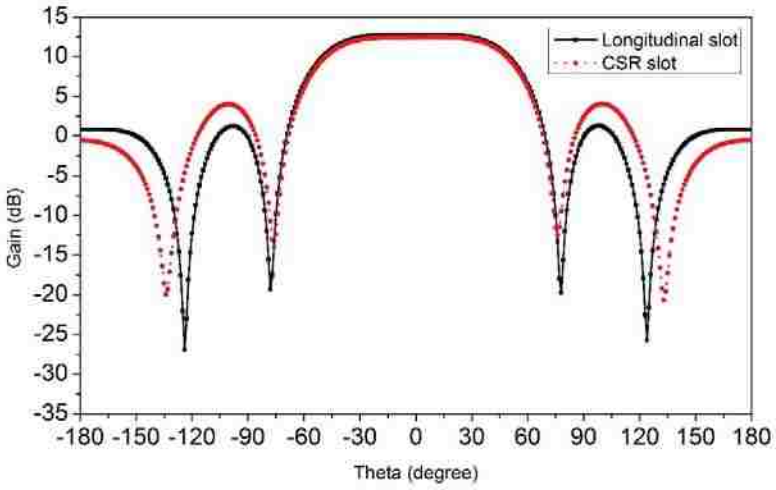


Figure 3.5: E plane radiation pattern of the the CSR slot array and the longitudinal slot array (same inter-element spacing: $11\lambda_g/16$)

spacing (in terms of guided wavelength).

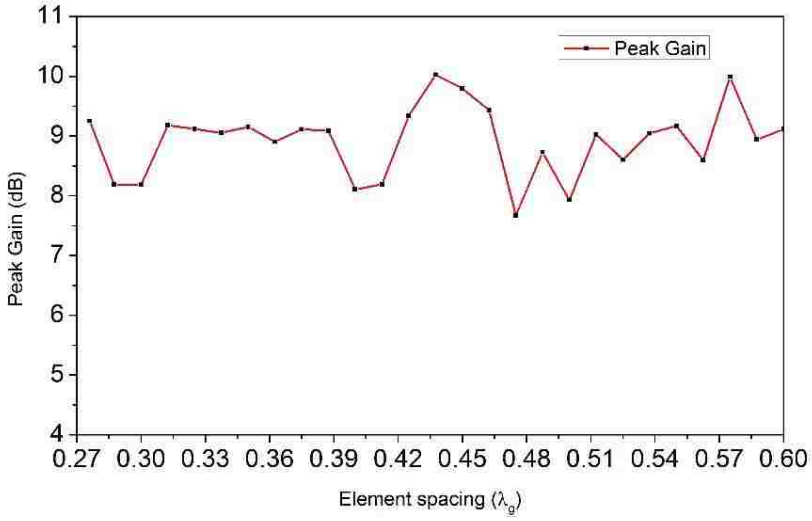


Figure 3.6: peak gain of the antenna vs inter-element spacing (in terms of guided wavelength)

There is no clear linear relation between the peak gain of the antenna and inter-element spacing between the CSR slots. The design of the complementary-split-ring slotted waveguide antenna is based on the trade-off between the antenna size and the antenna peak gain.

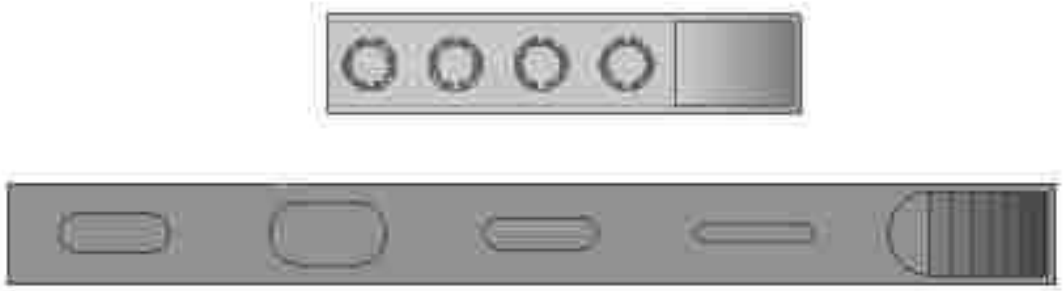

Figure 3.7: Comparison of the CSR-SWA with the longitudinal slot array

The final design uses an inter-element spacing of $0.2875\lambda_g$, as shown in Figure 3.7. It provides a return loss of $-30.77dB$, as shown in Figure 3.8. Figures 3.9 and 3.10 compare the radiation patterns of the CSR-SWA and the quarter-wavelength longitudinal slot array (same inter-element spacing: $0.2875\lambda_g$).

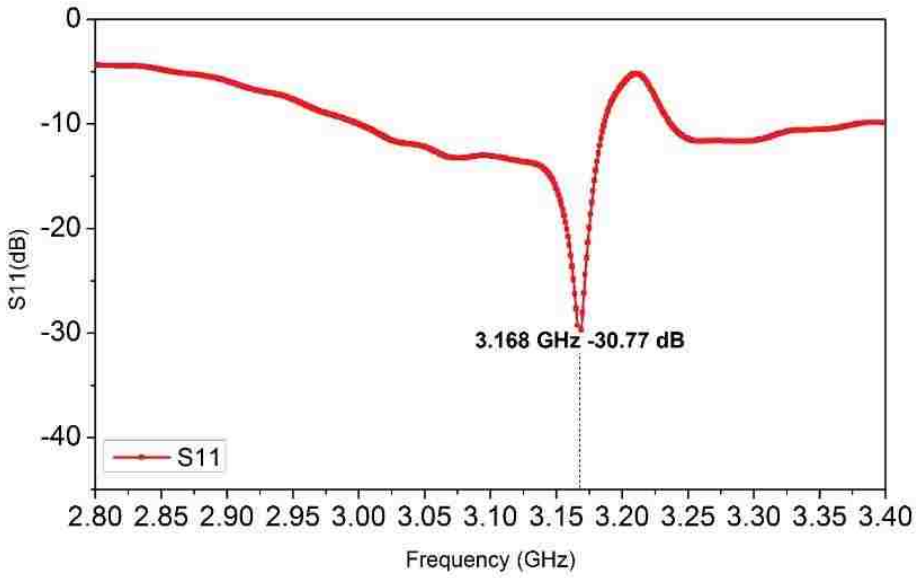


Figure 3.8: S parameter of the CSR-SWA

Field distribution across the CSR-slots are shown in Figure 3.11 with various delays of excitation at the input of the slot array . This also verifies that the design of the CSR-SWA is a quasi-uniform array even though the phase of each element of the array was not addressed in the design process.

The overall dimension of the proposed SWA is $187mm \times 74.14mm \times 34.04mm$, which is 55% less than the S-band narrow-wall slot array proposed in [18].

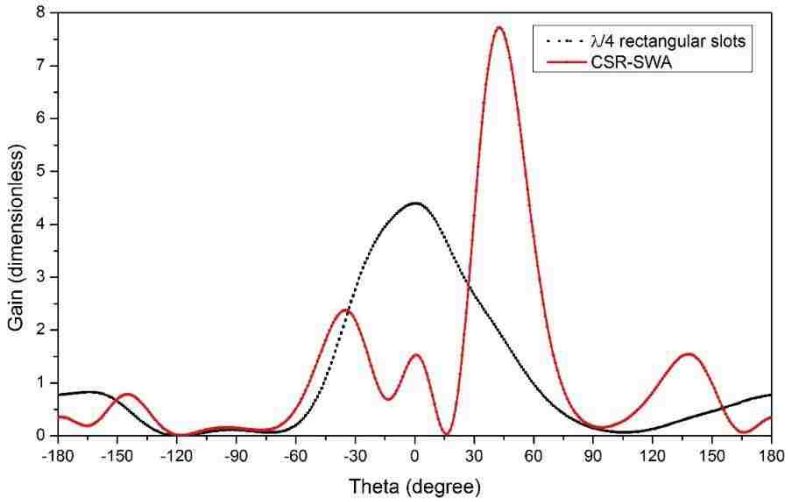


Figure 3.9: H plane radiation pattern of the CSR slot array and the $\lambda/4$ longitudinal slot array

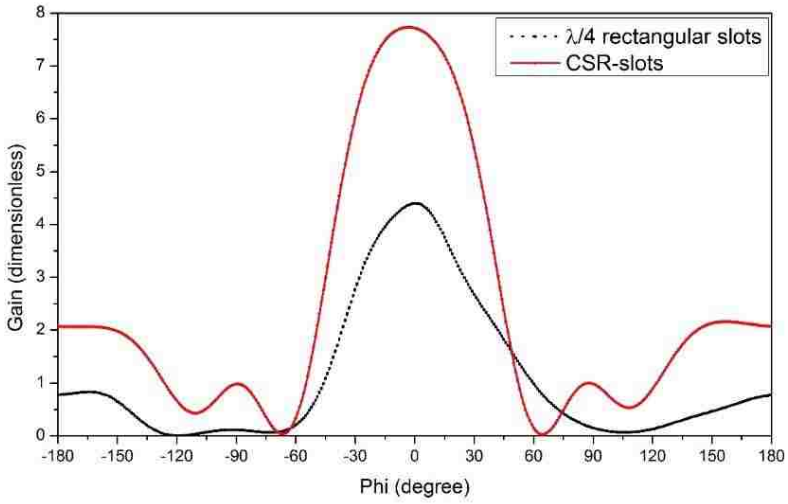


Figure 3.10: E plane radiation pattern of the CSR slot array and the $\lambda/4$ longitudinal slot array

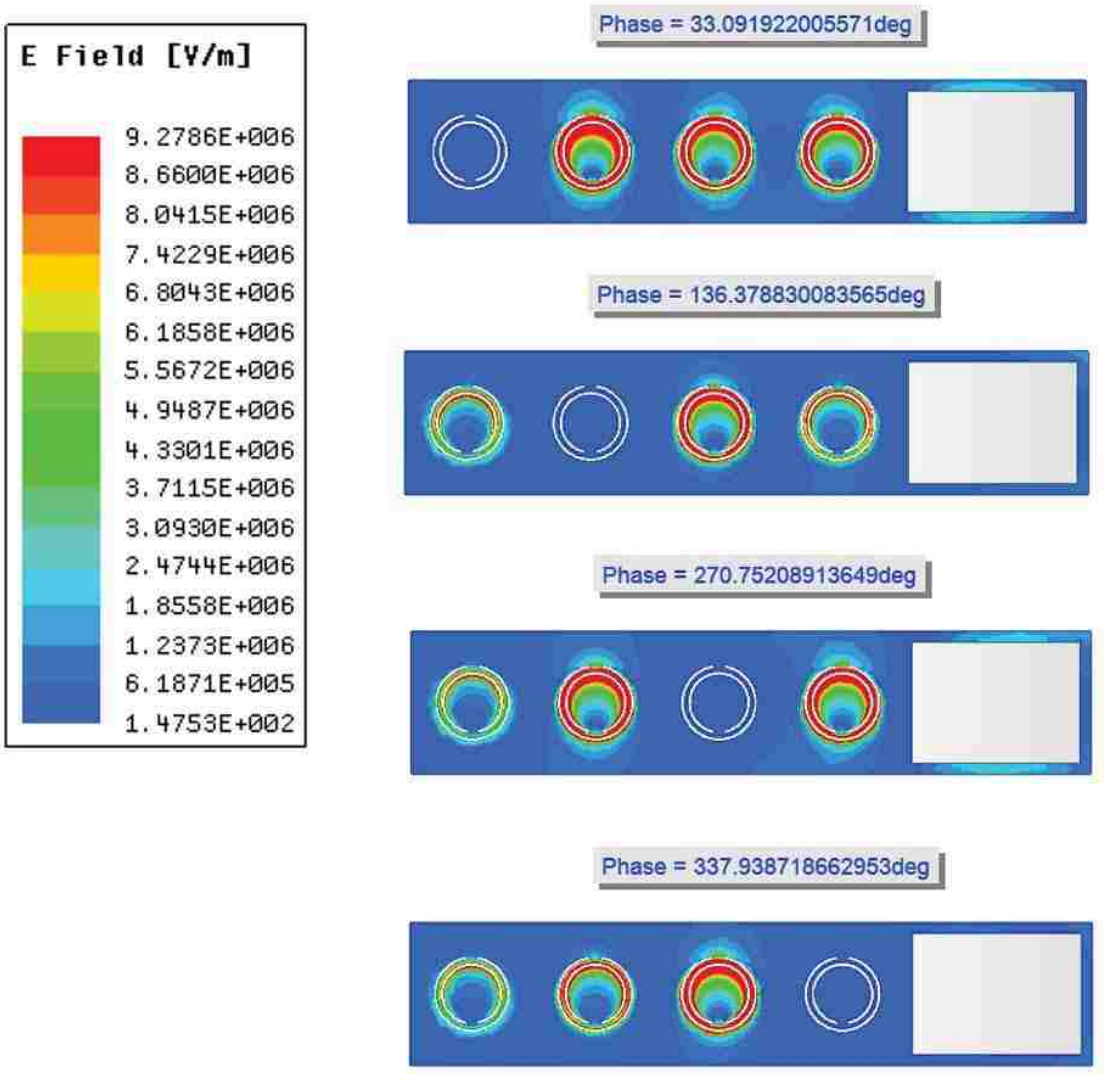


Figure 3.11: Electrical field across the narrow-wall of the CSR-SWA

## 3.3 Complementary-split-ring slotted waveguide antenna loaded with periodic air-filled corrugations

Due to the much closer center-to-center spacing, strong coupling is expected among the complementary spit ring slots. Thus, much thicker walls are used,

compared to standard WR284 waveguide. In this work, the thickness of the wall is set to be $3.175mm$ ($\frac{1}{8}in$). To further enhance the coupling between the wave propagating along the waveguide and the much deeper CSR slots, a set of periodic air-filled corrugations is added to the other (opposite) narrow-wall of the rectangular waveguide.

(a) 3D view

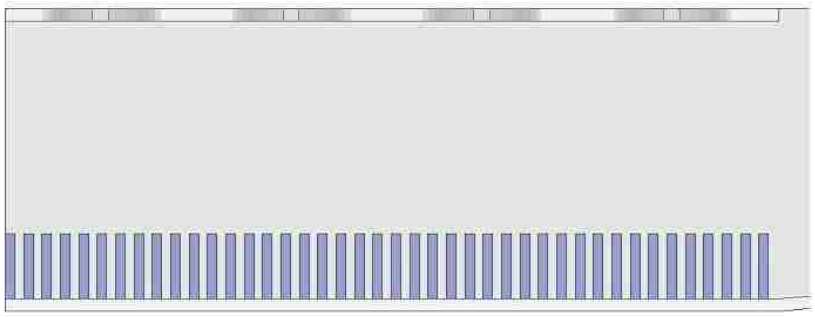

(b) side view

Figure 3.12: Periodic corrugations added to the other narrow-wall of the CSR-SWA

Figure 3.12 shows the basic schematic of the periodic air-filled corrugations added to the waveguide, which start at the input and end right before the HPB-radiator.

The height, length and inter-spacing of the periodic corrugations are optimized to enhance the coupling between the wave inside the waveguide and the CSR slots, which results in higher peak antenna gain. The optimal values obtained are shown in Table II.

Table 3.2: Corrugation dimension

| Height | Length | Inter-spacing |
|---|---|---|
| 16.97mm | 1.67mm | 1.67mm |

Figures 3.13 and 3.14 show the simulated radiation patterns of the narrow-wall CSR-SWAs loaded with periodic air-filled corrugations, compared to the narrow-wall CSR-SWAs without corrugations.

Based on the above results, we conclude that the complementary-split-ring slotted waveguide antenna has the advantage of being ***more compact*** compared to the

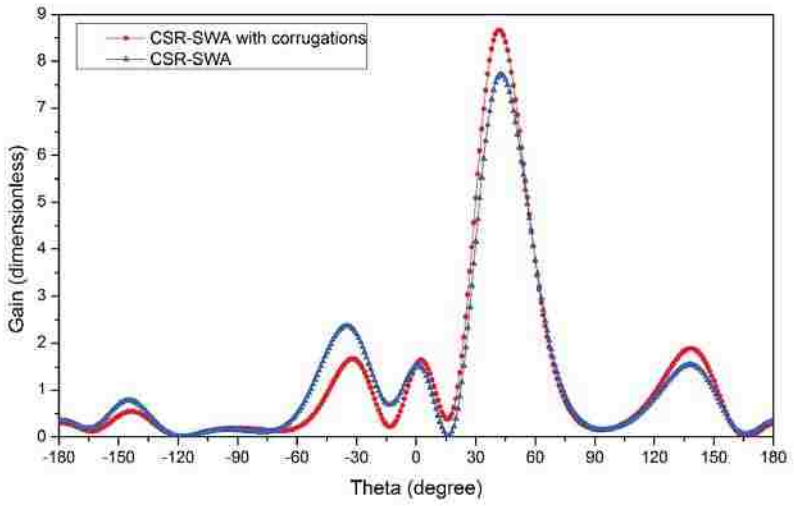


Figure 3.13: H plane radiation pattern of the CSR-SWA and the CSR-SWA loaded with corrugations

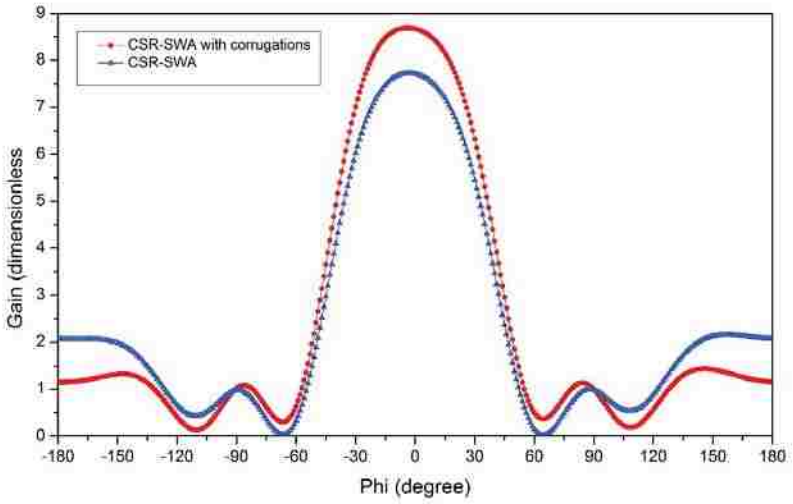


Figure 3.14: E plane radiation pattern of the CSR-SWA and the CSR-SWA loaded with corrugations

conventional half-wavelength longitudinal slot array and has ***better radiation performance*** (i.e. higher gain, narrower beamwidth) compared to the conventional quarter-wavelength longitudinal slot array.

## 3.4 Complementary-split-ring slotted waveguide antenna array

As mentioned before, the advantage of using complementary split ring slots instead of conventional longitudinal slots as radiating elements in slotted waveguide antenna designs is that the spacing between the radiating elements can be reduced due to the nature of the much smaller size of the CSR slots. In other words, given same dimension restriction, SWA designs using CSR slots can incorporate more slots

than using the conventional longitudinal slots, which potentially can improve the radiating characteristics of the antenna.

As an example, for the proposed design above, the center-to-center distance of the CSR-slots is set to be $0.2875\lambda_g$ while the original center-to-center distance of the longitudinal slots is $0.6875\lambda_g$. For a five-longitudinal-slots-array, maximum number of CSR-slots is $0.6875\lambda_g \times 4/0.2875\lambda_g = 9.6$. So for a similar dimension of the original longitudinal slot array, a CSR-SWA can be designed, consisting of 9 or 10 slots (8 or 9 CSR slots plus one HPB radiator), as shown in Figure 3.15. Ideally, it should give us better gain, more directive radiation pattern etc. However, to design an array of 8 or 9 CSR slots is a much more complicated process than simple rectangular slots, though the procedure can be followed in relatively straight-forward manner.

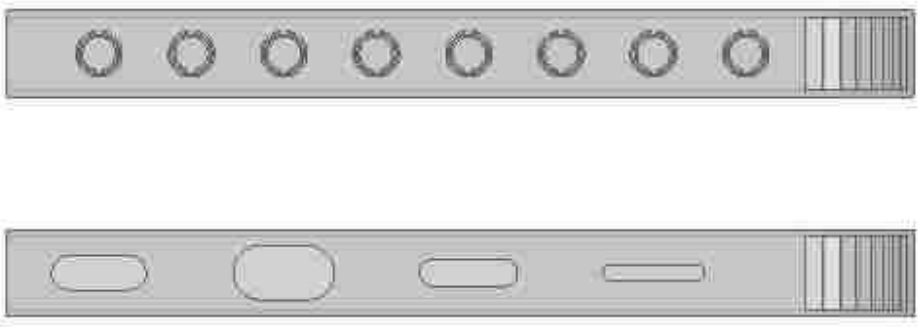

Figure 3.15: Comparison of longitudinal SWA and CSR-SWA (same dimension)

To prove the idea that more radiating elements in a similar slotted waveguide antenna dimension provide better radiating characteristics, we proposed an array of two complementary-split-ring slotted-waveguide-antenna, each of which consisting of

four CSR-slots and a HPB radiator, as shown in Figure 3.16.

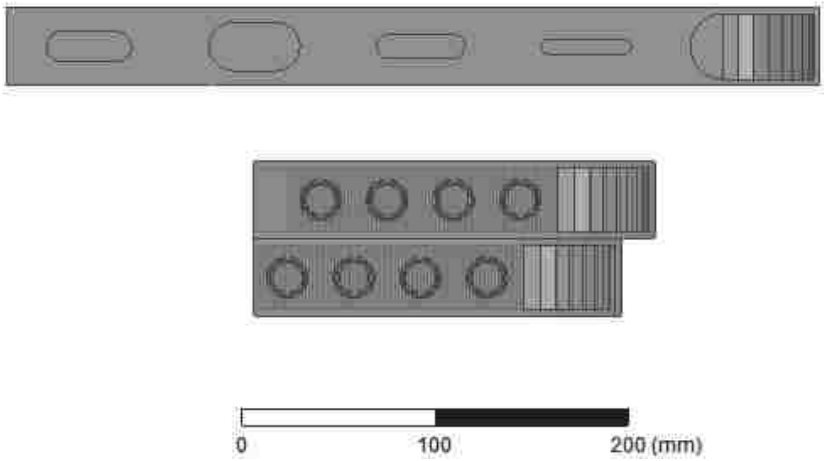


Figure 3.16: Comparison of the longitudinal SWA with the array of CSR-SWA (similar overall dimension)

The idea of putting two traveling wave narrow-wall slotted waveguide antennas adjacent to each other to reduce inter-element spacing, thus decreasing side lobe levels in the radiation pattern, has been shown in [70]. In [70], an array of two narrow-wall longitudinal slotted waveguide antenna was proposed. By controlling the phase of the input signal, it was shown that the grating lobe can be reduced.

A similar principle is applied here as the two complementary-split-ring slotted waveguide antennas are placed in a way to share a common broadwall. The slots are alternating from one side of the common wall to the other . However, due to the much stronger mutual coupling among the CSR-slots and much closer inter-element spacing, the ideal constant progressive phase shift between the radiating elements

unlikely exits, which is even hard to prove as mentioned earlier in microwave network analysis.

Recall the field distribution across the narrow-wall of the proposed CSR-SWA. In that particular case we concludes that the array was a quasi-uniform array. Based on the delay of the excitation signals, the progressive phase shift was estimated to be 98°. Thus, the ideal phase difference imposed on the exciting signal should be $0.2875/2 * 360° - 98°/2 = 2.75°$, which would give a quasi-uniform phase distribution across all apertures along the broad-wall. However, simulation results suggests a rather different scenario as the radiation pattern suggests a non-uniform array. This confirms the assumption that the ideal constant progressive phase shift between the radiating elements unlikely exits . To find an optimal phase delay between the exciting signals at the two input ports, a parametric sweep was performed. Its shown that when the phase delay between the two input ports is 6.5°, the array has an optimal radiation pattern.

Figure 3.17 and 3.18 show the gain radiation pattern of the array compared to the single longitudinal slotted waveguide antenna. The array clearly provides a narrower main beam and lower side-lobe level. The peak gain of the array is 11.75dB, very close to the peak gain of the single longitudinal slotted waveguide antenna (12.4dB).

Also, the CSR-SWA array provides a higher gain than the single CSR-SWA as expected. It also reduces the grating lob level which is significantly higher in the case of the single CSR-SWA than in the case of the longitudinal SWA. Figure 3.19 and 3.20 show the normalized radiation pattern of the array compared to the single longitudinal slotted waveguide antenna.

Thus, we conclude that for a similar antenna dimension, the design of slotted

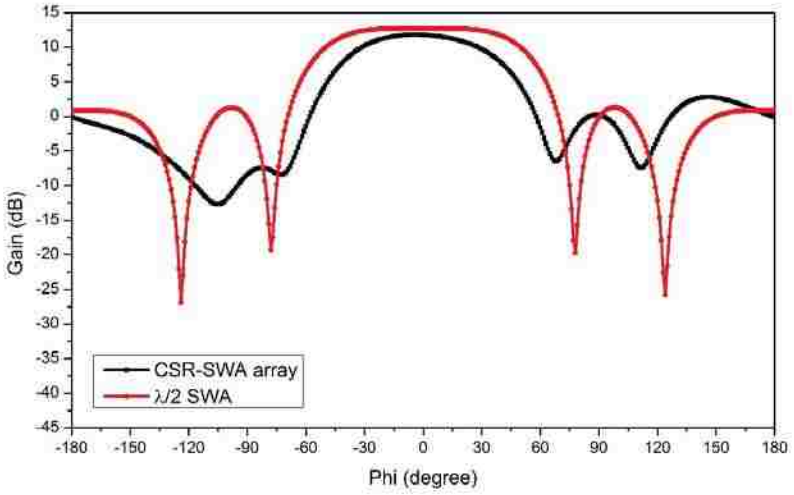


Figure 3.17: Comparison of the gain of the array of CSR-SWAs and the $\lambda/2$ longitudinal SWA (E-plane)

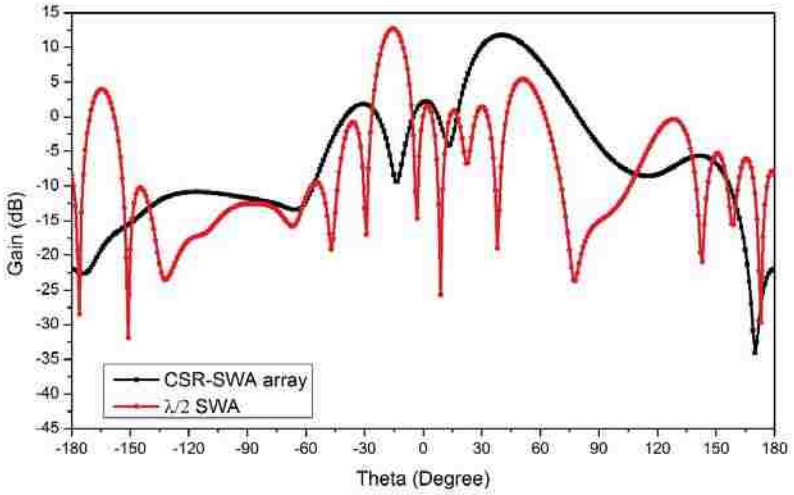


Figure 3.18: Comparison of the gain of the array of CSR-SWAs and the $\lambda/2$ longitudinal SWA (H-plane)

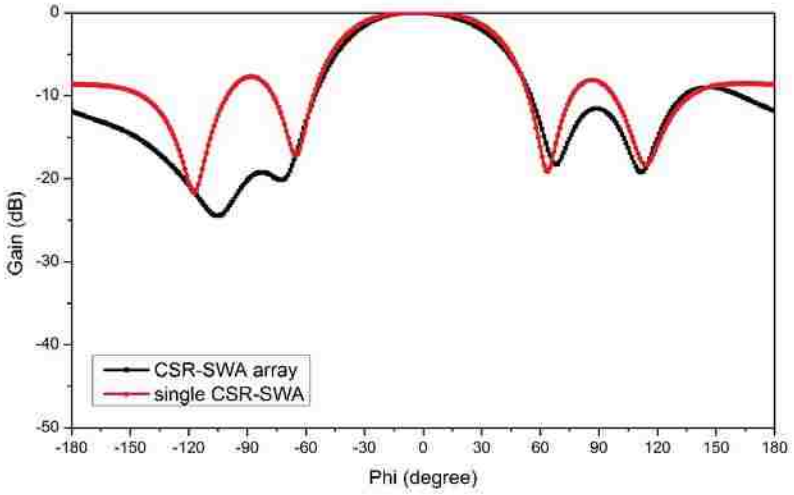


Figure 3.19: Comparison of the normalized gain of the array of CSR-SWAs and single CSR-SWA (E-plane)

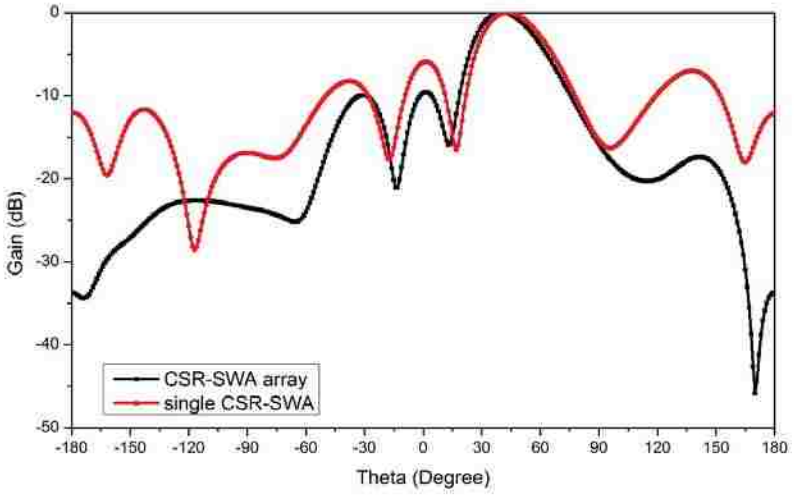


Figure 3.20: Comparison of the normalized gain of the array of CSR-SWAs and single CSR-SWA (H-plane)

waveguide antennas using CSR slots provides better radiation patterns while maintaining a similar peak gain compared the design that makes use of longitudinal slots instead.

# Chapter 4

# Power handling capability of the narrow-wall slotted waveguide antenna

High-power-microwave antennas are designed to withstand as much input power as possible. Depending on the feeding HPM source (magnetrons, backward-wave oscillators (BWO), magnetically insulated line oscillators (MILO), Marx generators, etc.), HPM antennas can provide very intense electric field (E-field) levels at hundreds of meters covering narrow band to ultra-wideband spectrums [5]. Such antennas must be able to operate under input power of MW (even GW) level, without causing breakdown within the HPM system [71]. The power handling capability of HPM antennas is usually investigated through large signal experiments (hot tests). By gradually increasing the input peak power, the maximum input power can then be determined when breakdown within the experimental set-up is detected. However,

this approach is time consuming and costly. It also increases the risk of damaging various components of the system and shortens the life time of the antennas and other electronics, even though most high power microwave system components are built to be rugged and withstand high RF fields.

Furthermore, this traditional approach usually fails to provide feedback on where exactly the breakdown occurred in the system; whether it is within the antenna structure or during the radiating stage outside the antenna. Thus, it is almost impossible to improve the antenna design addressing the power handling capability. In this work, the power handling capability estimation in the process of antenna design is proposed, with the help of numerical analysis tools such as HFSS and CST. Two main breakdown mechanism were used to determine the maximum input power threshold: 1) air breakdown (outside the antenna) [72], 2) multipaction breakdown (inside the antenna) [31]. This proposed approach provides a better insight in the maximum input power threshold of the HPM antennas as well as to which mechanism contributes towards the breakdown which is key in determining how to optimize the antenna design to improve power handling capability.

Unlike the air breakdown mechanism, which has been well adopted by antenna engineers as the criteria for the high-power-microwave antennas breakdown, few research articles in literature address the multipaction breakdown phenomenon within high-power-microwave antennas, especially on slotted waveguide antennas. For a relatively long pulse source, the possibility of multipaction to occur increases significantly, and its effect on antenna performance cannot be neglected by antenna engineers. However, its quite difficult to determine the exact criteria for multipaction breakdown to occur in the system. Here, we investigate the criteria for multipaction breakdown on an S-band longitudinal slotted waveguide antenna designed for high-

power-microwave applications [73].

## 4.1 Power handling capability estimation of an S-band narrow-wall longitudinal slotted waveguide antenna

To find the limit of the electron population inside an S-band waveguide, we performed an estimation of the power handling capability of the S-band longitudinal slotted waveguide antenna proposed in [73], and compared the results with the hot test results, performed at the Air Force Research Laboratory in Albuquerque, NM.

### 4.1.1 Overview of the large scale signal experiment on the S-band narrow-wall longitudinal slotted waveguide antenna

The hot test was conducted in AFRL, Albuquerque, New Mexico, USA. The test setup for the hot testing of this antenna is shown in the block diagram of Figure 4.1

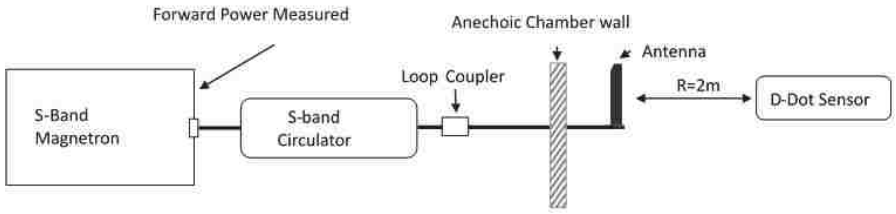


Figure 4.1: Block diagram of hot test setup


Figure 4.2: High power microwave source: S-Band Magnetron

as well as in the photographs of Figures 4.2 & 4.3.


Figure 4.3: Radiation pattern measurement setup inside anechoic chamber

The S-Band magnetron was located outside of an anechoic chamber as shown in Figures 4.1 and 4.2. The source power was fed through a patch panel in the chamber wall via an S-Band waveguide and then connected directly to the antenna inside the chamber. The magnetron used in these tests is tunable in frequency over a limited range and the frequency for these measurements was fixed at 3.0 GHz. The magnetron output power was varied from about 200kW up to just over 1 MW. The pulse duration was 500ns. Single pulse field measurements were made using a DDot sensor at a distance of 2 m from the antenna, in 5 degree increments along an arc in the H-plane as shown in the schematic of Figure 4.4.

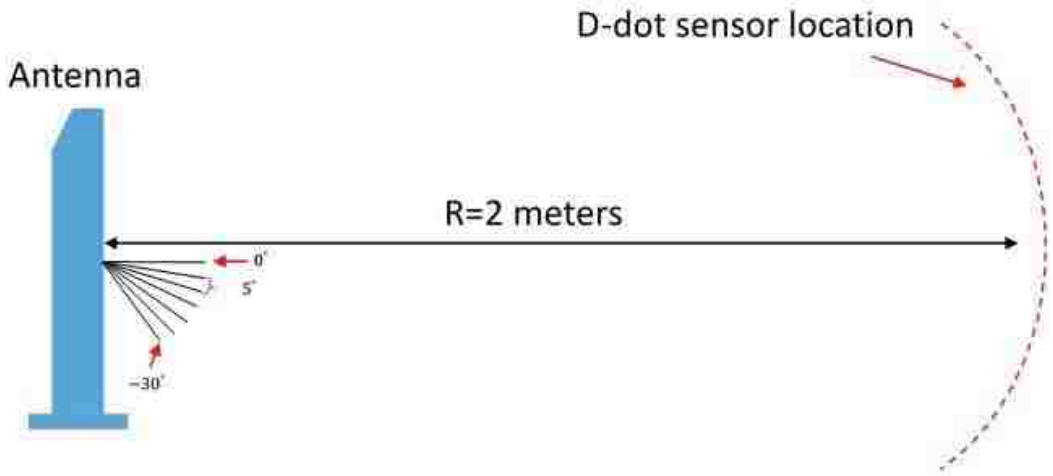


Figure 4.4: Diagram of H-plane radiation pattern measurements

Table 4.1 presents the measured gain of the antenna within the main beam. Figure 4.5 shows the comparison of the measured radiation pattern under both small and large signal conditions. Good agreement between the simulated radiation pattern and the measured main beam pattern were demonstrated within the main beam (region where the only experimental results could be obtained). With the input power as high as 0.813MW, no air break-down was observed.

| Position (degree) | Forward power(W) | Coupler power(W) | Gain(dB) | Simulated gain (dB)(f=3GHz) |
|---|---|---|---|---|
| -5 | 8.14E5 | 7.88E5 | -1.2 | -10.6 |
| -10 | 7.70E5 | 7.88E5 | -4.27 | 5.3 |
| -15 | 7.60E5 | 7.80E5 | 9.71 | 10.8 |
| -20 | 8.47E5 | 8.13E5 | 9.91 | 11.1 |
| -25 | 7.70E5 | 7.88E5 | 8.91 | 7.18 |
| -30 | 7.70E5 | 7.88E5 | -1.59 | -3.91 |

Table 4.1: ANTENNA GAIN WITHIN THE MAIN-BEAM

The tested S-band longitudinal slotted waveguide antenna is projected to have 1.8MW*19=34MW of output power, at the operating frequency of 3.17GHz. The slight drop in measured gain (9.91 dB instead of 12.49dB) shown in Table 4.1 is attributed to the operating frequency shift of the magnetron used in experiments,

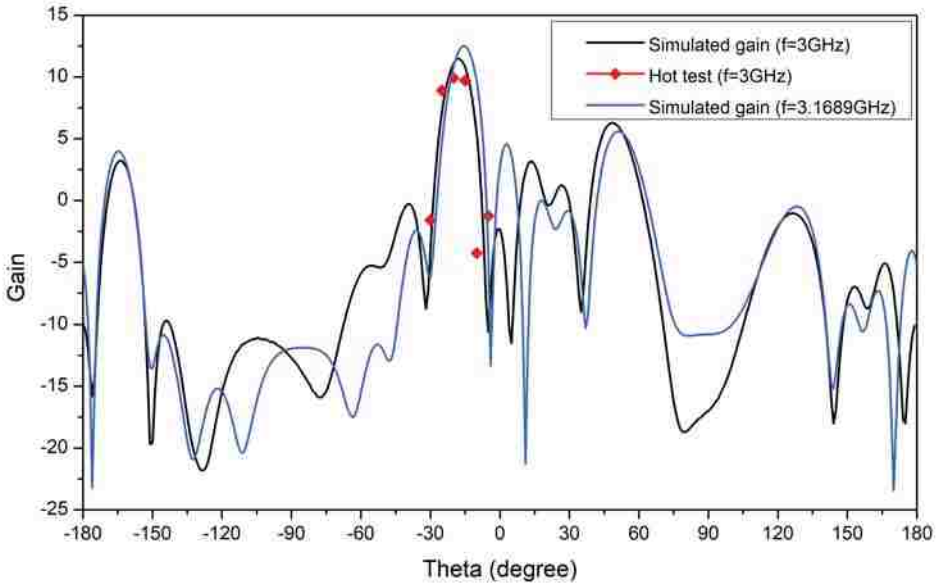


Figure 4.5: Antenna gain within the main-beam

which is 3 GHz instead of 3.17GHz. Even at the 3GHz, the antenna demonstrated an output power of 0.8*9.79=8MW. The S-band longitudinal slotted waveguide antenna is well suited for high-power-microwave applications.

### 4.1.2 Power handling capability estimation determined by air break down (outside the antenna)

The well-known electrical air breakdown value of approximately 3MV/m [74] for static fields at one atmosphere of air pressure is used as the upper limit for the maximum allowable E-field values. The air pressure at sea level is approximately one atmosphere, i.e. 760Torr. However, when antennas are operating at increasing altitudes above sea level, the value of air pressure falls, consequently, the electrical air breakdown values also falls [33]. Therefore, the maximum allowable power through the S-band feed-waveguide needs to be adjusted depending on the altitude at which the antennas are operating.

The pressure at an elevation of h meters above sea level can be computed using Equation 1.

$$p_h = p_0 e^{-\frac{h}{H}} \tag{4.1}$$

where $p_h$ is the air pressure at an elevation of $h$ meters above sea level; $p_0$ (=760 Torr) is the air pressure at sea level; $H$ (=8400 meters) is the approximate scale height of the Earth's atmosphere. According to the peek correction to Paschen law, the breakdown voltage is proportional to the relative density $\delta$ [33], as shown in Equation 2.

$$V(P, T, Hr) = \delta \times V(p_0, T_0, Hr_0) \tag{4.2}$$

Assuming same atmospheric condistions(i.e. temperature and humidity), the relative air density is $\delta = \frac{p_h}{p_0}$ [75]. Thus, the electrical air breakdown are proportional to the air pressure values, and can be computed through Equation 3.

$$E_{Br}(h) = \frac{p_h \times E_{Br}(h)}{p_0} \tag{4.3}$$

where $E_{Br}(0)$ (=3 MV/m) is the breakdown E-field value for static fields at one atmosphere air pressure. $E_{Br}(h)$ is the breakdown E-field value for static fields at an air pressure of $p_h$.

Next we illustrated how the power handling capability of a high power antenna is affected by the location of operation, which should always be considered during the antenna design process. Consider, for instance, that the antenna operates in Albuquerque, New Mexico, U.S.A. at an elevation of approximately 1610 meters above sea level. From Equation 1, the air pressure in Albuquerque is approximately equal to 627.44 Torr. This air pressure is in the range of values mentioned previously for which Equation 2 is valid. The corresponding air breakdown value in Albuquerque is computed from Equation 2 and is approximately equal to 2.48MV/m.

ANSYS HFSS was used to monitor the near-field radiation of the S-band longitudinal slotted waveguide antenna driven by various input power levels. Figure 4.6 shows the side view and the top view of the E field distribution of the S-band longitudinal slotted waveguide antenna simulated in HFSS. The top view of the E-field distribution was extracted on a surface just above the slots (about 0.1mm). It should be noted that the value of the maximum E-field in the near-field region is exactly linear to the square root value of the input power. Such values were recorded and used to determine the maximum input power, as shown in Table 4.2.

For the S-band longitudinal slotted waveguide antenna operating at 3.17GHz in

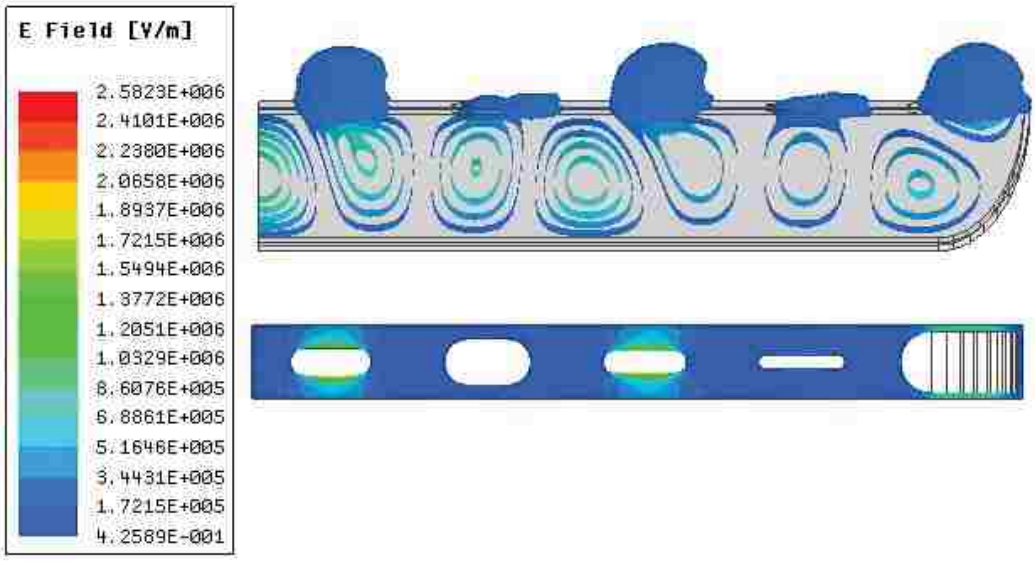


Figure 4.6: E field distribution simulated by HFSS

Albuquerque, NM, U.S.A., an input power of approximately 1.8MW through the S-band feed-waveguide would produce electrical field stronger than the threshold of 2.48MV/m, thus causing air breakdown.

Another factor that is key to the threshold of the input power is the dielectric material used to seal the antenna. For instance, a 5mm thick dielectric slab that covers the narrow-wall slots could significantly increase the maximum input power threshold without causing air breakdown.

| Input power (W) | 1E3 | 1E6 | 1.8E6 | 10E6 |
|---|---|---|---|---|
| $E_{max}$ (V/m) | 5.67E4 | 1.89E6 | 2.4E6 | 5.67E6 |

Table 4.2: Maximum E-field value based on HFSS simulation

### 4.1.3 Power handling capability estimation determined by multipaction break down (inside the antenna)

Multipaction is an RF vacuum breakdown mechanism, where an electron avalanche-like discharge occurs in structures operating under vacuum conditions and high-power electromagnetic fields [31]. The intensity of the applied field is such that the electrons are bombarding the walls, and if the kinetic energy of the impacting electrons is high enough, secondary electrons may be released from the walls. In such a way, the process can sustain itself, causing continuous growth of the population of the electron inside the device as illustrated in Figure 4.7. The discharge is mainly encountered in RF accelerating structures where the combination of RF fields and clean surfaces of high secondary yield metals like copper, aluminum, or niobium will increase the number of electrons at each impact.

According to recent literature on multipaction studies, once the RF fields are high enough to sustain the continuous growth of electron population as mentioned above, the electron population is expected to grow until a steady-state (saturation level) is reached [76]. Two main mechanisms are behind the form of such steady-state: 1) the accumulated electrons produce an electrical field that cancels out the applied electrical field, leading to saturated electron population; 2) the space charge effect among the accumulated electrons results in a steady electron cloud. Such an electron cloud/bridge could create an unwanted short path within the system. Either way, the operation of the RF system can be disrupted by saturated multipaction, which is generally considered as the criteria for multipaction breakdown during multipaction prediction.

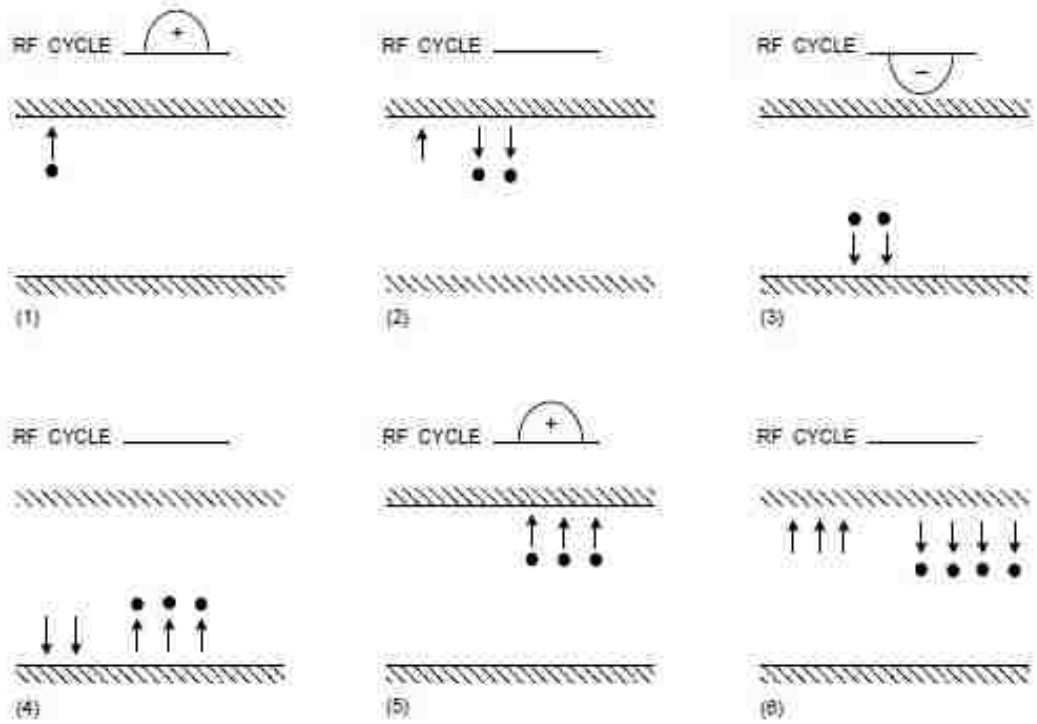


Figure 4.7: Electron discharge leading to multipaction

Several models have been used to study multipaction saturation status. Depending on the particular characteristics of the case (waveguide dimensions, SEY properties, RF voltage), the saturation level is within the range of $10^9 - 10^{12}$ electrons between two parallel metal plates separated by 1mm according to [77]. However, it is difficult to determine the saturation level for the electron population inside a slotted waveguide antenna structure, especially for a relatively large waveguide WR284, with a cross-section of dimension of 72.16mm*34.04mm. Most studies in literature focused on two parallel plates systems. It is shown in [78] that for the coaxial waveguide considered (inner radius 2mm, out radius 3mm, 100mm long), numerical simulations based on a saturation level of $10^{12}$ fit the experimental data. Less studies have

been done on multipaction saturation inside rectangular waveguides, thus, we took an educational guess, the saturation level of the S-band slotted waveguide antenna, $N_{sat}$, is approximately $10^{12} * \frac{74.14*34.04*416}{\pi*(3^2-2^2)*100} \approx 10^{15}$.

Different numerical simulation codes are used for predicting multipaction. Every code has certain set of advantages coupled with certain limitations. Most numerical simulation codes are 1D and 2D and use a semi-empirical approach derived by Vaughan [79]. Some other codes use macro-particles instead of individual electrons, where a large number of electrons are located at the same point, with identical momentum. The use of macro-particles means that information about the energy distribution cannot be accurately resolved and that the statistical nature of electron reflection and emission is at best integrated over and smoothed out. For design and analysis of RF structures with complex geometries and non-uniform electromagnetic fields, it is required to use a numerical simulation tool that combines electromagnetic field simulation, multi-particle tracking and advanced probabilistic emission models.

The well-known CST particle studio (PS) [80] simulation tool has the following advantages for realistic multipaction simulations:

1. 1. Electromagnetic field calculation using CST Microwave studio can be directly imported to CST PS.
2. Multi-particle tracking using Particle-in-cell (PIC) solver.
3. Incorporates advanced emission model, introduced by Furman and Pivi [81]. This model is well adopted in the particle accelerator community due to the fact that it provides not only an SEY (second emission yield) curve but also the energy and angular distribution for the emitted electrons.
4. 4. Incorporates the flexibility to accommodate user defined inputs even

for the secondary emission model, such as initial particles distribution.

**Table A-6: Constants for the most used materials**

| Material | $\alpha_{max}$ [a] | E1 [a] | E2 [a] | Em [a] | Slope(a) | Slope(b) | Wf1 | Wf2 |
|---|---|---|---|---|---|---|---|---|
| Gold | 1,79 | 150 | 4000 | 1000 | 64,2 | 40,1 | 30,1 | 56,2 |
| Silver | 2,22 | 30 | 5000 | 165 | 62,4 | 37,9 | 32,4 | 59,1 |
| Aluminium | 2,98 | 30 | 5000 | 805 | 39,8 | 26,6 | 23,3 | 44,7 |
| Alodine | 1,83 | 41 | 5000 | 180 | 73,8 | 73,8 | 85,6 | 85,6 |
| Copper | 2,25 | 25 | 5000 | 175 | 54,1 | 54,1 | 37,1 | 37,1 |

$\alpha_{max}$ = maximum secondary emission coefficient (see A.4.1)
E1 = lowest incident electron energy at [ρ=1] (see A.4.1)
E2 = highest incident electron energy at [ρ=1] (see A.4.1)
Em = incident electron energy for $\alpha_{max}$ (see A.4.1)
Slope(a) = upper design boundary (see A.4.2.5)
Slope(b) = lower design boundary (see A.4.2.5)
Wf1 and Wf2 are work functions

[a] Data for silver and copper are from [1]. Data for aluminium and alodine are from [13].

Table 4.3: Constants for the most used materials [ref]

The input power threshold analysis is accomplished through the CST PIC solver. The material used here is copper (ECSS: European Cooperation for Space Standardization), predefined in the CST secondary electron emission (SEE) material library. Some common materials defined by European Space Agency(ESA) ECSS document are shown in Table 4.3 [80].

For the secondary emission yield curve, we used Furmans model [81]. Compared to the Vaughan model [79], which is more popular among the microwave community, Furmans model offers not only good agreement to measurements, but also flexibility to distinguish between re-diffused, elastic backscattered and true secondary electrons, as illustrated in Figure 4.8 and 4.9.

To save computer memory and time, only emission in the most critical parts of the antenna were investigated.

First, the slotted waveguide antenna structure was simulated in CST MWS to identify the most critrical areas. Next, using Maxwellian Particles Macro toolbox, the initial particle distribution was assigned to the designated area corresponding to the critical areas revealed by CST MWS simulation, as shown in Figure 4.10 and 4.11.

Electromagnetic fields simulated previously in CST MWS were imported, and the field amplitude was scaled to represent the input power as the CST MWS field monitor automatically normalize its results to the input power of 1W.

CST provides the option of setting solver stopper criteria to interrupt simulation in order to facilitate the simulation process, since the computing resource (i.e. RAM) required increases rapidly as the number of electrons during simulation increases. Such criteria are usually set as the speed of the electron population

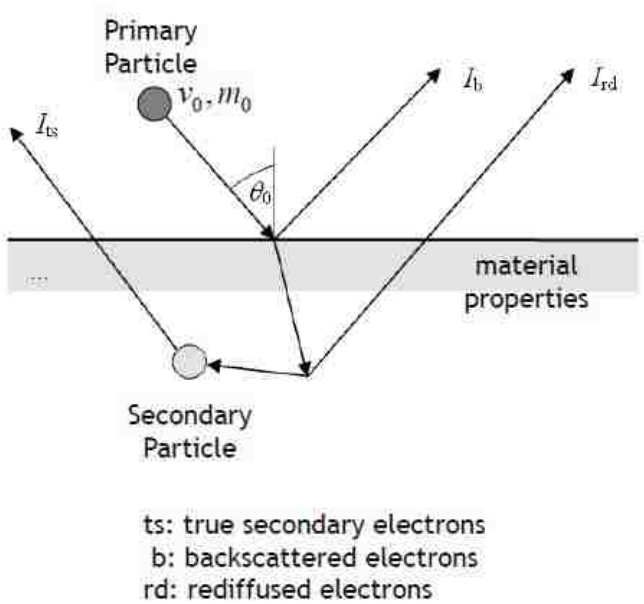


Figure 4.8: A primary particle hitting a metal surface

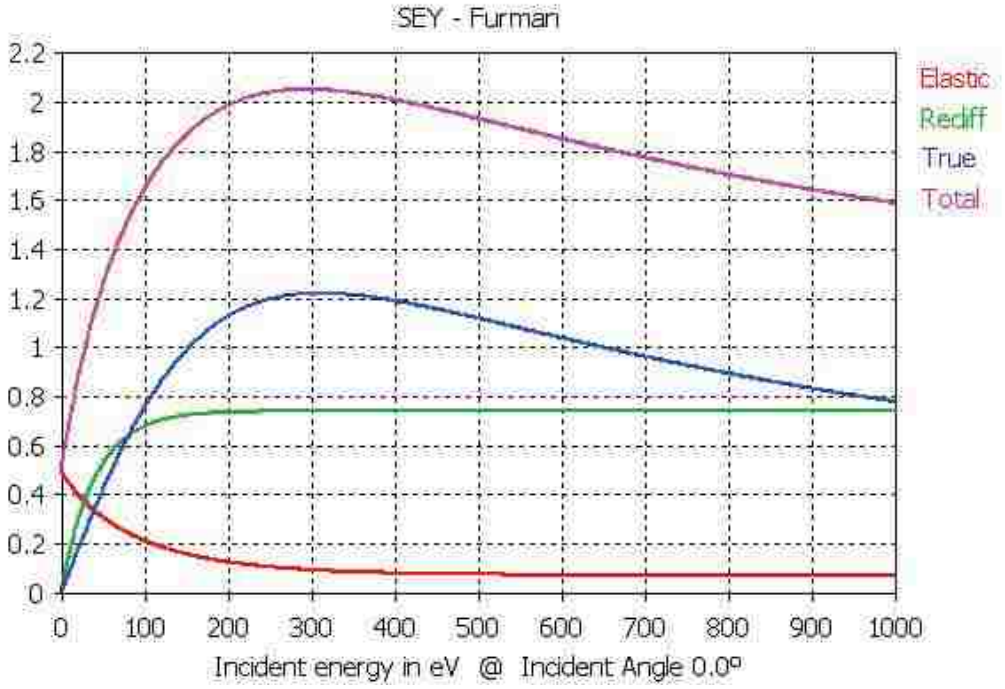


Figure 4.9: SEY curve Furman model [81]

growth exceeds the exponential growing rate. In a typical multipactor breakdown analysis/estimation, the time frame of the operation is long enough that whenever the speed of the growth of the particles surpasses exponential growth, the population of the particles will eventually reach the saturation level. However, for the case of the relatively long pulse duration in our simulation/experiment (500ns), there's no guarantee that the population of the free electrons will reach saturation level. This requires a full simulation over the whole operation time frame which increases the complexity of analysis.

To better predict the threshold of the multipaction power level and to reduce the overall simulation time, first, a quick classic input power threshold estimation was performed within a simulation duration of 20ns, The result is shown in Figure

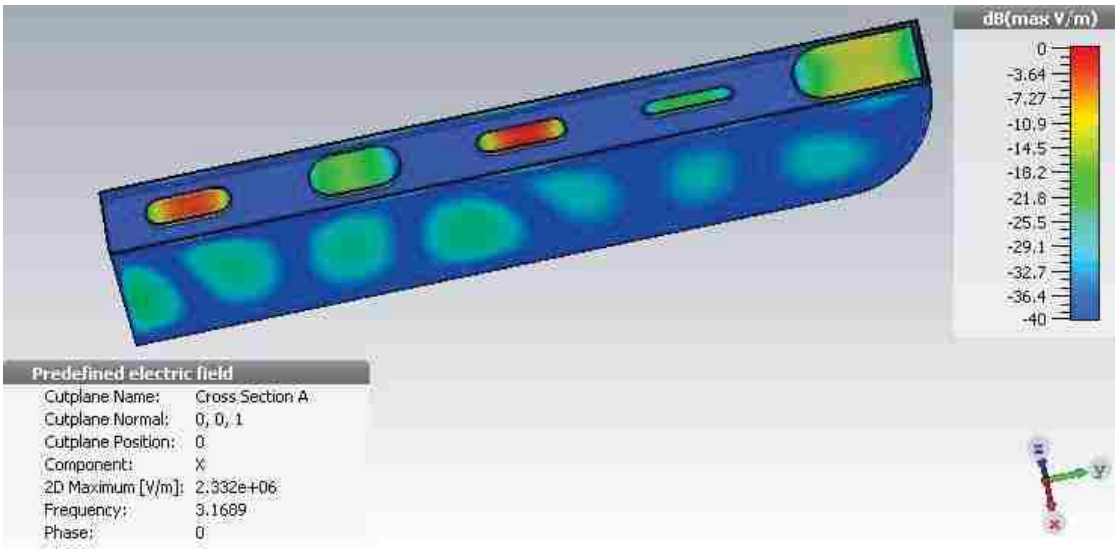


Figure 4.10: S-band longitudinal slotted waveguide antenna simulated in CST MWS.

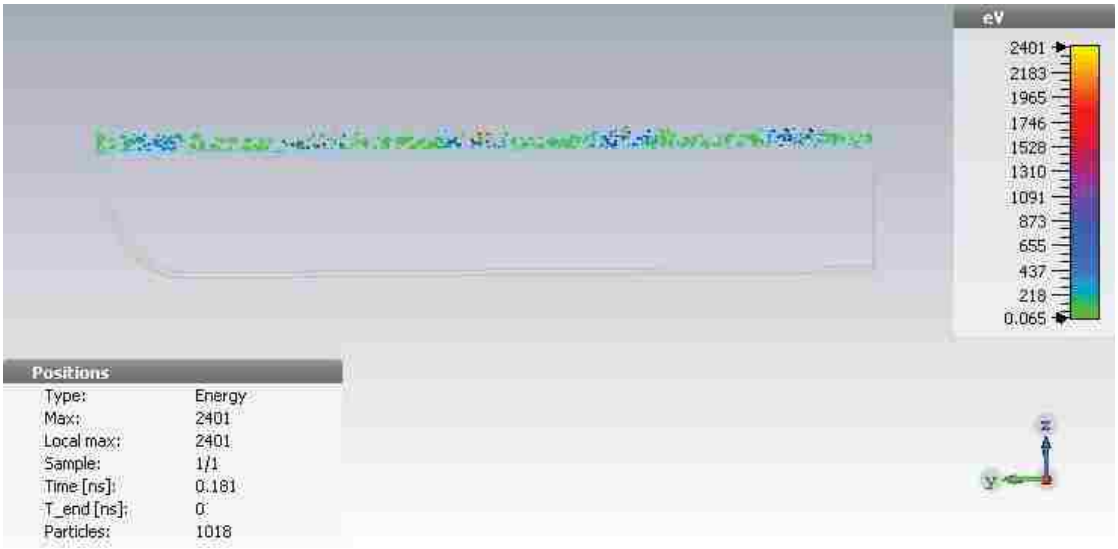


Figure 4.11: Initial electron distribution assigned to the S-band longitudinal slotted waveguide antenna in CST PS.

4.12, and it's quite clear that the threshold should be somewhere between 1.5MW and 2.5MW(3MW). Also, we can conclude from Figure 4.12 that around 0.8MW,

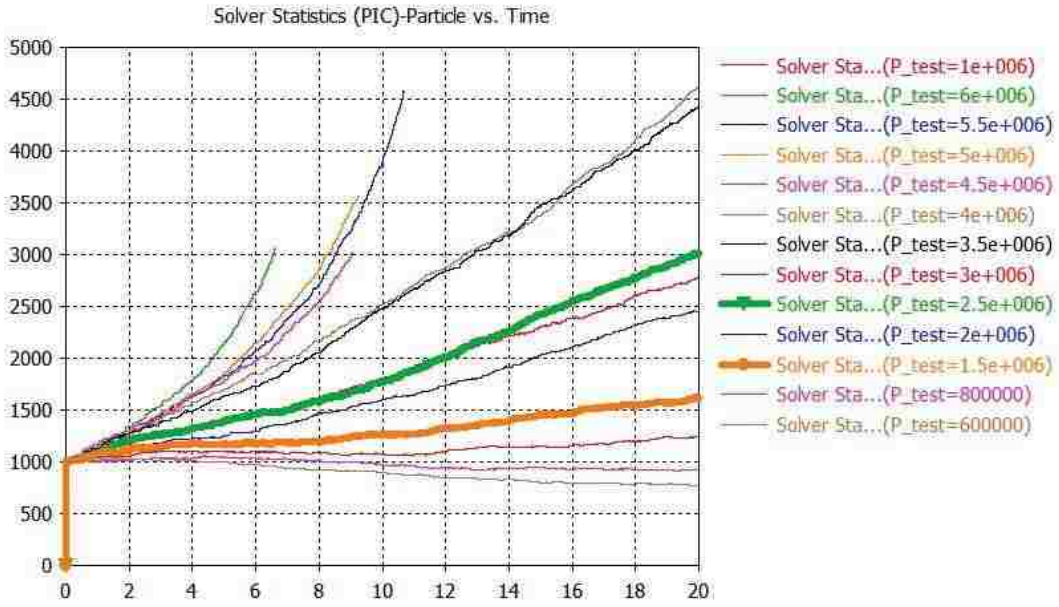


Figure 4.12: Power threshold estimation by CST PS.

the population of the particles shows no sign of growing, which indicates that no multipactor occurs around such input power level.

More thorough simulations were conducted next. We chose the input power to be 2.35MW, 2.54MW and 2.7MW respectively. Figures 4.13 and 4.14, show the population of secondary emitted electrons versus time and the population of total particles inside the antenna structure versus time, for various input power respectively.

The simulation time required for the pulse duration of a) 300ns for 2.35MW and b) 2.54MW and c) 250ns for 2.7MW are 45 minutes, 45 hours and 85 hours respectively. For the case of an input power of 2.75MW, the simulation was forced to stop shortly after 250ns of operation due to the fact that the computing resources we have were exhausted already as the population of the electrons exceeded 100

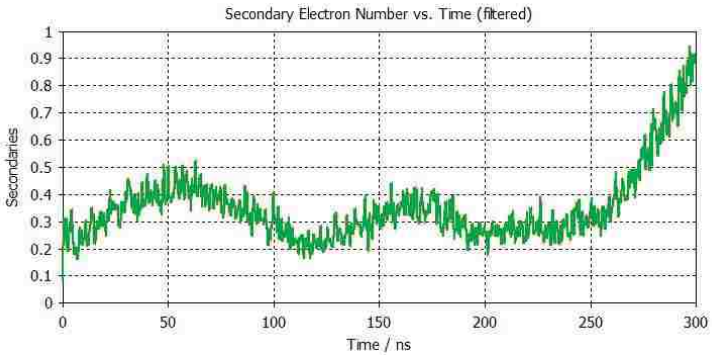


(a) Input power of 2.35 MW

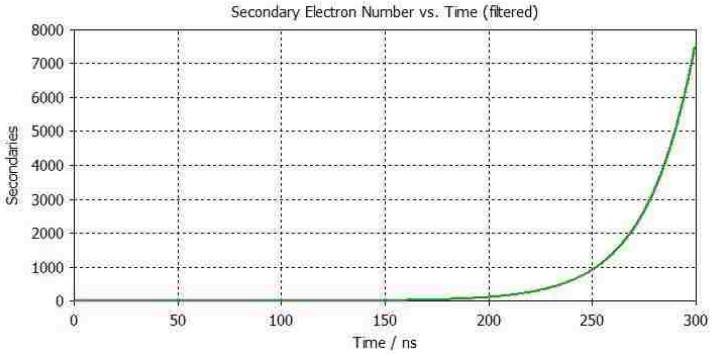


(b) Input power of 2.54MW

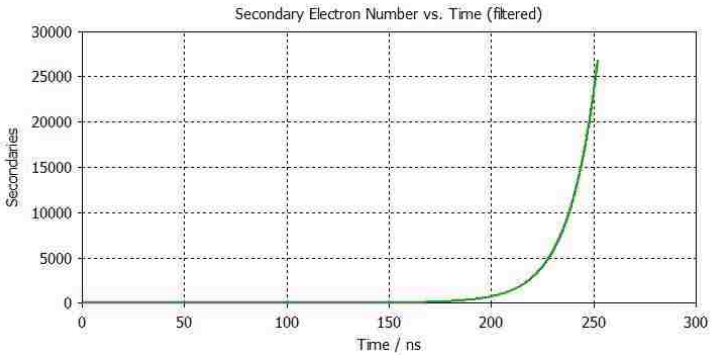


(c) Input power of 2.75MW

Figure 4.13: Population of secondary emitted electrons versus time inside the S-band longitudinal slotted waveguide antenna excited by a) 2.35MW, b) 2.54MW, c) 2.75 MW

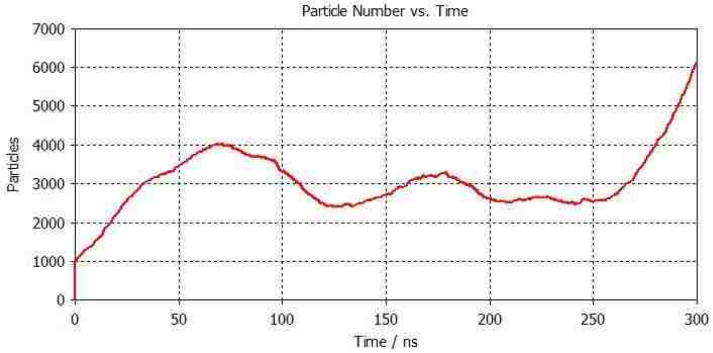


(a) Input power of 2.35 MW.

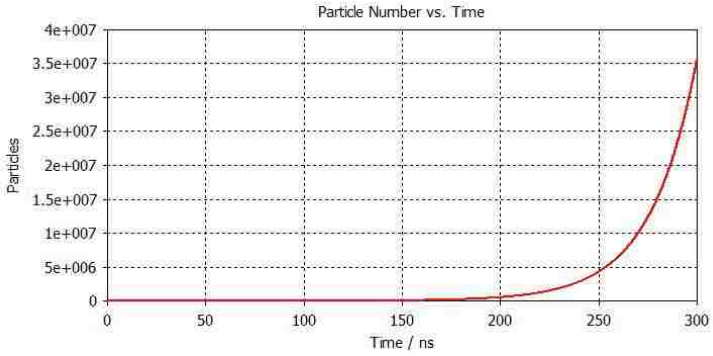


(b) Input power of 2.54MW.

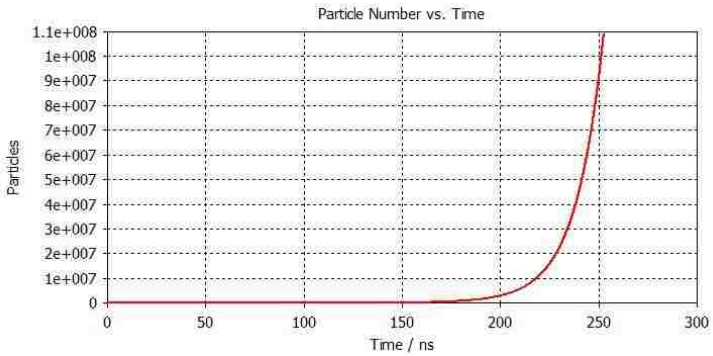


(c) Input power of 2.75MW.

Figure 4.14: Population of total electrons versus time inside the S-band longitudinal slotted waveguide antenna excited by a) 2.35MW, b) 2.54MW, c) 2.75 MW.

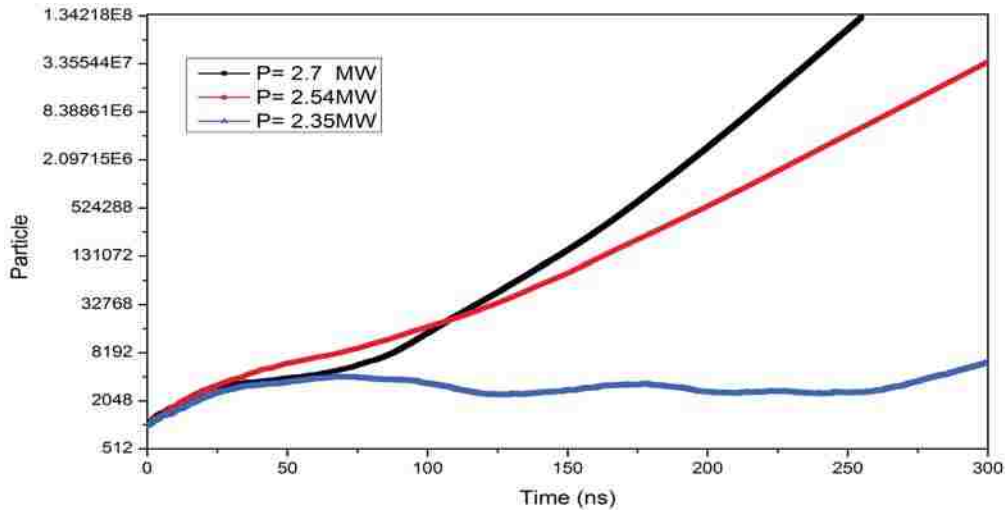


Figure 4.15: Population of total electrons versus time inside the S-band longitudinal slotted waveguide antenna excited by 2.35MW, 2.54MW and 2.75 MW, respectively.

million, as shown in Figure 4.15. However, such electron population is far from the saturation level.

Thus, for the case of a 500ns long pulse, a certain level of estimation is required to decide whether the population of the electrons reaches the saturation level during the whole process. The estimated electron populations are shown in Table 4.4 for various input power levels. When the antenna is excited with an input power of 2.75 MW, the particle population is projected to reach the saturation level of $10^{15}$ within 500 ns, while for an input power of up to 2.35 MW, the particle population is far from reaching the saturation level at the end of 500ns.

Figure 4.16 to 4.18 show the distribution of the electrons at T=300ns for an input power of 2.35MW and 2.54MW, and at T=250ns for an input power of 2.75MW.

Thus we conclude that the input power threshold for the S-band narrow-wall longitudinal slotted waveguide antenna is around 800 kW before multipaction occur

inside the antenna, and 2.35 MW before saturated multipaction reached.

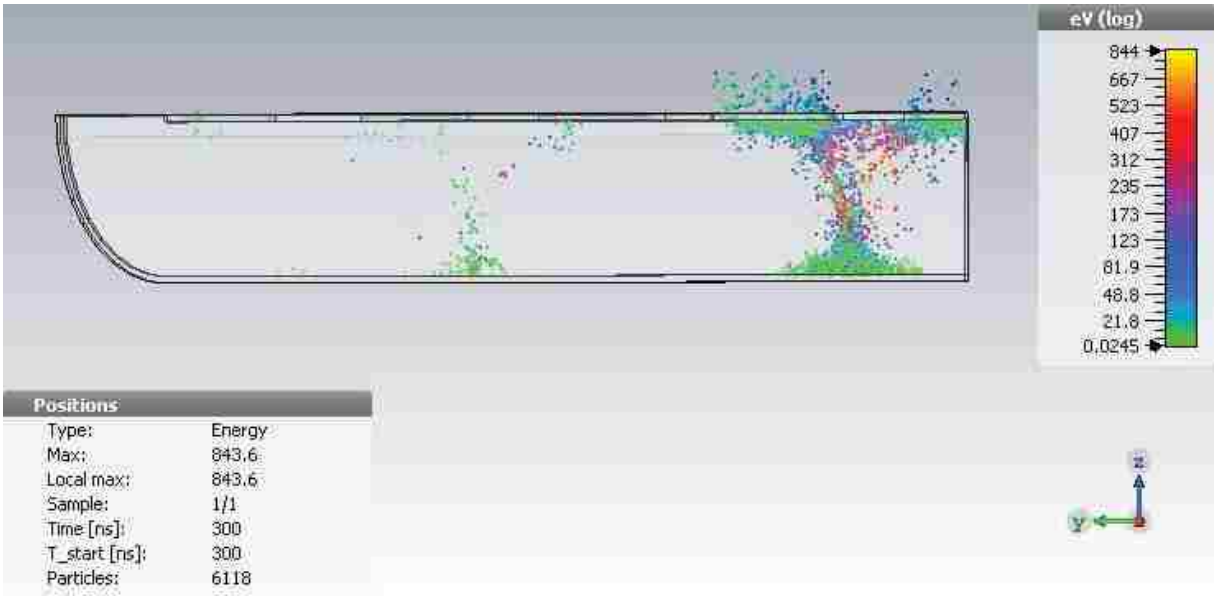


(a) Side view

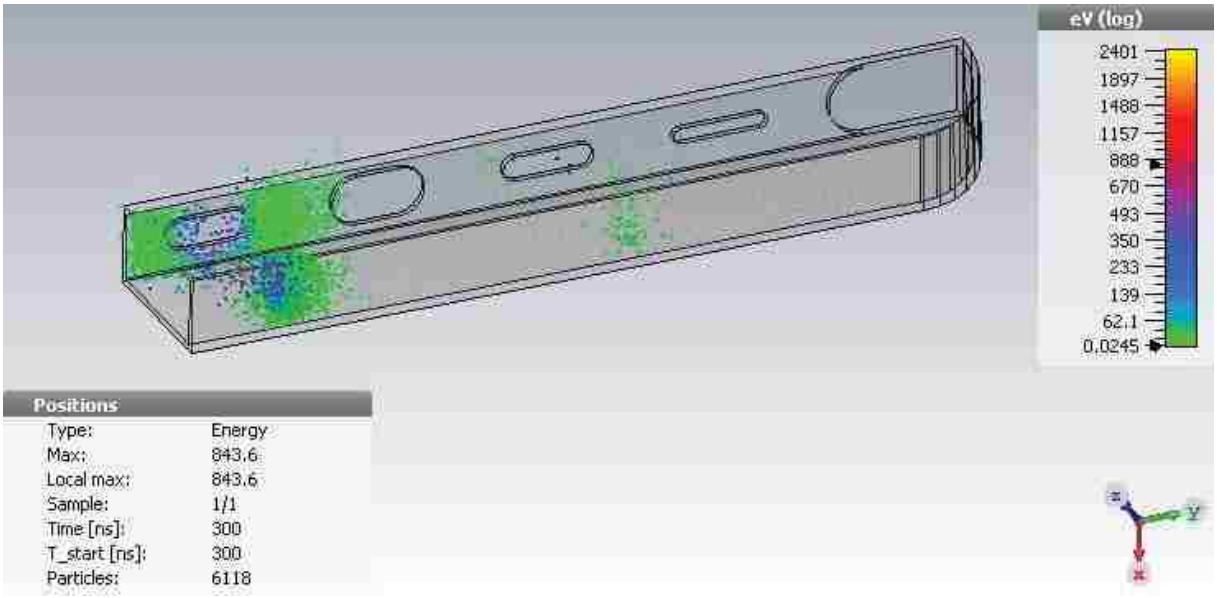


(b) Top view

Figure 4.16: Electron distribution inside the S-band longitudinal slotted waveguide antenna excited by 2.35MW. a) side view, b) 3D view.

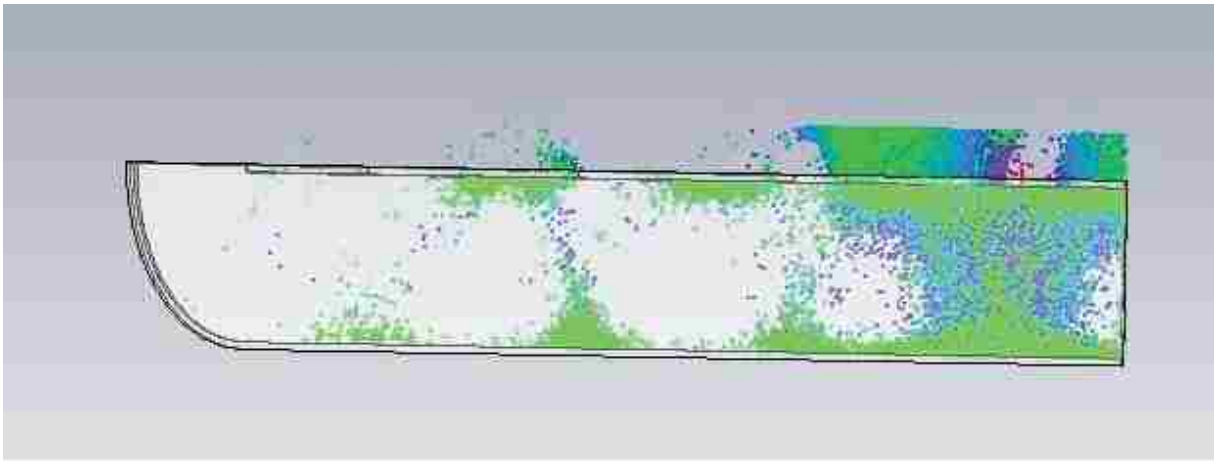

(a) Side view

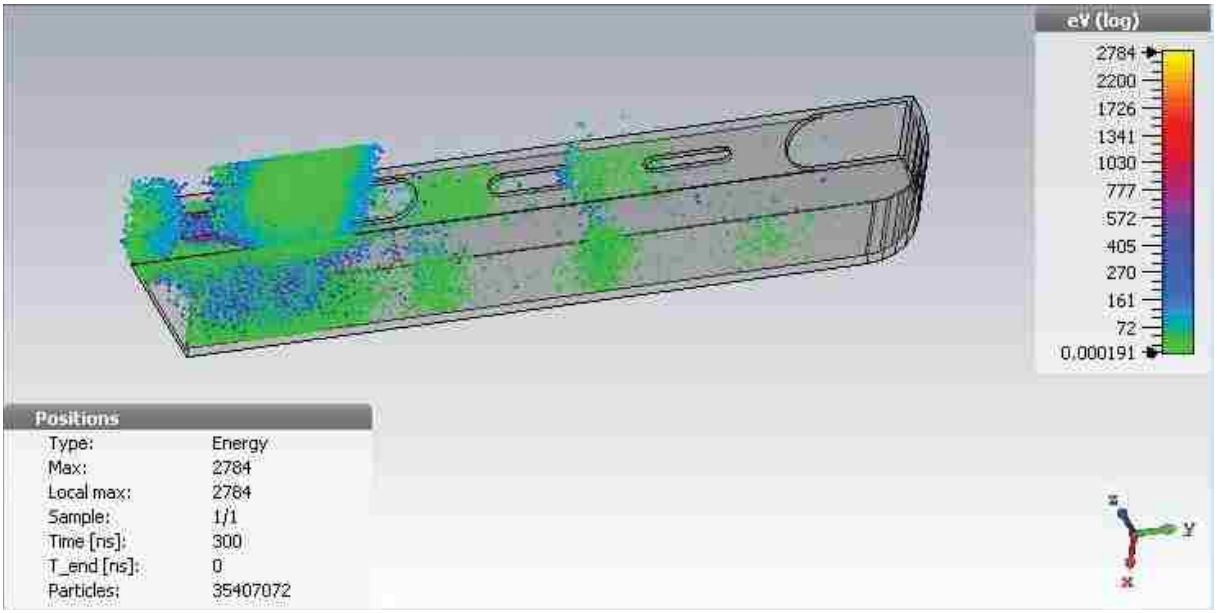


(b) Top view

Figure 4.17: Electron distribution inside the S-band longitudinal slotted waveguide antenna excited by 2.54MW. a) side view, b) 3D view.

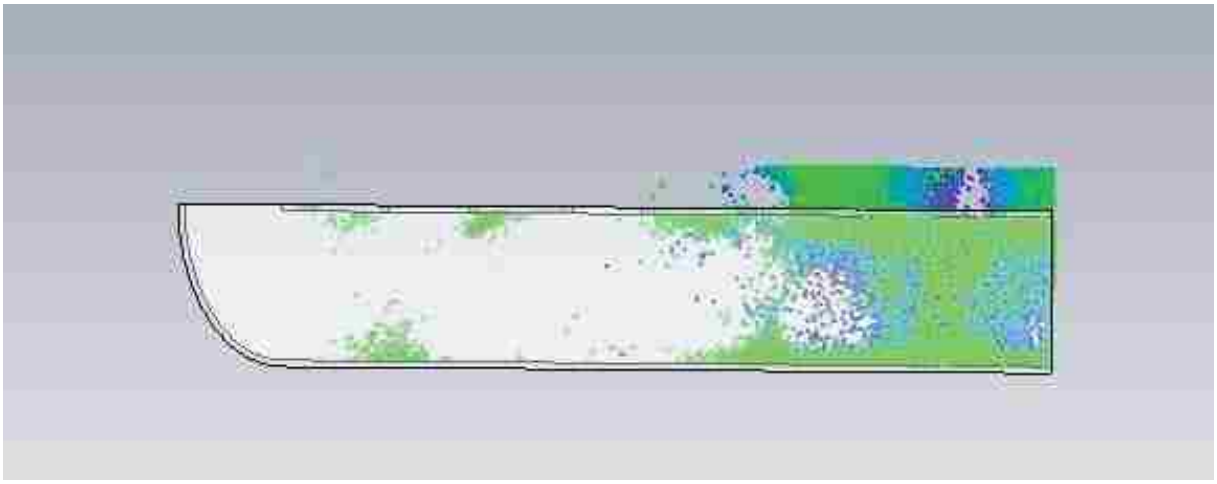

(a) Side view

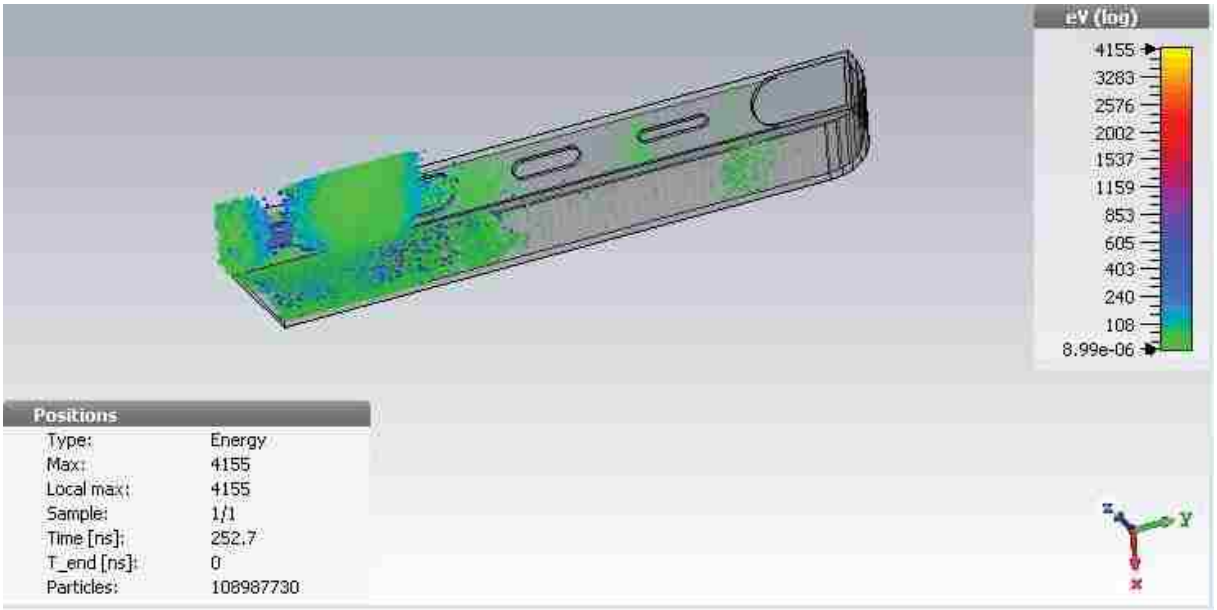


(b) Top view

Figure 4.18: Electron distribution inside the S-band longitudinal slotted waveguide antenna excited by 2.75MW. a) side view, b) 3D view.

## 4.2 Power handling capability estimation of slotted waveguide antenna for HPM applications

### 4.2.1 Power handling capability of the S-band narrow-wall longitudinal slotted waveguide antenna

For the S-band longitudinal slotted waveguide antenna to be operating in Albuquerque, New Mexico, USA, driven by a commercial S-band magnetron of output power ranging from 200kw up to 1MW with a pulse duration of 500ns, the maximum input power without causing multipaction inside the antenna is around 800kW, and the maximum input power without causing multipaction breakdown (saturated multipcation) inside the antenna is around 2.35MW. The former threshold is verified by the experiment during the single pulse field measurements, which showed no sign of breakdown. The latter threshold is yet to be verified as it actually exceeds the maximum input power threshold without causing air-breakdown outside the antenna (1.8MW). If current set-up of single pulse field measurements is to be used to test whether such input power of 2.35MW would cause multipaction breakdown during the time frame of 500ns, the receiving DDot sensor wouldnt be able to get any useful data, as the input power exceeds 1.8MW, and likely causes breakdown near the antenna, disrupting antenna radiation.

Thus we conclude that the S-band longitudinal slotted waveguide antenna is projected to withstand 1.8MW of input power, at the operating frequency of 3.17GHz, at Albuquerque, NM, USA.

### 4.2.2 Power handling capability estimation of slotted waveguide antenna for high-power-microwave applications

So, for any given slotted waveguide antenna designed for high-power-microwave applications, the maximum input power allowed is determined mainly by two breakdown mechanisms: 1. air breakdown (outside the antenna), 2. multipaction breakdown (inside the antenna). The former is determined mainly by the location of the antenna operation and the dielectricsubstrate used to fill/seal the slotted waveguide antennas. It can usually be predicted regardless of the high-power-microwave source used. The latter mechanism, however, is highly dependent on the relativistic high-power-microwave source, i.e. peak power, pulse duration, etc.

Thus, therere three thresholds to be considered during the power handling capability estimation: a) maximum input power without causing air-breakdown outside the antenna (shown in Figure 4.19a), b) maximum input power without causing multipaction inside the antenna (shown in Figure 4.19b), c) maximum input power without reaching multipaction saturation/breakdown inside the antenna (shown in Figure 4.19b). Estimation towards thresholds a an b can be done independently while estimation towards threshold c has to be conducted by taking the specific of the relativistic high-power-microwave source into account.

Following the procedures demonstrated in previous sections, the three input power thresholds can be obtained for any given slotted waveguide antenna designed for high-power-microwave applications. And it is known that the antenna can operate if the input power level is below the minimum of threshold a (maximum input power without causing air-breakdown) and threshold b (maximum input power without

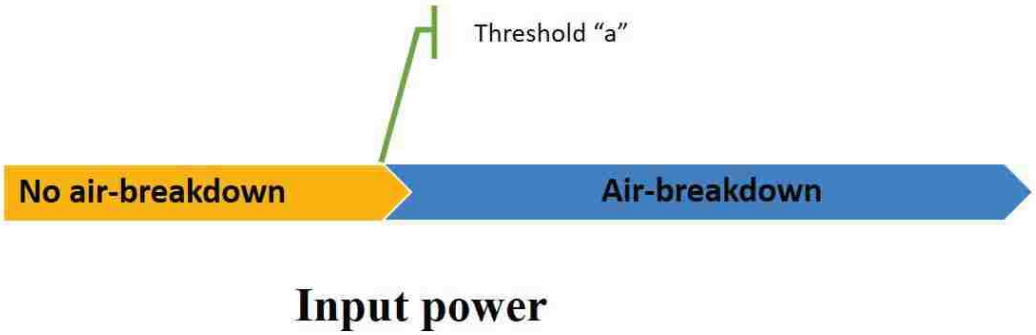


(a) Air breakdown

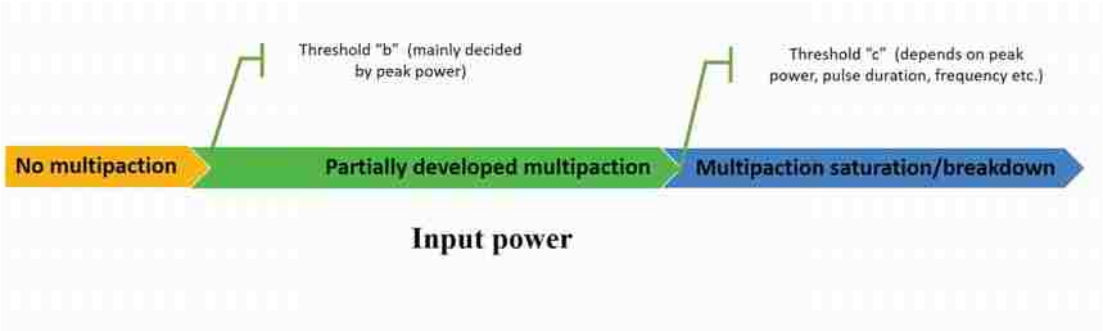


(b) Multipaction breakdown

Figure 4.19: High power microwave antenna breakdown mechanisms

causing multipaction), and that the antenna cannot operate if the input power level is above the minimum of threshold a and threshold c (maximum input power without reaching multipaction saturation/breakdown).

Further research needs to be done on whether a partially developed multipaction can affect the operation of the slotted waveguide antennas designed for high power microwave applications.

# Chapter 5

# Experiment results

## 5.1 Small scale measurements on the narrow-wall complementary-split-ring slotted waveguide antenna

Figure 5.1 shows the S-band narrow-wall complementary-split-ring slotted waveguide antenna aligned with the S-band narrow-wall longitudinal slotted waveguide antenna.

The experiment was conducted at 3.1689GHz and the feed guide used is a standard S-band WR-284 waveguide. The manufacturing of the complementary-split-ring slots on a metal plate is more difficult than that of the standard rectangular waveguide of circular slots. The antenna dimension tolerance is extremely small since a small change in CSRs dimensions can have an impact on the final EM performance of the antenna. Waterjet Cutting [82] was used to create the CSR slots on an

Figure 5.1: S-band narrow-wall complementary-split-ring slotted waveguide antenna aligned with the S-band narrow-wall longitudinal slotted waveguide antenna.

aluminum plate.

(a) aluminum plate as one the narrow-wall of the waveguide

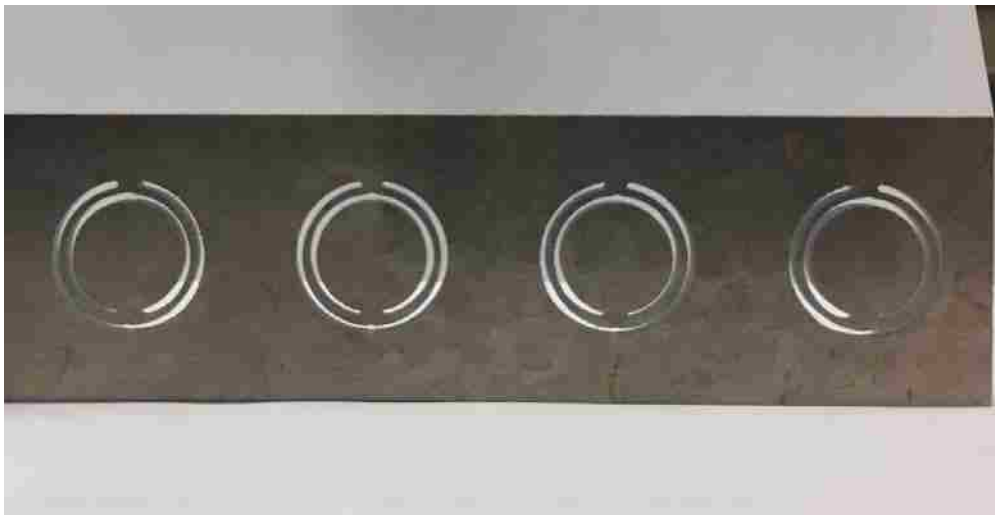

(b) Complementary-split-ring slots cut by Waterjet Cut Inc.

Figure 5.2: Aluminum plate with complementary-split-ring slots

Figure 5.2 shows the aluminum plate with the complementary split ring slots. Figure 5.3 shows the plates fabricated to be the walls of the waveguide. The final product was achieved by welding these four aluminum plates together as shown in Figure 5.4. A copper tape was used to seal the arch at the end of the waveguide. The skin depth of copper at the operating frequency of 3.17GHz is $3.67 * 10^{-7}m$. The thickness of the copper tape is $6 * 10^{-5}m$, which is more than 10 times the skin depth of copper at the operating frequency. Thus we consider the copper tape thick

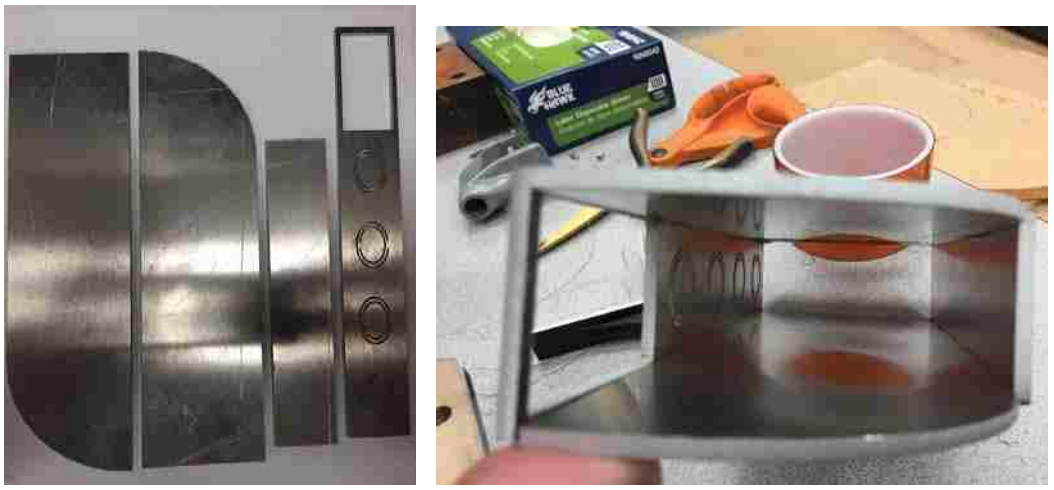

(a) (b)

Figure 5.3: (a)aluminum plates, (b) aluminum plates welded together

enough to act like a bended waveguide guide wall.

Figure 5.5 shows the experimental set-up used to measure the reflection coefficients of the S-band narrow-wall longitudinal-slot array shown in Figure 5.1. The antenna was connected to waveguide-to-SMA adapter, and then connected to a vector network analyzer, HP 83650A.

The absorber in Figure 5.5 is placed in front of the narrow-wall longitudinal-slot array so that all the radiated power will be absorbed instead of affecting the antenna itself. We set the frequency sweep range to be from 2.8 GHz to 3.4 GHz, and the sampling number is 200.

Figure 5.6 shows the result obtained from the network analyzer compared to the HFSS simulation results. The magnitude of S11 for the narrow-wall complementary-split-ring slotted waveguide antenna at the resonant frequency of 3.175GHz is approximately -40dB according to the experiment, while the magnitude of S11 for

Figure 5.4: S-band narrow-wall complementary-split-ring slotted waveguide antenna.

the narrow-wall complementary-split-ring slotted waveguide antenna at the resonant frequency of 3.1689GHz is approximately -30dB according to the simulation. Such

Figure 5.5: S parameter measurement set-up for the S-band narrow-wall complementary-split-ring slotted waveguide antenna.

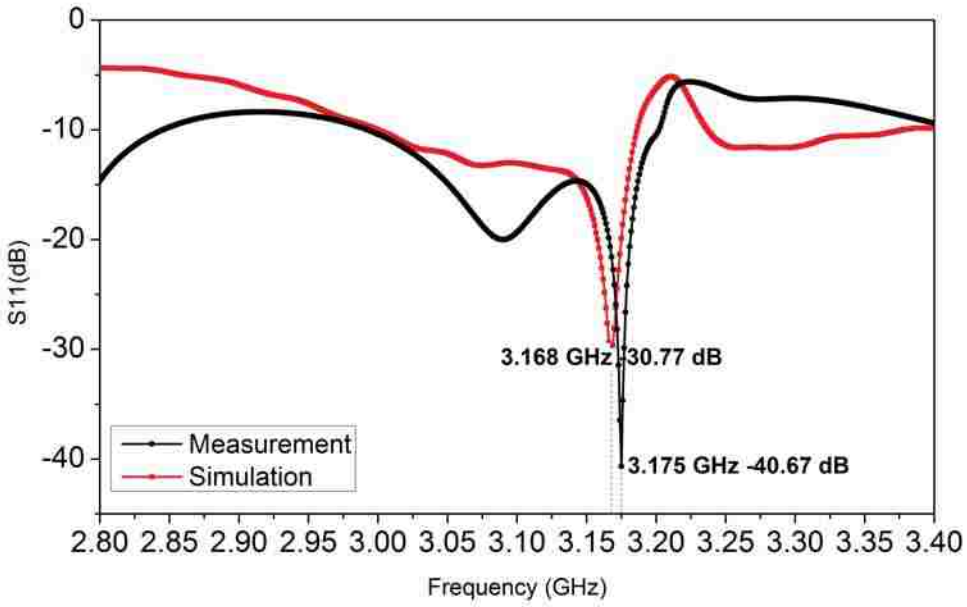


Figure 5.6: S parameter measurement result compared to simulation.

frequency shift is likely caused by the error introduced during fabrication of the aluminum plates and the assembly through welding. Good agreement between the theoretical analysis and experiments of the return loss of the antenna shows that the narrow-wall complementary-split-ring slotted waveguide antenna is well matched and suitable for high power microwave applications.

Figure 5.7 shows the experimental set up used to measure the radiation patterns of the S-band narrow-wall complementary-split-ring slotted waveguide antenna. The turn table shown in the figure is an ETS Lindgreen Model 2005 Azimuth Positioner. The S-band narrow-wall complementary-split-ring slotted waveguide antenna was placed on the turn table, aligned with the center of the standard horn. Both the S-band narrow-wall complementary-split-ring slotted waveguide antenna and the standard horn were connected to Agilent PNA-X N5247A. The S-band narrow-wall

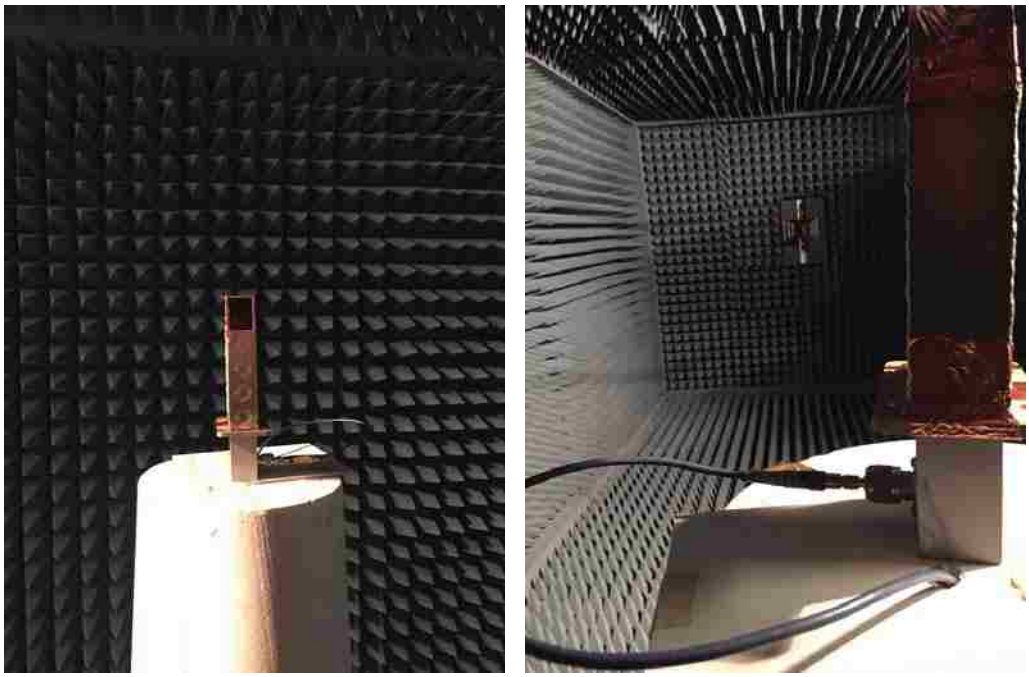

(a) (b)

Figure 5.7: Radiation pattern measurement set-up.

complementary-split-ring slotted waveguide antenna and the standard horn were separated by 4.2m, which puts the standard horn in the far-field region of the S-band narrow-wall complementary-split-ring slotted waveguide antenna.

By changing the orientation of the S-band narrow-wall complementary-split-ring slotted waveguide antenna and the standard horn, the co-polarized and cross-polarized components of both the H-plane and E-plane of the S-band narrow-wall complementary-split-ring slotted waveguide antenna were measured. The built-in software of the antenna gain measurement controls the speed and increment of the rotation of the turn table. The radiation pattern measurement was conducted at the measured resonant frequency, 3.175GHz.

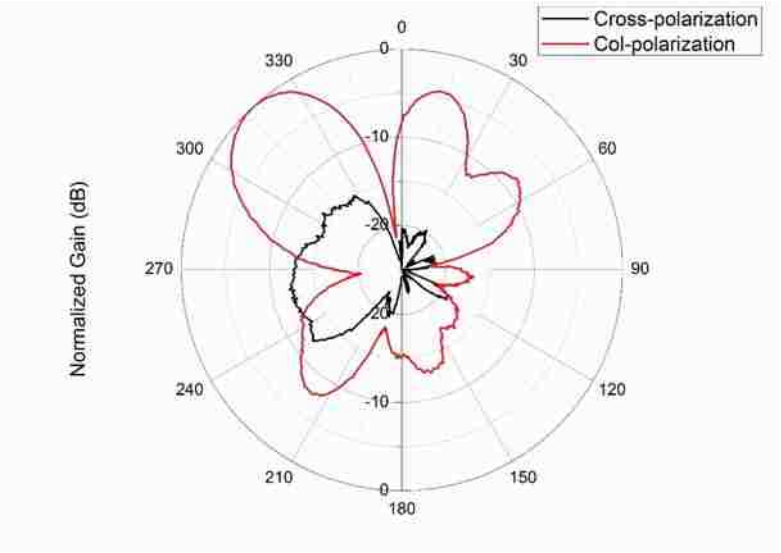


Figure 5.8: Measured col-polarization & cross polarization of the H-plane of the S-band narrow-wall complementary-split-ring slotted waveguide antenna.

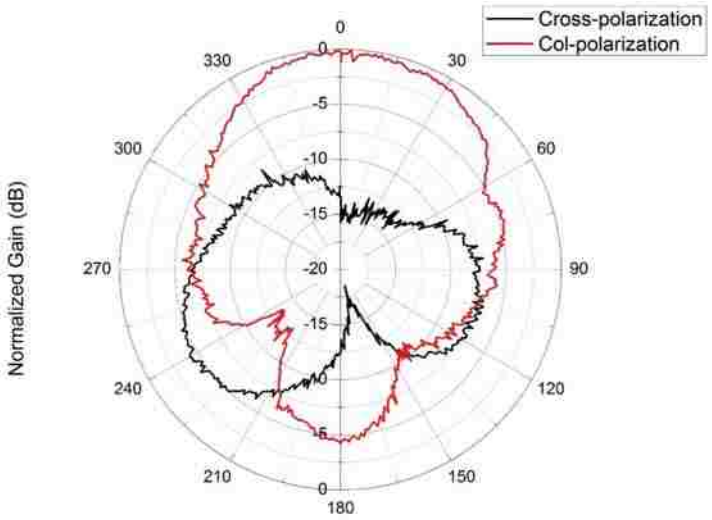


Figure 5.9: Measured col-polarization & cross polarization of the E-plane of the S-band narrow-wall complementary-split-ring slotted waveguide antenna.

The measured co-polar and cross-polar componets of both the H-plane and E-plane of the antenna are shown in Figure 5.8 and 5.9.

It can be easily concluded that the S-band narrow-wall complementary-split-ring slotted waveguide antenna provides a linear polarization within the main beam of the antenna.

Figure 5.10 and 5.11 compare the theoretical and experimental radiation patterns of the S-band narrow-wall complementary-split-ring slotted waveguide antenna.

Good agreement is shown between measured and simulated radiation patterns for the S-band narrow-wall complementary-split-ring slotted waveguide antenna. The

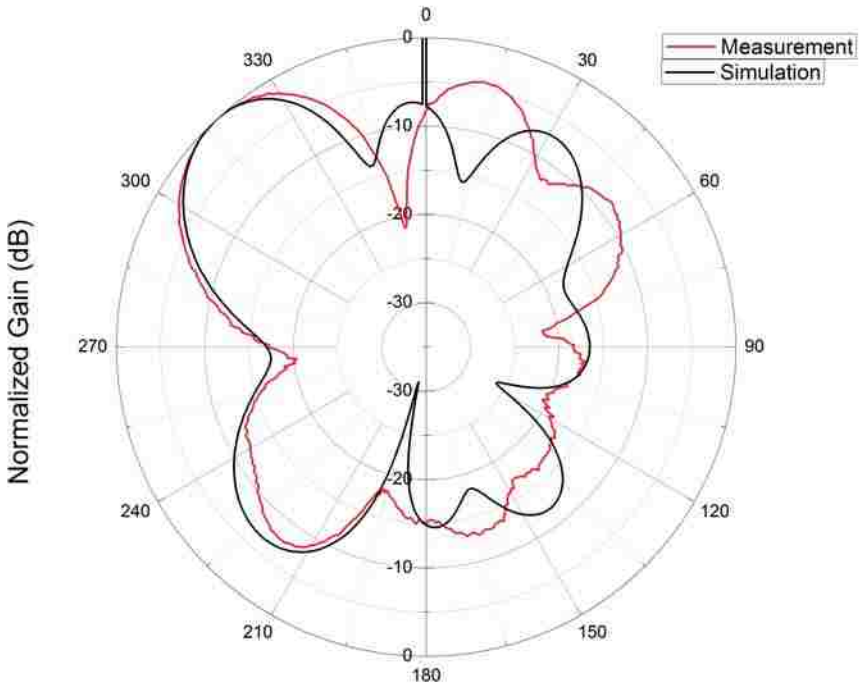


Figure 5.10: Measured and simulated E-plane radiation pattern of the H-plane of the S-band narrow-wall complementary-split-ring slotted waveguide antenna.

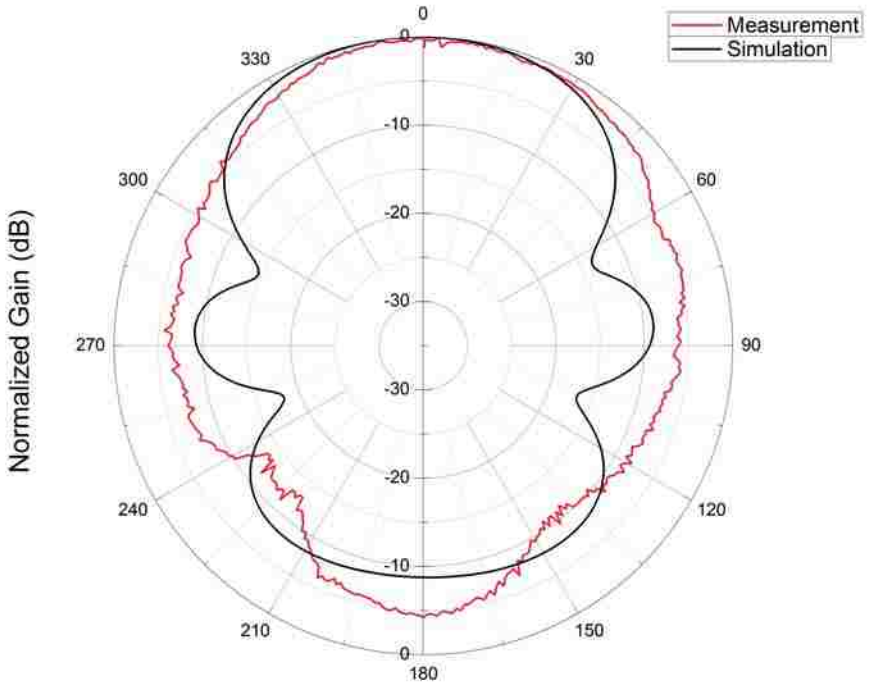


Figure 5.11: Measured and simulated E-plane radiation pattern of the S-band narrow-wall complementary-split-ring slotted waveguide antenna.

slight differences between simulation and measurement results are likely caused by manufacturing as well as cable effect during radiation pattern measurement.

Based on these results, we conclude that the proposed CSR-SWA has very low return loss, which makes it suitable for HPM systems, especially at MW and GW levels. The measured radiation patterns show good agreement with the simulated ones, which proves that CSR slots are good radiating elements for slotted waveguide antenna designs. The proposed CSR-SWA also shows significant size reduction, way beyond the limitations of the conventional half-wavelength SWA designs.

## 5.2 Fast prototyping of the high-power-microwave CSR slotted waveguide antenna

CSR-SWA designs depend on highly accurate electromagnetic simulations that take geometric details into full account. Conventional antenna manufacturing approaches such as direct machining and platelet technology lack the ability to precisely translate the electromagnetic simulation model into its physical metallization. To rapidly prototype complex 3D antenna structures in a cost-effective way, we propose an approach based on stereolithography or 3D printing technology. It has been shown that 3D printing is capable of providing manufacturing precision for CSR-SWAs that makes fast prototyping of CSR-SWAs for HPM applications possible.

Besides providing manufacturing precision, the idea of fabricating complex antennas using plastic and then coating them with a conductive material can also benefit from the low cost of 3D printing technology and its lightweight. The much-reduced dimension of the CSR-SWA compared to the longitudinal slotted waveguide antenna makes the antenna possible to be fabricated with most commercially available 3D printers. Figure 5.12 shows one of the CSR-SWAs fabricated using a commercial 3D printer, next to the aluminum CSR-SWA.

The CSR-SWA shown in Figure 5.12 was printed using an uPRINT SE 3D printer, which prints with ABSplus and with an accuracy of 100 microns. The total time required to print the complementary-split-ring slotted waveguide antenna was approximately 14 hours.

First, metallic spray paint was applied to the 3D printed CSR-SWA to create a

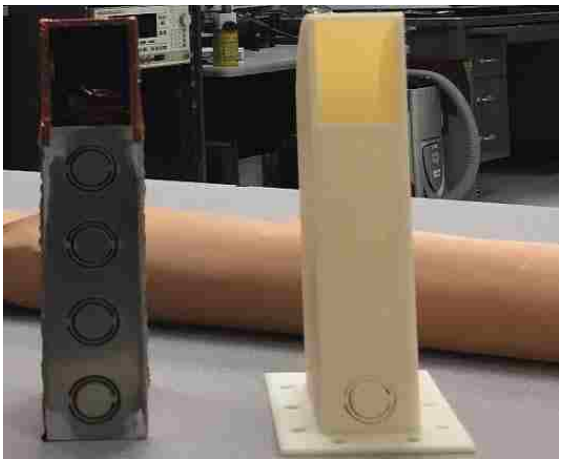

Figure 5.12: 3D printed CSR-SWA (on the right) and aluminum CSR-SWA. Antenna one the left is the metallic version.

metallic layer thick enough so that the antenna can radiate. Also, it was an attempt to further facilitate the fabrication process as the spray painting can be done quickly and ready to test after the paint dries in an hour.

The MG chemical 843 [83] was used as the metallic spray paint. The MG chemical 843 is a high conductive coating designed to reduce electromagnetic or radio frequency interference (EMI/RFI). According to the manufacturer, it provides a low surface resistivity of 0.21 S/square (1.0 mil), which is equal to a bulk conductivity of 1.87*105 S/m.

Since the metallic spray is manually applied, control of the metallization thickness uniformity and surface roughness is very critical. As expected, a higher surface resistance degrades the gain of the CSR-SWA.

Figure 5.13 shows the schematic of the antenna that was metallized. An average thickness of 0.3mm of the conductive spray coating was applied to the wall, which is much greater than 0.0065mm, the skin depth of the MG chemical 843 conductive

coating at the operating frequency of 3.17GHz. The 3D printed CSR-SWA with conductive coating was modeled in HFSS, as shown in Figure 5.13. A modified model was 3D printed and metallically sprayed, as shown in Figure 5.14.

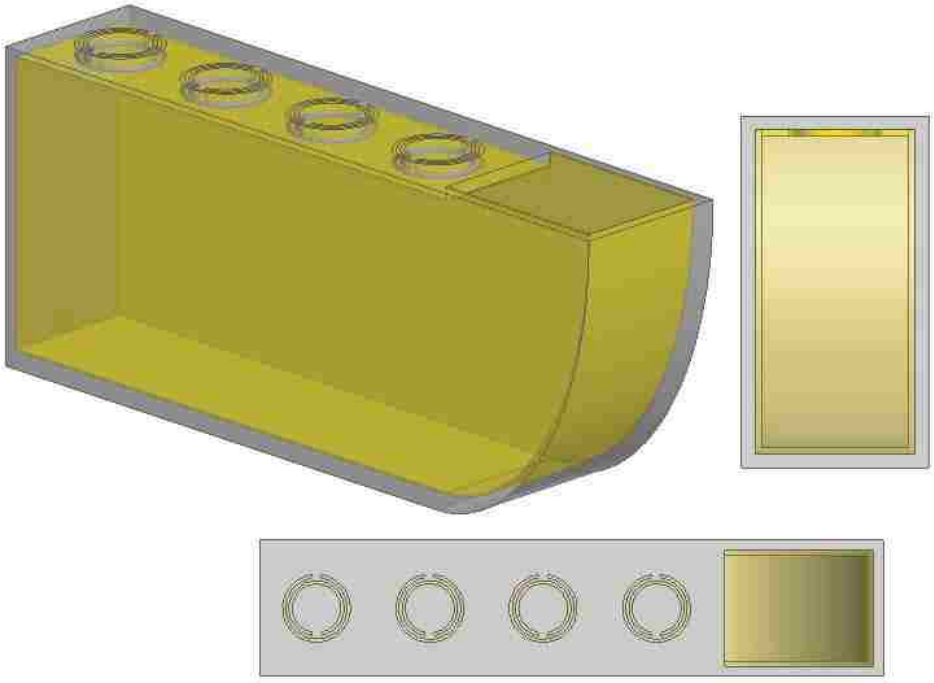

Figure 5.13: Schematic of 3D printed CSR-SWA with conductive coatings.

The measured and simulated S11 values are shown in Figure 5.15. Figures 5.16 and 5.17 present the comparison of the radiation patterns of the modified 3D printed CSR-SWA with conductive coating and the metal CSR-SWA. Despite the manually applied conductive spray, the ABS plastic CSR-SWA coated with metallic paint shows similar radiation characteristics compared to the metal CSR-SWA.

Overall, the radiation patterns of the 3D printed array are close to the ones from the equivalent metallic array. However, the lossy metallic spray paint applied created

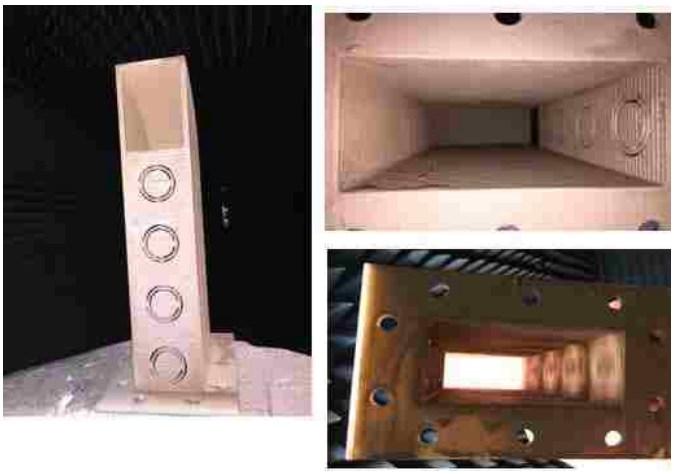

Figure 5.14: A 3D printed CSR-SWA applied with MG chemical 843 conductive coating.

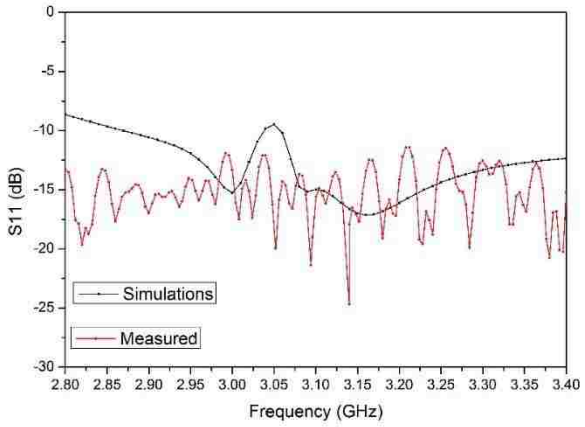


Figure 5.15: S11 of 3D printed modified CSR-SWA with conductive coating.

a higher surface resistance, which degraded the gain of the antenna. Thus we started looking into electro-plating as an alternative to create the desired metallic coating layer.

The first plating step is room temperature electroless nickel plating. This step

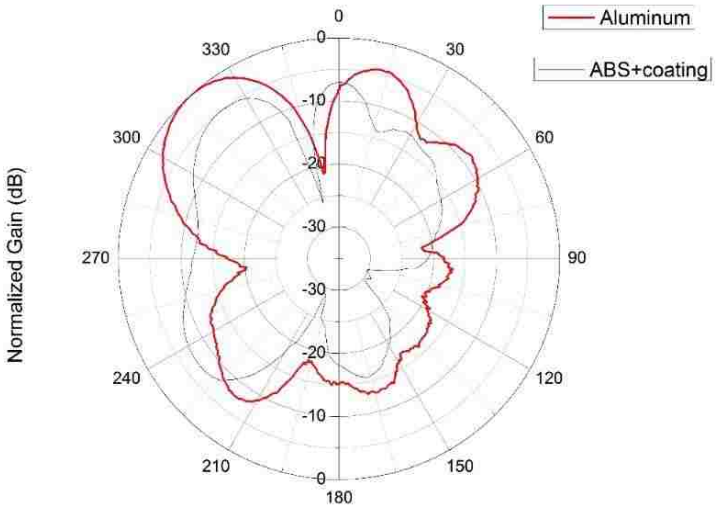


Figure 5.16: H-plane radiation pattern of 3D printed modified CSR-SWA with conductive coating.

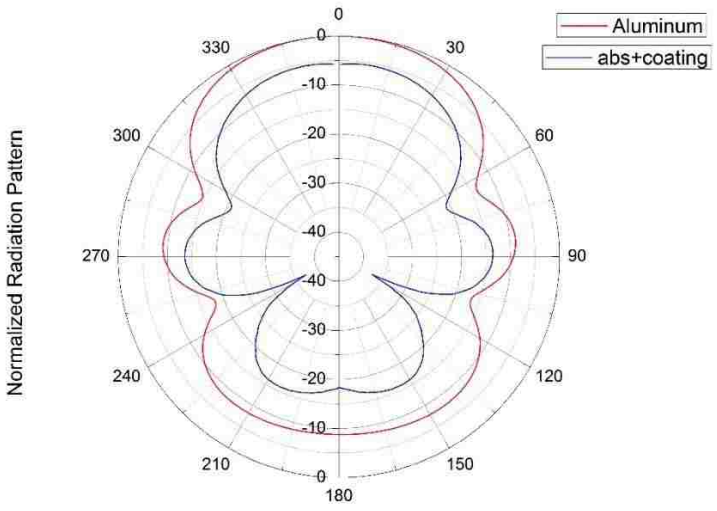


Figure 5.17: E-plane radiation pattern of 3D printed modified CSR-SWA with conductive coating.

provides the conductive layer necessary to enable electroplating. Electroless plating followed by electro-plating has proven high performance. From an RF point of view, a plastic part plated with multiple skin depths of metal operates identically to a solid metal part. Measured 3D printed arrays consistently have gain that is very similar to both metallic arrays of identical design and HFSS simulation.

The antenna is plated with about 2 mils (50.8microns) of copper externally, and inside there can be regions where the thickness is reduced to $10-20\%$ of this thickness. That means theres a minimum of 5.08 microns of copper everywhere. At 3.1689 GHz, thats 4.37 skin depths of copper which is adequate for the metal plated structure to function essentially the same as a solid copper structure. Current density decreases exponentially as distance divided by skin depth, so at 3.1689GHz, in the region of the antenna with the thinnest copper, thats $e^{-4.37} = 0.01$.

The metal plating thickness is thin enough to be disregarded mechanically, i.e. the additional thickness does not affect the mechanical aspects of the design. Howeverfor conventional slotted waveguide antenna design, the additional thickness of 5-50 microns can affect the dimensions of the complementary-split-ring slots and the RF performance of such slots. Such additional thickness has to be included during the design of the CSR-SWA before it gets 3D printed. The plating process has significant flexibility to meet RF performance requirements. Meanwhile, the plastic structure is relatively inexpensive, and significantly lighter than a solid metal structure.

The 3D printed antennas are washed in fresh alcohol and cured with UV light. The ceramic filled stereolithography resin is chosen for its stability and stiffness. The resin is very opaque to UV light, so it is difficult to post cure the resin with a UV light oven. These resins do thermally cure at elevated temperature or in longer

Figure 5.18: ABS printed CSR-SWA next to the Bluestone printed CSR-SWA.

time at room temperature. Parts that are properly cleaned and cured will result in more uniform deposition of nickel and subsequent copper over all surfaces. In addition to SLA, the multijet 3d printing process can also produce precise objects, but the support material used cannot be removed to the extent required to enable uniform nickel and copper plating. The antenna presented here used SLA 3D printing followed by thorough cleaning and curing. The resins used for SLA 3D printing of the slotted waveguide antenna presented here is Accura Bluestone [84]. Bluestone is a rigid stable engineered nano composite for high stiffness parts. It provides the highest stiffness available, heat and abrasion resistance, and chemical resistance. Bluestone can be used for printing on 3D stereolithography printers like ProX 800 and ProX 950. The slotted waveguide antenna presented here was printed by 3D Proven System in Albuquerque NM. Figure 5.18 shows the ABS printed CSR-SWA next to the Bluestone printed CSR-SWA.

The relatively low Coefficient of Thermal Expansion of these resins also enhances the metal plating success. Plating of the slotted waveguide antenna was performed by RepliForm inc in Baltimore MD [85]. Figure 5.19 shows the copper plated CSR-SWA based on Bluestone.

Figure 5.20 presents the Agilent PNA-X N5247A used to measure the return loss of the copper plated CSR-SWA printed on Bluestone. The results are shown in Figure 5.21.

Figure 5.20 presents the Agilent PNA-X N5247A used to measure the return loss of the copper plated CSR-SWA printed on Bluestone. The results are shown in


Figure 5.19: Bluestone printed CSR-SWA plated with copper by RepliForm Inc.

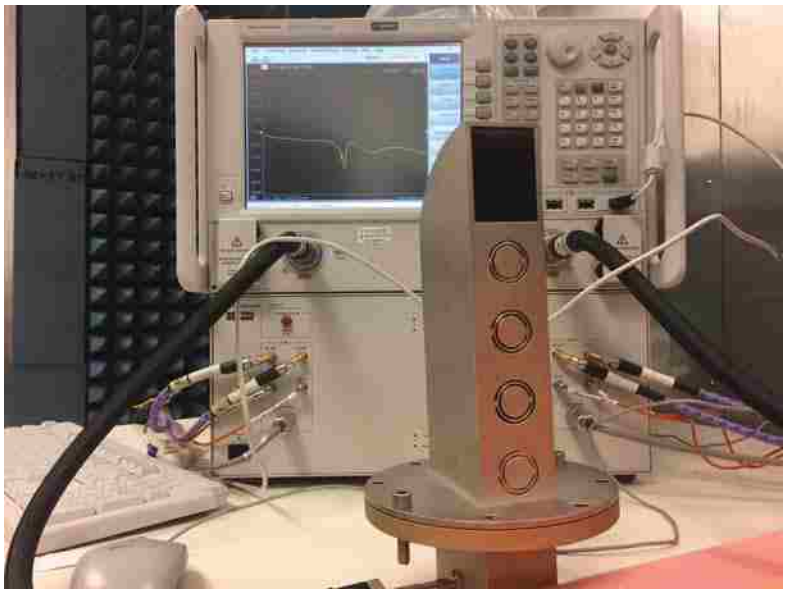

Figure 5.20: S11 measurement set-up for the copper plated CSR-SWA printed on Bluestone

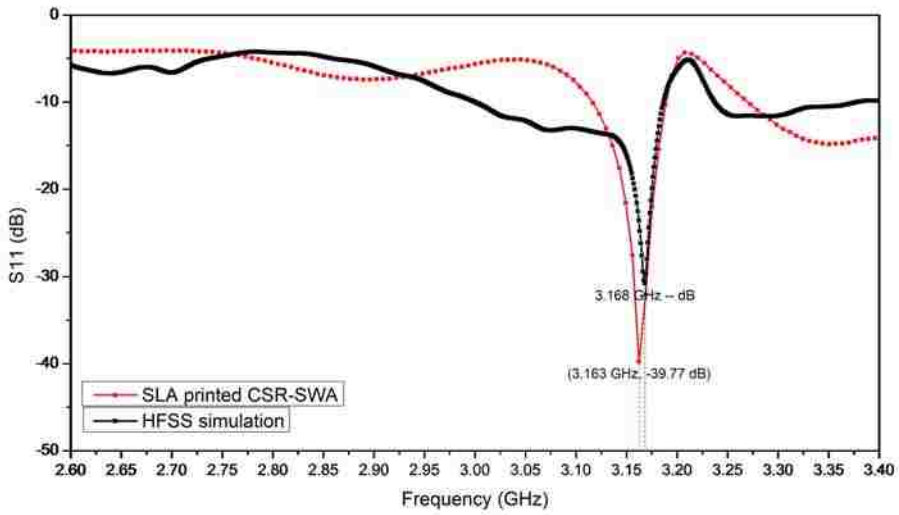


Figure 5.21: S11 measurement set-up for the copper plated CSR-SWA printed on Bluestone

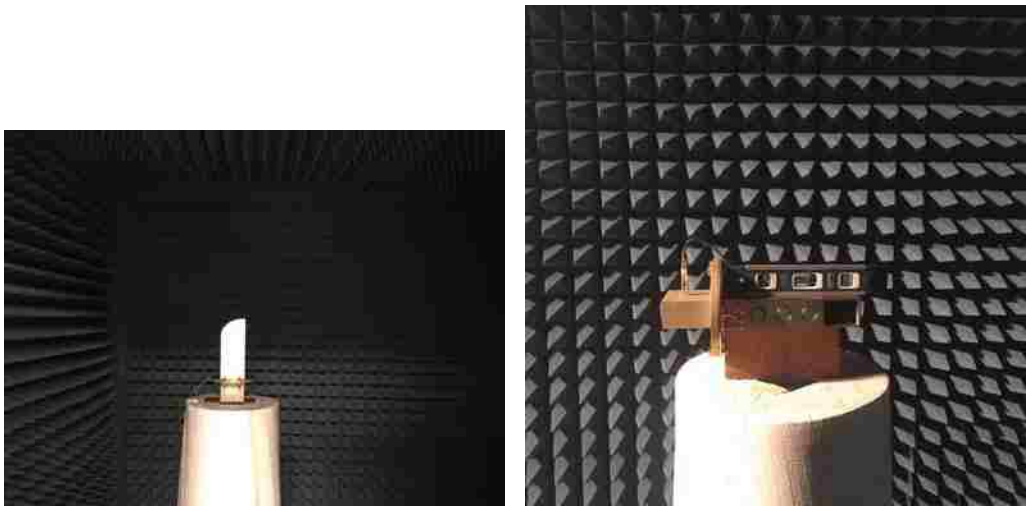

(a) (b)

Figure 5.22: Radiation pattern measurement set-up.

Figure 5.21.

Similar to the measurements performed before, Figure 5.22 shows the test set-up for the radiation patterns of the copper plated CSR-SWA printed on Bluestone.

Figure 5.23 and 5.24 show a comparison of the simulated radiation patterns and the measured alumnum CSR-SWA mentioned before. The alumnium CSR-SWA has a measured peak gain of 8.9577 dB while the copper plated CSR-SWA printed on Bluestone has a measured peak gain of 7.3969 dB. The drop in peak gain of the antenna was expected due to addtional loss in the materials used. These losses were also predicted in our simulation results of the copper plated CSR-SWA printed on Bluestone. The measured radiation patterns show a good agreement in radiation characteristics such as, beamwidth, boresight angle, side lobe level, polarization etc.

These results suggest that no significant degradation of antenna performance due to surface roughness or dimensional tolerances of SLA 3D printed and plated

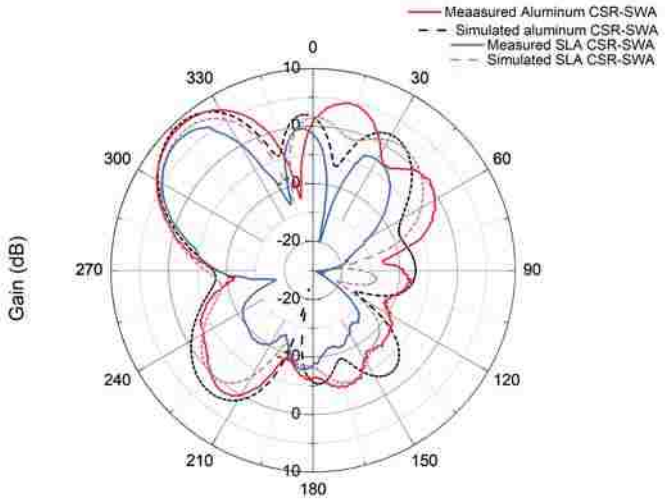


Figure 5.23: H-plane radiation pattern of the aluminum CSR-SWA and the copper plated CSR-SWA printed on Bluestone.

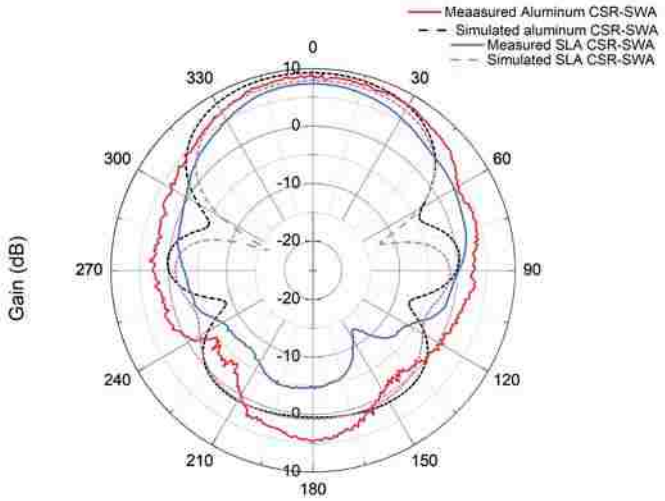


Figure 5.24: E-plane radiation pattern of the aluminum CSR-SWA and the copper plated CSR-SWA printed on Bluestone.

antennas based on experiments performed at 3.17 GHz. Print resolution using SLA is on the order of 45 microns, so for S-band operation, no degradation of performance due to 3D printing resolution limitations should be expected.

# Chapter 6

# Conclusion and Future Work

In this dissertation work, we investigated the structure of complementary-split-ring slots as a radiating elements for size reduction of the conventional half-wavelength slot structure. Combining the advantage of the compact size of split ring slots and the higher power handling capability of narrow-wall apertures, a narrow-wall rugged complementary-split-ring (CSR) slotted waveguide antenna (SWA) is proposed for high power microwave application.

Applying microwave network analysis and full-wave analysis tool (HFSS&CST), an array of complementary-split-ring slots on the narrow-wall of an rectangular waveguide is designed to form an uniform array with minimal power reflected back to the input port. The antenna is simulated, manufactured and tested. The results show that the proposed CSR-SWA has a peak measured gain of 8.9577dB at 3.17GHz and return loss as low as -40dB. It is well suited for high power microwave applications.

Using 3D printing technology and electro-plating techniques, the CSR-SWA is able to be easily manufactured. The test results of the 3D printed CSR-SWAs show

a similar peak gain and radiation patterns compared to the aluminum CSR-SWA model. It provides a new method for fast-prototyping microwave passive devices for high-power-microwave applications, especially for the devices using meta-material like structures or meta-materials that have complicated geometric structures. It is not only cost effective but also extremely light weighted, which can be a key advantage for HPM antenna designs like lens antennas.

In this work, a new procedure is proposed to estimate the power handling capability of an high-power-microwave antenna during its design phase. Taking both air-breakdown and multipaction breakdown into consideration, the proposed procedure suits well for HPM antennas operating both under vacuum condition and under air environment. The estimated input power threshold for the S-band longitudinal slotted waveguide antenna can function as a proper guideline for the high-power-microwave test performed.

Future work should focus in the following areas: 1, developing compact high-power-microwave phase-shifters for improving the beam steering mechanism of the narrow-wall longitudinal-slot array antennas. 2, experiment with various 3D printing technology to develop some understanding of various material properties under high-power-microwave pulses. 3, studying the physics of multipaction within a leaky-wave structure.

# References


[1] W. A. Radasky, C. E. Baum, and M. W. Wik. "Introduction to the special issue on high-power electromagnetics (HPEM) and intentional electromagnetic interference (IEMI)". *IEEE Transactions on Electromagnetic Compatibility*, Vol. 46(3):pp. 314–321, Aug 2004.

[2] D. V. Giri and F. M. Tesche. "Classification of intentional electromagnetic environments (IEME)". *IEEE Transactions on Electromagnetic Compatibility*, Vol. 46(3):pp. 322–328, Aug 2004.

[3] D.V. Giri. *High-Power Electromagnetic Radiators Nonlethal Weapons and Other Applications*, chapter Ch. 2, pages 23–28. "Example scenarios for nonlethal systems". Harvard University Press, Cambridge, MA, 2004.

[4] M. R. Lambrecht, K. L. Cartwright, C. E. Baum, and E. Schamiloglu. "Electromagnetic modeling of hot-wire detonators". *IEEE Transactions on Microwave Theory and Techniques*, Vol. 57(7):pp. 1707–1713, July 2009.

[5] Janes Benford, John Swegle, and Edl Schamiloglu. *High Power Microwaves, Third Edition*. CRC Press, Boca Raton, FL, 2015.

[6] C.D.Taylor and D.V.Giri. "Waveguide/antenna design considerations for high-power microwaves". *High-Power Microwave Systems and Effects*, ch.2:pp.23–59, 1994.

[7] W. D. Prather, C. E. Baum, J. M. Lehr, J. P. O'Loughlin, S. Tyo, J. S. H. Schoenberg, R. J. Torres, T. C. Tran, D. W. Scholfield, J. Gaudet, and J. W. Burger. "Ultra-wideband source and antenna research". *IEEE Transactions on Plasma Science*, Vol. 28(5):pp. 1624–1630, 2000.

[8] E. G. Farr, L. H. Bowen, C. E. Baum, and W. D. Prather. "The folded horn antenna". *IEEE Transactions on Antennas and Propagation*, Vol. 55(11):pp. 3341–3344, Nov 2007.

[9] N.R.Devarapalli. *"Rectangular waveguide narrow-wall longitudinal-aperture antenna arrays for high power applications"*. Doctor dissertation, University of New Mexico, Albuquerque, New Mexico, August 2009.

[10] J. Miletta N. Tesny L. Dilks C. Brown W. Coburn, M. Litz and B. King. "A slotted-waveguide array for high-power microwave transmission". Army Research Laboratory, Jan 2001.

[11] J. E. Lawrance, C. G. Christodoulou, and M. R. Taha. "A high-power microwave zoom antenna with metal-plate lenses". *IEEE Transactions on Antennas and Propagation*, Vol. 63(8):pp. 3380–3389, Aug 2015.

[12] X. Li, Q. Liu, X. Wu, L. Zhao, J. Zhang, and Z. Zhang. "A gw level high-power radial line helical array antenna". *IEEE Transactions on Antennas and Propagation*, Vol. 56(9):pp. 2943–2948, Sept 2008.

[13] X. Li, Q. Liu, J. Zhang, and L. Zhao. 16-element single-layer rectangular radial line helical array antenna for high-power applications. *IEEE Antennas and Wireless Propagation Letters*, Vol. 9:pp. 708–711, 2010.

[14] J. Zhao, H. Li, and T. Li. "Design of a double square rings element for high-power x-band reflectarray antenna". In *2015 IEEE International Vacuum Electronics Conference (IVEC)*, pages 1–2, April 2015.

[15] C.E.Baum. "Sidewall waveguide slot antenna for high power". Sensor and Simulation Notes, Note 503, August 2005.

[16] C.D.Taylor and D.V.Giri. "Canonical examples of hpm radiation systems". *High-Power Microwave Systems and Effects*, ch.3:pp.61–110, 1994.

[17] A.F. Stevensen. "Theory of slots in rectangular wave-guides". *Appl. Phys.*, Vol. 19:pp. 24–38, Jan 1948.

[18] H. Jasik, editor. *Antenna Engineering Handbook*. McGraw-Hill Companies,Incorporated, 1961.

[19] Pan. *"S band narrow-wall slotted waveguide antenna for high-power applications"*. Master thesis, University of New Mexico, Albuquerque, New Mexico, December 2012.

[20] Constantine A. Balanis. *Antenna Theory: Analysis and Design, 3rd Edition*. Wiley, 2005.

[21] R.E.Collin. *"Field Theory of Guided Waves"*. The Institute of Electrical and Electronics Engineers, Inc., New York, 1991.

[22] D.M. Pozar. *Microwave Engineering*. Wiley John & Sons, New York, 2005.

[23] K. J. Nicholson, W. S. T. Rowe, P. J. Callus, and K. Ghorbani. "Split-ring resonator loading for the slotted waveguide antenna stiffened structure. *IEEE Antennas and Wireless Propagation Letters*, 10:1524–1527, 2011.

[24] K. J. Nicholson, W. S. T. Rowe, P. J. Callus, and K. Ghorbani. "Small slot design for slotted waveguide antenna stiffened structure. *Electronics Letters*, 48(12):676 –677, June 2012.

[25] A. Daliri, W. S. T. Rowe, and K. Ghorbani. "Slotted waveguide antenna array using complimentary split ring resonator elements. In *2014 International Workshop on Antenna Technology: Small Antennas, Novel EM Structures and Materials, and Applications (iWAT)*, pages 344–347, March 2014.

[26] A. Daliri, W. S. T. Rowe, and K. Ghorbani. "Split-ring slot in the broad-wall of a rectangular waveguide. *IEEE Antennas and Wireless Propagation Letters*, Vol. 13:pp. 991–994, 2014.

[27] X. Pan and C. G. Christodoulou. "A compact s-band narrow-wall complementary-split-ring slotted waveguide antenna for high power applications". In *2015 IEEE International Symposium on Antennas and Propagation USNC/URSI National Radio Science Meeting*, pages 675–676, July 2015.

[28] L. Guo, W. Huang, C. Chang, J. Li, Y. Liu, and R. Meng. "Studies of a leaky-wave phased array antenna for high-power microwave applications. *IEEE Transactions on Plasma Science*, Vol. 44(10):pp. 2366–2375, Oct 2016.

[29] N.R. Devarapalli, C.G. Christodoulou C.E. Baum, and E. Schamiloglu. "A fan-beam radiator using waveguide's narrow wall for horizontal polarization and high power". *IEEE Transactions on Electromagnetic Compatibility*, Vol. 53(2):pp. 380–389, May 2011.

[30] O. Manoochehri, A. Darvazehban, M. A. Salari, A. Emadeddin, and D. Erricolo. "A parallel plate ultrawideband multibeam microwave lens antenna". *IEEE Transactions on Antennas and Propagation*, Vol. 66(9):pp. 4878–4883, Sept 2018.

[31] J. R. M. Vaughan. "Multipactor". *IEEE Transactions on Electron Devices*, Vol. 35(7):pp. 1172–1180, July 1988.

[32] Friedrich Paschen. "Ueber die zum funkenbergang in luft, wasserstoff und kohlensure bei verschiedenen drucken erforderliche potentialdifferenz". *Annalen der Physik*, Vol. 273(5):pp. 69–96.

[33] F. W. Peek. "Effect of altitude on the spark-over voltages of bushings, leads and insulators. *Transactions of the American Institute of Electrical Engineers*, Vol. XXXIII(2):pp. 1721–1730, June 1914.

[34] C. R. Garcia, R. C. Rumpf, H. H. Tsang, and J. H. Barton. "Effects of extreme surface roughness on 3d printed horn antenna". *Electronics Letters*, Vol. 49(12):pp. 734–736, June 2013.

[35] T. S. Bird and C. Granet. "Fabrication and space-qualifying a lightweight corrugated horn with low sidelobes for global-earth coverage". *IEEE Antennas and Propagation Magazine*, Vol. 50(1):pp. 80–86, Feb 2008.

[36] J. Czyewski, P. Burzyski, K. Gawe, and J. Meisner. "Rapid prototyping of electrically conductive components using 3D printing technology". *Journal of Materials Processing Technology*, Vol.209(12):pp. 5281–5285, July 2009.

[37] N. M. Jordan, G. B. Greening, S. C. Exelby, R. M. Gilgenbach, Y. Y. Lau, and B. W. Hoff. "Additively manufactured anodes in a relativistic planar magnetron". In *2016 IEEE International Vacuum Electronics Conference (IVEC)*, pages 1–2, April 2016.

[38] F. Capolino. *Theory and Phenomena of Metamaterials*. CRC Press:Taylor and Francis, Boca Raton, FL, USA, 2009.

[39] R. Marqués, F. Martín, and M. Sorolla. *Metamaterials with Negative Parameters: Theory, Design, and Microwave Applications*. Wiley Series in Microwave and Optical Engineering. Wiley, 2011.

[40] T. Roy, E. T. F. Rogers, and N. I. Zheludev. "Sub-wavelength focusing meta-lens". *Opt. Express*, Vol. 21:pp. 7577–7582, Mar 2013.

[41] M. Ghosh and S. Kar. "Metamaterial plane-slab focusing and sub-wavelength imagingthe concept, analysis and characterization'. In *2013 Science and Information Conference*, pages 670–674, Oct 2013.

[42] V. G. Veselago. "The electrodynamics of substances with simultaneously negative values of $\epsilon$ and $\mu$". *Soviet Physics Uspekhi*, Vol.10:pp.509, jan 1968.

[43] D. R. Smith, Willie J. Padilla, D. C. Vier, S. C. Nemat-Nasser, and S. Schultz. "Composite medium with simultaneously negative permeability and permittivity". *Phys. Rev. Lett.*, Vol. 84:pp. 4184–4187, May 2000.

[44] R. A. Shelby, D. R. Smith, and S. Schultz. "Experimental verification of a negative index of refraction". *Science*, Vol. 292(5514):pp. 77–79, 2001.

[45] R. Wu, Y. Gu, and L. Tan. "Optimizing the directional radiation of metamaterial antenna". In *2013 7th International Congress on Advanced Electromagnetic Materials in Microwaves and Optics*, pages 106–108, Sept 2013.

[46] M. Laroche, C. Arnold, F. Marquier, R. Carminati, J.-J. Greffet, S. Collin, N. Bardou, and J.-L. Pelouard. "Highly directional radiation generated by a tungsten thermal source". *Opt. Lett.*, Vol. 30(19):pp. 2623–2625, Oct 2005.

[47] V. Yannopapas. "Artificial magnetism and negative refractive index in three-dimensional metamaterials of spherical particles at near-infrared and visible frequencies". *Applied Physics A*, Vol. 87(2):pp. 259–264, May 2007.

[48] D. Schurig, J. J. Mock, B. J. Justice, S. A. Cummer, J. B. Pendry, A. F. Starr, and D. R. Smith. "Metamaterial electromagnetic cloak at microwave frequencies". *Science*, Vol. 314(5801):pp. 977–980, 2006.

[49] H. Tao, M. Zhao, Y. Xu, S. Wang, and Z. Yang. "Broadband metasurface carpet cloak in the near infrared region'. *IEEE Photonics Technology Letters*, Vol. 30(14):pp. 1281–1284, July 2018.

[50] D. R. Smith, D. C. Vier, Th. Koschny, and C. M. Soukoulis. "Electromagnetic parameter retrieval from inhomogeneous metamaterials". *Phys. Rev. E*, Vol.71:pp.036617, Mar 2005.

[51] Hans J. Schneider and P. Dullenkopf. "Slotted tube resonator: A new nmr probe head at high observing frequencies". *Review of Scientific Instruments*, Vol. 48(1):pp. 68–73, 1977.

[52] W. N. Hardy and L. A. Whitehead. "Splitring resonator for use in magnetic resonance from 2002000 mhz". *Review of Scientific Instruments*, Vol. 52(2):pp. 213–216, 1981.

[53] J. B. Pendry, A. J. Holden, D. J. Robbins, and W. J. Stewart. "Magnetism from conductors and enhanced nonlinear phenomena". *IEEE Transactions on Microwave Theory and Techniques*, Vol. 47(11):pp. 2075–2084, Nov 1999.

[54] V. V. Varadan and A. R. Tellakula. "Effective properties of split-ring resonator metamaterials using measured scattering parameters: Effect of gap orientation". *Journal of Applied Physics*, Vol. 100(3):pp. 034910, 2006.

[55] J. D. Baena, J. Bonache, F. Martin, R. M. Sillero, F. Falcone, T. Lopetegi, M. A. G. Laso, J. Garcia-Garcia, I. Gil, M. F. Portillo, and M. Sorolla. "Equivalent-circuit models for split-ring resonators and complementary split-ring resonators coupled to planar transmission lines". *IEEE Transactions on Microwave Theory and Techniques*, Vol. 53(4):pp. 1451–1461, April 2005.

[56] N. Katsarakis, T. Koschny, M. Kafesaki, E. N. Economou, and C. M. Soukoulis. "Electric coupling to the magnetic resonance of split ring resonators". *Applied Physics Letters*, Vol. 84(15):pp. 2943–2945, 2004.

[57] Koray A., Irfan B., Kaan G., Maria K., C. M. Soukoulis, and Ekmel O. "Investigation of magnetic resonances for different split-ring resonator parameters and designs". *New Journal of Physics*, Vol. 7:pp. 1367–2630, August 2005.

[58] J.J. Du, S.Y. Liu, Z.F. Lin, and S. T. Chui. "Magnetic resonance of slotted circular cylinder resonators". *Journal of Applied Physics*, Vol. 104(1):pp. 014907, 2008.

[59] Didier F. and Guy B. "Left-handed media and homogenization of photonic crystals". *Opt. Lett.*, Vol. 30(10):pp. 1189–1191, May 2005.

[60] R. Ziolkowski and J. Grant. "Scattering from cavity-backed apertures: The generalized dual series solution of the concentrically loaded lt;tex gt;e lt;/tex gt;-pol slit cylinder problem". *IEEE Transactions on Antennas and Propagation*, Vol. 35(5):pp. 504–528, May 1987.

[61] William A. Johnson and Richard W. Ziolkowski. "The scattering of an h-polarized plane wave from an axially slotted infinite cylinder: A dual series approach". *Radio Science*, Vol. 19(1):pp. 275–291.

[62] D. Colak, A. I. Nosich, and A. Altintas. "Radar cross-section study of cylindrical cavity-backed apertures with outer or inner material coating: the case of e-polarization". *IEEE Transactions on Antennas and Propagation*, Vol. 41(11):pp. 1551–1559, Nov 1993.

[63] D. Colak, A. I. Nosich, and A. Altintas. "Radar cross-section study of cylindrical cavity-backed apertures with outer or inner material coating: the case of H-polarization". *IEEE Transactions on Antennas and Propagation*, Vol. 43(5):pp. 440–447, May 1995.

[64] A. E. Serebryannikov and A. I. Nosich. "TE-case RCS analysis of finite-thickness slotted circular cylinder loaded with lossy filling". *IEEE Transactions on Antennas and Propagation*, Vol. 53(4):pp. 1426–1434, April 2005.

[65] A. E. Serebryannikov and A. I. Nosich. "TE-wave penetration into finite-thickness slotted circular cylinder with lossy and lossless inner coatings". *IEEE Transactions on Electromagnetic Compatibility*, Vol. 47(4):pp. 709–716, Nov 2005.

[66] J. D. Baena, R. Marqués, F. Medina, and J. Martel. "Artificial magnetic metamaterial design by using spiral resonators". *Phys. Rev. B*, Vol. 69:pp.014402, Jan 2004.

[67] B. Sauviac, C. R. Simovski, and S. A. Tretyakov. "Double Split-Ring Resonators: Analytical Modeling and Numerical Simulations". *Electromagnetics*, Vol. 24(5):pp. 317–338, 2004.

[68] M. Shamonin, E. Shamonina, V. Kalinin, and L. Solymar. "Properties of a metamaterial element: Analytical solutions and numerical simulations for a singly split double ring". *Journal of Applied Physics*, Vol. 95(7):pp. 3778–3784, 2004.

[69] W.B. Smythe. *Static and dynamic electricity*. Hemisphere Publishing, United States, 1988.

[70] X. Pan and C. G. Christodoulou. "A narrow-wall slotted waveguide antenna array for high power applications". In *2014 IEEE Antennas and Propagation Society International Symposium (APSURSI)*, pages 1493–1494, July 2014.

[71] S. B. Pottier, F. Hamm, D. Jousse, P. Sirot, F. T. Talom, and R. Vzinet. "High Pulsed Power Compact Antenna for High-Power Microwaves Applications". *IEEE Transactions on Plasma Science*, Vol. 42(6):pp. 1515–1521, June 2014.

[72] J.A.Rees, editor. *Electrical Breakdown in Gases*. "Figure 3. Calculated (x) and observed (o) spaking potentials in air". John Wiley & Sons, New York, 1973.

[73] X. Pan, C. G. Christodoulou, J. Lawrance, J. McConaha, and M. Landavazo. "Cold&hot tests of an s-band antenna for high power microwave systems". In *2017 IEEE International Symposium on Antennas and Propagation USNC/URSI National Radio Science Meeting*, pages 627–628, July 2017.

[74] L.I. Berger. *CRC Handbook of Chemistry and Phsics*, chapter 15. Practical Laboratory Data. "Table 1. Dielectric strength of gases". CRC Press/Taylor and Francis, Boca Raton, FL, internet version 2009 edition, 2009.

[75] "IEEE standard for high-voltage testing techniques". *IEEE Std 4-2013 (Revision of IEEE Std 4-1995)*, pages pp. 1–213, May 2013.

[76] S. Riyopoulos. "Multipactor saturation due to space-charge-induced debunching". *Physics of Plasmas*, Vol. 4(5):pp. 1448–1462, 1997.

[77] E. Sorolla, A. Sounas, and M. Mattes. "Space charge effects for multipactor in coaxial lines". *Physics of Plasmas*, Col. 22(3):pp. 033512, 2015.

[78] D. Gonzlez-Iglesias, O. Monerris Belda, M. E. Daz, B. Gimeno, V. E. Boria, and D. Raboso. "Experimental analysis of the multipactor effect with rf pulsed signals". *IEEE Electron Device Letters*, Vol. 36(10):pp. 1085–1087, Oct 2015.

[79] J. R. M. Vaughan. "A new formula for secondary emission yield". *IEEE Transactions on Electron Devices*, Vol. 36(9):pp. 1963–1967, Sept 1989.

[80] CST PS STUDIO. CST computer simulation technology. `https://www.cst.com`, 2018. [Online, Last accessed on 2018].

[81] M. A. Furman and M. T. F. Pivi. "Probabilistic model for the simulation of secondary electron emission". *Phys. Rev. ST Accel. Beams*, Vol. 5:pp. 124404, Dec 2002.

[82] Waterjet Cutting Inc. Albuquerque. Waterjetcuttinginc.com. `http://www.waterjetcuttinginc.com/`, 2018.

[83] MG Chemicals. 843-Super Shield Silver Coated Copper Conductive Coating - Acrylic Conductive Coatings (Original Series) | MG Chemicals. `https://www.mgchemicals.com/products/emi-and-rfi-shielding/acrylic-conductive-coatings-original-series/super-shield-silver-copper-843`, 2018. [Online, Last accessed on 2018].

[84] Accura Bluestone (SLA) — 3D Systems. 3D Systems. `https://www.3dsystems.com/materials/accura-bluestone`, 2018.

[85] RePliForm. Repliforminc.com. `http://repliforminc.com/`, 2018.